TABLE OF CONTENTS

Page

LIST OF TABLES

LIST OF FIGURES

LIST OF ABREVIATIONS

CSP	Canadian Softwood Plywood
DFP	Douglas-Fir Plywood
MAE	Mean Absolute Error
MAPE	Mean Absolute Percent Error
NAH	Nearfield Acoustical Holography
OHS	Occupational Health and Safety
PRF	Penetration Resistance Force
PP	Poplar Plywood
RMS	Root Mean Square
SEE	Standard Error of Estimate

LIST OF SYMBOLS

Symbol	Unit	Description
A_1, A_2	m^2	Piston effective areas on the piston head screw and rod side
A_{ch}	m^2	Air channel cross sectional area
A_{eff}, A_{e1}, A_{ma}, A_{1m}	m^2	Restriction effective areas
A_{h1}, A_{h2}	m^2	Area of the head valve supporting the downward pressure and upward pressure
A_r	m^2	Rod cross-sectional area
c	m/s	Sound speed
C_f	-	Restriction discharge coefficient
C_v	kJ/kg^{o}C	Specific heat at constant volume
D	m	Nail diameter
d_c	m	Chamber no.1 diameter
D_{ch}	m	Inner diameter of the air channel
f	Hz	Frequency
g	m/s^2	Gravitational acceleration
F_{fh}	N	Friction force between head valve and cap wall
F_{fp}	N	Friction force between piston and cylinder wall
F_{hm}	N	Operator hand force
F_r	N	Penetration resistance force
F_s	N	Compression spring force
F_{sfh}, F_{dfh}	N	Head valve-cap wall static and dynamic friction forces
F_{sfp}, F_{dfp}	N	Piston-cylinder wall static and dynamic friction forces
H_M	N/mm	Hardness modulus
L	m	Piston stroke
L_{ch}	m	Air channel length
L_h	m	Maximum head valve displacement
l_n	m	Nail length
$L_{WA,1s}$	dBA	A-weighted single-event sound power level

k_{esg}	N/mm	Equivalent safety guard stiffness
k_{hc1}	N/mm	Contact stiffness between the head valve and nail gun cap surface
k_{hc2}	N/mm	Contact stiffness between the head valve and cylinder
k_{pb}, k_{ps}	N/mm	Piston bumper and piston stopper stiffness
k_s	N/mm	Compression spring stiffness
k_{sg}	N/mm	Safety guard spring stiffness
k_w	N/mm	Wood stiffness
k_{ws}, k_{wsn}	N/mm	Wood- support and wood-nail gun contact stiffness
M	Kg	Projectile mass
$\dot{m}_{ch}$	kg/s	Mass flow through the channel
M_g, M_h, M_n, M_w	Kg	Nail gun, head valve, nail , and wood masses
$\dot{m}_{in}$, $\dot{m}_{out}$	kg/s	Input and output mass flow rates
NL	m	Nail length
P_1, P_2	Pa	Absolute air pressures in chamber no.1 and 2
P_a	Pa	Absolute ambient pressure
P_{ch}	Pa	Pressure along the channel
P_{che}	Pa	Pressure at the air channel end
P_{cr}	-	Critical pressure ratio
P_{ext}	Pa	External chamber absolute pressure
P_h	Pa	Head valve chamber absolute pressure
P_r	Pa	Return air chamber absolute pressure
P_u , P_d	Pa	Upstream and downstream pressures
q_{in}, q_{out}	J/s	Heat transfer terms
R	J kg^{-1} K^{-1}	Ideal gas constant
R^2	-	Coefficient of determination
R_{ch}	N s/m^4	Channel resistance
s	m	Coordinate along the channel
ST	-	Nail shank type
T	°k	Gas temperature

$t_0, t_1, \ldots, t_{18}$	s	Time positions
$\dot{U}$	J/s	Internal energy rate of change
v_0	m/s	Impact velocity
v	m/s	Penetration velocity
V	m^3	Chamber volume
V_{01}, V_{02}	m^3	Inactive volumes of chamber no.1 and 2
V_{ext}	m^3	External chamber volume
V_r	m^3	Return air chamber volume
$\dot{W}$	J/s	Work rate of change
y	m	Nail displacement
x_{gl}, y_{gl}	-	Global coordinate system
y_g	m	Nail gun displacement
y_h	m	Head valve displacement
y_{hr}	m	Head valve displacement relative to the nail gun
y_{msg}	m	Maximum compression of safety guard spring
y_p	m	Piston-rod assembly displacement
y_{pbin}	m	Distance between the rod end and nail head at t_0
y_{pbp}	m	Distance between the rod end and workpiece surface at t_0
y_{pr}	m	Piston-rod assembly displacement relative to the nail gun
y_s, y_{sp}	m	Compression spring displacement and preload length
y_w	m	Wood displacement
$\alpha, \alpha_{in}, \alpha_{out}$		Coefficients of heat transfer process
β	-	Floor factor
β_{pb}, β_{ps}	Ns/mm	Damping coefficients of the piston bumper and stopper
γ	-	Specific heat ratio
μ	N s/m^2	Air dynamic viscosity
μ_{fh}	-	Head valve-cap wall friction coefficient
μ_{fp}	-	Piston-cylinder wall friction coefficient
μ_r	-	Nail-wood friction coefficient
$\Pi_1, \ldots, \Pi_6$	-	Dimensionless parameters

ρ	kg/m^3	Density
ϕ	-	Flow attenuation through the length of the air channel

INTRODUCTION

Since the 50s, nailing devices have been used to fasten separate pieces of material together by nails. Nailing devices have a wide range of applications in the construction industry even though they generate noise at levels high enough to put workers at risk of hearing loss.

The present study belongs to a broader investigation aiming to reduce noise emissions in pneumatic nailing devices. The contributions of this research work are presented in three published (or submitted) articles integrated into this article-based thesis.

This introduction first presents a description of the nailing device operation followed by the research problem, the general research objectives, the literature review, the specific research objectives, and finally the document structure and research methodology.

0.1 Nailing device operation

Figure 0.1 shows a schematic representation of a pneumatic nailing device operation. When the trigger valve (10) is in the released position, the compressed air covers the area above the head valve (3). The resultant of the air pressure on both sides of the head valve and the compression spring downward force keeps the head valve pressed against the cylinder top. Pulling the trigger stops the air flow to the head valve upper area. As a result, the head valve goes up and impacts the nailing device internal cap surface which closes the air exhaust. The compressed air flows to the internal chamber (4) above the piston head, pushes the piston (6) downward. The nail penetration into the workpiece (11) causes the workpiece fracture and deformation. The resulting workpiece vibration continues even after the penetration end. Impacts also take place between the piston and piston bumper (7) after the penetration end (Figure 0.1 (c)). The associated piston oscillations result in vibrations of the nailing device body. Releasing the trigger valve allows a back motion of the head valve which stops the compressed air discharge to the piston head and opens the air exhaust. The pressurized air inside the return chamber (9) then drives the piston upward, pushing at the same time the air above the piston to the atmosphere through the air exhaust holes (2). At the

end of its returning stroke, the piston head impacts the piston stop (8) followed by the piston oscillations.

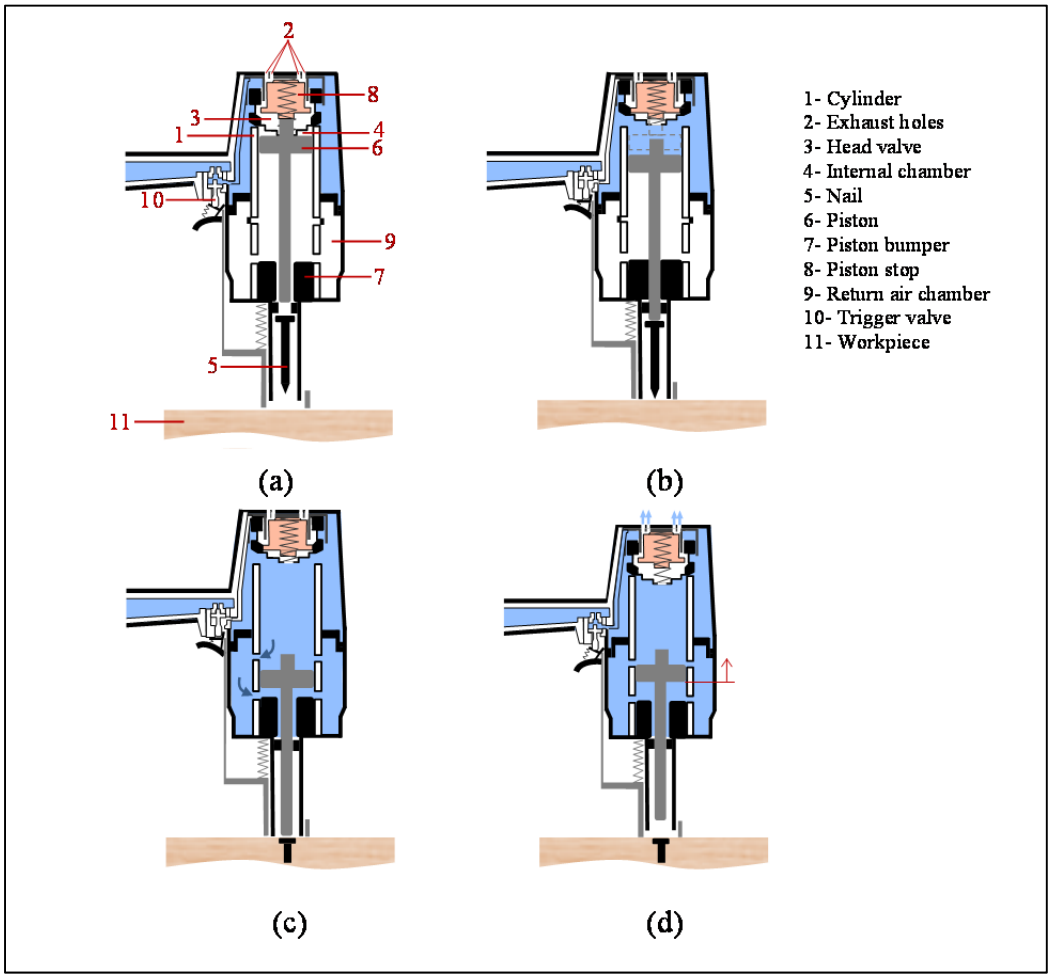

Figure 0.1 Schematic representation of a pneumatic nailing device: (a) at rest, (b) during the driving stroke, (c) end of the driving stroke, (d) the air exhaust

0.2 Research problem

The general problem of this research is the high level of noise generated by pneumatic nailing devices. This leads to health problems among workers using these devices, as the noise above a certain level induces hearing loss. This issue is referred to as “Occupational Health and Safety (OHS) problem” which is addressed in section 0.2.1. This health problem comes from the lack of appropriate technology such as reduced noise devices; this is the

second issue called “Technological problem” discussed in section 0.2.2. This technological problem in turn results from a lack of scientific knowledge about noise reduction of these devices; this is the “Scientific problem” addressed in section 0.2.3.

0.2.1 Occupational health and safety(OHS) problem

Long term exposure (i.e. eight hours/day) to sound levels over 85 dBA causes permanent hearing loss. From 1997 to 2013, more than 50,000 new cases of occupational hearing loss have been reported in Quebec (INSPQ, 2015). The number of workers with hearing loss increased from 1,540 in 1997 to 5,609 in 2013 (INSPQ, 2015). In 2014, occupational deafness constituted 65.8% of all occupational disease cases making occupational deafness the most frequent occupational injury in Quebec (CSST, 2015). The problem is not limited to Quebec. In the US, approximately 22 million workers are at risk of hearing loss (NIOSH, 2014). The estimated cost of US workers’ compensation for hearing disability is $242 million per year (NIOSH, 2014). In Australia, between July 2002 and June 2007, about 16,500 cases of occupational deafness were reported (Timmins and Granger, 2010).

Throughout the world, many construction workers use pneumatic nailing devices every day. Exposure to hazardous noise levels emitted by these devices contributes significantly to risk of hearing damage among these workers (Shanks, 2008).

0.2.2 Technological problem

To prevent the noise-induced hearing loss, the generated noise by pneumatic nailing devices should be reduced at the worker’s ear. This noise reduction can be realized through the two following solutions:

(1) <u>Using ear protectors</u>

As a short-term solution, ear protectors are generally effective at preventing the hearing damages (Berger et al., 2003). However, they are not an ideal choice for users due to two disadvantages: 1- people often feel physical discomfort wearing them which can make them

stop using protectors, and 2- people have difficulties communicating with each other while using ear protectors.

(2) Noise reduction at the Source

This solution has none of the abovementioned disadvantages. However the survey of this research group and Shanks (2008) did not find any commercial reduced noise pneumatic nailing device.

0.2.3 Scientific problem

To reduce the noise at the source, the classical noise control solutions (such as enclosures and mufflers) might lead to sufficient reductions in systems with only one dominant noise source. For systems with multiple noise sources, big noise reductions require a decrease of contribution of all sources. Therefore all the sources should be isolated either using enclosures or mufflers. This might considerably increase the device weight and volume and also restricts access to the device or workpiece. A fundamental solution to this noise problem can be to improve the device concept design. However, author's survey showed no account of the nailing device redesign in the science and trade literature. The reason might be the lack of knowledge about the noise sources and also the absence of a model which can simulate the system operation. A comprehensive study of the noise sources is required to identify the system physical processes and their associated noise generation mechanisms. A model is needed to predict the sound emission from the nailing device. The details obtained from the noise source identification and model predictions are used to propose the design modifications. The model is also used to evaluate the efficiency of the proposed modifications.

A comprehensive model of the nailing device includes two parts: a dynamic model that predicts the system variables (forces, whole body motion, and air flow), and a vibro-acoustic/air flow-acoustics model which predicts structural vibrations and sound radiations from the structures and from the air flow to the atmosphere.

Dynamic modeling of the nailing device requires mathematical modeling of different internal and external physical processes involved in its operation cycle. All of these processes can be described through already existing mathematical relations, except for the penetration process of the nail into the wood. During the penetration process, a penetration resistance force (PRF) is imposed on the nails. The PRF depends on various factors, including: nail physical properties, wood physical and mechanical properties, nail displacement, impactor mass, and penetration velocity. A model is required to predict this force.

Vibro-acoustic modeling requires vibration analysis of the system under the dynamic excitation forces to obtain the modes of vibration and the surface velocities. The dynamic excitation forces are predicted by the dynamic model. The surface velocities are then used to compute the acoustic radiation and radiation efficiency of the system. Moreover, air flow-acoustics model establishes a relationship between the mass flow rate and the sound radiation of the exhausting air into the atmosphere.

0.3 Research objectives

This study aims to provide the details on the noise sources and also a simulation tool in response to the research needs explained in section 0.2.3 for the pneumatic nailing device redesign.

As a simulation tool, a dynamic model of the system should be developed. The dynamic model is chosen since it is the fundamental simulation tool served to provide the inputs (dynamic excitation forces) to the vibro-acoustic model. Moreover, the dynamic model simulates the system operation; it provides the details which otherwise cannot be obtained through the noise source identification (or the vibro-acoustic model). The knowledge which is needed to be used in conjunction with the details obtained from the noise source identification to propose the design modifications. On the other hand, to solve the vibration/noise problem of the nailing device, the root causes should be tackled which are indeed the excitation forces and the air flow oscillations. Varying the forces and the flow conditions certainly will cause some changes in the system operation and performance; these changes are only predictable by the dynamic model. Finally with the dynamic model alone

and due to the linearity of the system, the effective design modifications can be proposed to reduce the vibration and noise by decreasing the excitation forces. The design modifications can be also made to change the air flow conditions to reduce the noise/vibration. However, to obtain the precise reduction in the vibration/sound radiation as a result of decreasing the forces and/or changing the air flow conditions, the next step will be to develop the vibro-acoustic/air flow-acoustics model of the system.

To sum up, the noise source identification and dynamic modeling of the pneumatic nailing process are the two objectives of this research. However as explained in section 0.2.3, before proceeding with the dynamic modeling, a model should be developed to predict the nail-wood penetration resistance force. Therefore, this study pursues the following two objectives towards solving the nailing device noise problem:

(1) Identifying and ranking the noise sources in a pneumatic nailing process;
(2) Developing dynamic model of the pneumatic nailing devices.

0.4 Literature review

This section presents a complete review of the previous studies related to noise source identification and modeling of the pneumatic nailing devices. Each following subsection presents the pertinent literature to each objective in the order established in section 0.3. In general, the pneumatic nailing device noise is mainly generated by two processes: the impact process, and the process of the air passing through flow restrictions. For better understanding of the nailing device noise sources, sections 0.4.1 and 0.4.2 present a review of the literature which studied the noise generation mechanisms in these two processes.

0.4.1 Noise generation mechanisms in impact processes

Impact noise is the type of high peak level and short duration sound associated with collision of two or more bodies (Akay, 1978).

The mechanisms involved in generation of impact noise can be grouped under four different classes (Figure 0.2): rigid body acceleration/deceleration, air ejection, local surface

deformations and impact material fracture, and pseudo-steady-state vibrations. These mechanisms are described in the four following sections.

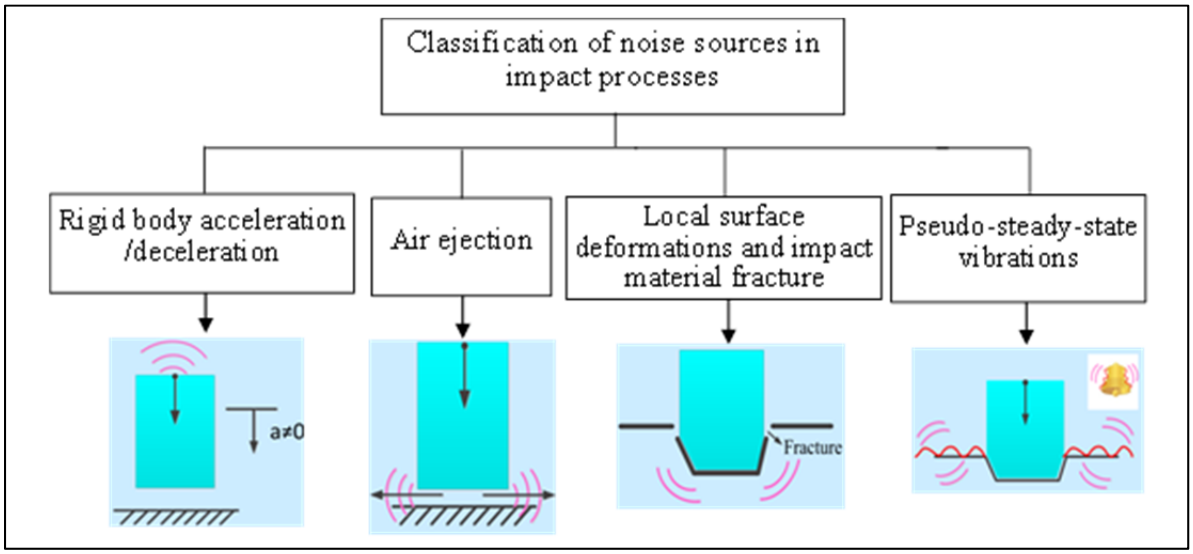

Figure 0.2 Schematic view of four mechanisms of noise generation in impact processes

0.4.1.1 Rigid body acceleration/deceleration

This type of sound radiation is associated with the pressure disturbance generated in an acoustic medium by sudden velocity change of an object while impacting other object (see Figure 0.2).

In the pneumatic nailing process, this kind of radiation might be generated due to the impact between: 1- the piston and piston bumper, 2- the piston and piston stop, 2- the head valve and nailing device internal cap surface, 3- the piston-rod assembly and nail, 4- the nail and workpiece.

While a few studies (Hodgson, 1976; Richards and Carr, 1986) have determined the sound radiation from this mechanism in forging machineries, rigid body radiation in the pneumatic nailing process has not been the subject of any previous studies.

0.4.1.2 Air-ejection

When the gap between two approaching surfaces is narrowed, the air ejection from this gap develops a pressure gradient between these surfaces (Akay, 1978). Holmes (1973) analytically showed that this pressure gradient generates a rarefactive acoustic wave in the medium.

In the pneumatic nailing process, this kind of radiation might be generated as a result of the impact between different parts. However due to the small area of the impacting surfaces, the generated noise seems to be insignificant in comparison to the other noise sources. The sound field resulting from this mechanism in pneumatic nailing devices has not been investigated in previous studies.

0.4.1.3 Local surface deformation and fracture

This type of radiation results from rapid fracture and deformation of the surfaces in impact. In nailing devices, the workpiece deformation/fracture due to high speed penetration of the nails might be a source of radiation. Similar to the other noise generation mechanisms, the literature survey indicated that the noise radiation due to this mechanism in the nailing process has not been the subject of any previous studies.

0.4.1.4 Pseudo-steady-state vibrations

Due to very short time span of the impact process, the applied energy is not entirely converted to work. The excess energy causes transient vibrations of the mechanical structure and pseudo steady-state radiation (or ringing noise) (Richards et al., 1983; Richards et al., 1979). This phenomenon has been illustrated in the case of the inelastic impact of a sphere on a rectangular plate in Troccaz et al. (2000).

In the pneumatic nailing process, this kind of radiation might be generated as a result of: 1- the workpiece vibration, 2- the machine body vibration.

To the authors' knowledge, the noise radiated by this mechanism in the nailing process has not been studied previously. However two studies have generally discussed the generated noise by pneumatic nailing devices. Adelberg et al. (2002) distinguished four noise peaks in the sound pressure time history of the process. The authors attributed these peaks to the following four sources: (1) air exchange after trigger pulling, (2) piston impact with piston bumper, (3) air exhaust, and (4) piston return impact with piston stopper. Jayakumar et al. (2015) identified the impact noise transmitted through the structure as the first contributor to the total noise. The study also identified four distinct peaks in the noise time history. The authors associated these peaks to the following sources: (1) compressed air flow through inlet port, (2) piston rod-nail impact, (3) nail-wood impact, (4) air exhaust.

0.4.2 Noise generation mechanisms in restrictions outflow processes

The outflows from fixed (orifices) and variable (valves) flow restrictions can be a source of strong mechanical vibration and high intensity noise. The generated aerodynamic noise strongly depends on the range of the restriction outflow. When the flow is in the subsonic range (or the flow velocity at the nozzle exit is below the sound speed), the turbulent mixing noise is the most effective emitter of the acoustic power (Lighthill, 1962; 1963; Ribner, 1964; Witczak, 1976). This noise type results from turbulent mixing of jet flows with the ambient fluid. The large-scale and fine-scale turbulence structures contribute to the turbulent mixing noise (Tam, 1995).

On the other hand, supersonic conditions are engendered when the flow is choked and the flow velocity at the restriction exit reaches the sound speed. Under such conditions, two additional noise sources appear and predominate over the turbulent mixing noise (Witczak, 1976): broadband shock-associated noise, and screech tones (acoustic feedback). The broadband shock-associated noises result from interactions between downstream propagating large-scale turbulence structures passing through quasi-periodic shock cell structures (Tam, 1995). Screech tones are discrete frequency noises (Tam, 1995; Witczak, 1976). They result from unsteady interactions between large amplitude instability waves and quasi-periodic shock cell structures.

These noise generation mechanisms usually exist in pneumatic devices such as pneumatic nailing devices particularly during the air exhaust process. Three studies (Adelberg et al., 2002; Jayakumar, Kim and Zechmann, 2015; Tisserand and Triomphe, 2011) studied the noise generated during the air exhaust process in pneumatic nailing devices. As mentioned in section 0.4.1.4, Adelberg et al. (2002) and Jayakumar et al. (2015) found a distinct peak in the noise time history associated with the exhaust process. Jayakumar et al. (2015) identified the exhaust related noise as the second contributor to the total noise. The authors designed and applied four mufflers to reduce the exhaust noise. Tisserand and Triomphe (2011) also evaluated the noise reduction obtained during the air exhaust phase when using a silencer device.

0.4.3 Noise source identification

This section provides a general overview of the techniques used in the literature to study the noise sources in different machineries and discusses the effectiveness of each technique in identifying the nailing device noise sources.

0.4.3.1 General noise source identification techniques

As described in section 0.1, the pneumatic nailing process constitutes of various events occurring at successive time intervals. Identification of the noise sources in the nail gun requires identifying these processes and their associated noise generation mechanisms at different instants. The most effective techniques for this purpose can be found among those used in the literature to identify and rank the noise sources in the machineries. This section discusses the four most popular ones, namely: (1) time-synchronized data analysis technique, (2) correlation and coherence techniques, (3) selective wrapping and muffler technique, (4) nearfield acoustical holography technique.

(1) Time-synchronized data analysis technique is used to identify the physical processes (and their associated noise generation mechanisms) involved in the machine operation at different time instants through measuring and time domain analysis of different variables involved in its cycle. Stewart et al. (1975) performed a time domain analysis of the

punch press sound and workpiece acceleration signals and identified five distinct events occurring during the machine cycle. Similar to the punch press, the events in the pneumatic nailing device are successive in time. Therefore this technique can accurately identify the nailing device physical processes (and their associated noise generation mechanisms) provided that adequate number of variables are measured and observed.

(2) Correlation and coherence techniques can be used to locate the noise sources by seeking the relationship between different transducers signals (input) and the radiated sound (output). This technique might be successfully used in source identification of the processes with random noise such as diesel engines (Chung et al., 1975; Kumar and Srivastava, 1975). However for the devices with a well-trackable time signature such as the pneumatic nailing device, the noise sources could be well identified by only observing the time signals and using this technique does not appear to be necessary.

(3) Selective wrapping and muffler is a classical technique to rank the noise sources. In this technique, all the noise source emission is reduced by either an enclosure made of a sound barrier material (lined on the inside with a sound absorbing layer) or an oversize muffler. The reduced noise sources are then exposed one at a time by removing the associated noise control measure so that the noise radiation from each source can be measured. Beiers (1966) applied this technique to measure the contribution of the air exhaust noise source in a pneumatic rock drill. The author fitted one end of a long hose over the exhaust port to lead away the exhaust noise to a point outside the anechoic chamber where a muffler was attached to the other end of the hose. A similar setup can be also used to enclose the air exhaust noise of the pneumatic nailing device. Richards et al. (1983) used this technique to eliminate the pseudo-steady-state radiation of the concrete bases in a drop hammer using a sand-filled enclosure around the bases. The standard BSI (1999) used a similar setup to minimize the workpiece noise contribution, though the efficiency of the setup has never been established. Overall, the technique assures a reliable classification of the noise sources and it is ideal for small machineries. In pneumatic nailing devices, since multiple noise sources radiate at the same time, the time-synchronized data analysis

technique is limited in the number of sources it can identify and rank. Thus, it can be completed by a selective wrapping and muffler technique.

(4) Nearfield acoustical holography (NAH) provides the acoustic intensity map (image), the velocity vector field, and the acoustic pressure of a radiating surface in 3D space through analyzing the nearfield acoustic pressure measurements at a set of points on a 2D hypothetical surface. For the pneumatic nailing device, using the time-synchronized data analysis technique in conjunction with the selective wrapping and muffler technique can identify the physical processes which indicate the radiating parts of the bodies. However, if there is a need to refine the radiation from each part, using this technique might bring some additional information.

0.4.3.2 Nailing device noise identification techniques

Two studies (Adelberg et al., 2002; Jayakumar et al., 2015) have examined the noise problem in pneumatic nailing devices. Adelberg et al. (2002) used a simple experimental setup where one microphone captures the sound at the operator position to identify the noise sources. The authors distinguished four noise peaks in the sound pressure time history of the process. Considering nailing device operating mechanism, they attributed these peaks to the four sources mentioned in section 0.4.1.4.

Recently, Jayakumar et al. (2015) used sound pressure time history and acoustic maps (obtained using NAH) to determine the possible noise sources and the corresponding transmission paths. In the investigation the workpiece was supported by a sand bed. The presented acoustic map showed the radiating surfaces in four successive time sequences during the nailing device cycle.

However, considering complexity of the noise generation mechanisms in a pneumatic nailing device, a more comprehensive experimental approach is essential to provide a more detailed separation of the noise generation mechanisms in time and to determine the relative contribution of the major sources. A combination of the time-synchronized data analysis and selective wrapping and muffler techniques appears to provide such results.

0.4.4 Nail- wood penetration

Though the nail penetration into the wood at quasi-static velocities has not been investigated in any previous studies, two studies (Bartelt et al., 1994; Villaggio, 2005) have examined nail penetration tribo-dynamic aspects at high velocities. Villaggio (2005) studied nail penetration into soft materials as a result of hammering. The author idealized the nail as a cylindrical shaft, and developed an analytical formulation of the penetration rate per hammer blow. For their part, Bartelt et al. (1994) employed numerical models to simulate impact penetration of nails driven by power-actuated fastening devices into hard construction materials such as steel or concrete.

Since wood products correspond to highly heterogeneous domains, the precise numerical modeling of such materials results in computationally difficult simulations. Moreover, the analytical modeling would require many simplifications which highly affect the model precision. The empirical modeling, however, appears to ensure rapid and precise representations.

0.4.5 Dynamic modeling of the pneumatic nailing devices

The mathematical models of pneumatic valves and actuators have been developed in numerous studies (Andersen, 2001; Riachy and Ghanes, 2014; Richer and Hurmuzlu, 2000a; 2000b; Sorli et al., 2004).

Though the pneumatic nailing device represents a more complicated system (due to the existence of various moving elements, and the impacts and interactions between various components), only two studies (Hu, 2009; Zhong et al., 2008) investigated the mathematical modeling of pneumatic nailing devices. Zhong et al. (2008) presented a simplified mathematical pneumatic nailer model. The authors simulated the air pressure in three out of five nailer chambers and considered the piston as acting against a constant penetration resistance force. Later, Hu (2009) examined the gas dynamics influence on the performance of a pneumatic nailer. This second reference also neglected the complex tribo-dynamic conditions involved in the nail penetration process and reduced the nail penetration resistance

to a constant force. The study of nail penetration into concrete by Bartelt et al. (1994) and also investigations on high velocity impact penetration of solids by different projectiles (Goldsmith, 1960) have shown that PRF may be highly affected by the penetrating object displacement and velocity.

Moreover, in the nailing device dynamic models developed by the above-mentioned studies (Hu, 2009; Zhong et al., 2008), the influence of the air channel connecting the chambers, the dynamics of the impacts occurring between the different moving and fixed components of the system (impact between piston and bumper or between the workpiece and supports, etc.), the nailing device body and valve dynamics, as well as the workpiece dynamics were ignored. The valve was considered as a fixed restriction. Neglecting dynamics of all these important parts in the model might strongly affect the model precision.

0.5 Research methodology

The literature review of section 0.4 extracted the knowledge useful for the purpose of this study and introduced the shortcomings of the literature in dealing with nailing devices noise problem. This information allows defining the methodology to accomplish the objectives (introduced in section 0.3) in this section.

With regard to objective 1, section 0.4.3 concluded that time domain identification and ranking of the noise sources should be conducted using two complementary experimental techniques, namely, time-synchronized data analysis and selective wrapping and muffler. Therefore, the time-synchronized data analysis technique is used to identify the noise generation mechanisms at different time instants and the selective wrapping and muffler technique is used to rank the major noise sources.

To develop the dynamic model of the pneumatic nailing process (objective 2), an empirical prediction model for nail-wood penetration resistance force is required. This prediction law can be obtained by following two different approaches in parallel: a high-speed approach and a quasi-static approach. While the provided law by the high-speed approach covers a wider range of the influencing factors, this approach is rather complicated

and expected to be a long development process. Therefore considering the possibility that it would not lead to the required results before the end of this doctoral work, an alternative simpler approach is conducted: a quasi-static approach. This approach provides the results required for the dynamic model on time while carrying out the high-speed approach.

Though the high-speed approach may not be used in this work to develop the law, it will be useful in the long run to obtain a law which fully covers the entire space of all influential parameters involved in the nail penetration process of pneumatic nailing devices. The approach requires a sophisticated test machine to measure PRF at high penetration velocities. This machine allows developing PRF law over a wide range of the penetration velocities while including the influence of impactor mass parameter. The machine should be designed such that to cover the penetration velocity ranges of the pneumatic nailing process (20-30 m/s). This machine can be designed and fabricated using the knowledge gained at different stages of this research project.

Alternatively, the quasi-static approach uses a relatively simple experimental setup to measure the PRF when the nail is driven into the wood at quasi-static velocities. This approach can provide a rapid and precise representation of the law under quasi-static conditions.

The dynamic model of the pneumatic nailing process can be thus developed integrating the empirical PRF law obtained using the quasi-static approach.

To summarize, the following tasks should be performed to accomplish the objectives introduced in section 0.3:

(1) Time-domain identification and ranking of the noise sources in a pneumatic nailing process;
   (1-1) Identification of the system physical processes and their associated noise generation mechanisms using a time-synchronized data analysis technique;
   (1-2) Ranking of the noise sources using a selective wrapping and muffler technique.

(2) Developing an empirical prediction law for nail-wood penetration resistance force;

(2-1) Developing an empirical prediction law at quasi-static penetration velocities;

(2-2) Design and fabrication of a test machine for conducting nail driving experiments at high penetration velocities.

(3) Developing a dynamic model of the pneumatic nailing devices.

0.6 Thesis structure

This section presents the structure of the present document and contents of each chapter. Table 0.1 shows the tasks performed in each chapter. Tasks 1-1 and 1-2 are covered in the same chapter (chapter 1) since their obtained results should be analyzed in conjunction with each other to provide a comprehensive identification and ranking of the noise sources. Tasks 2-1 and 2-2 are presented in the separate chapters (2 and 3) as they employ independent and different approaches to study the nail penetration tribo-dynamic aspects. Finally, task 3 (dynamic modeling) can be found in chapter 4. The dynamic modeling is presented as the final chapter of this thesis since it uses the results achieved in the first two chapters. Chapter 4 uses the results of chapter 2 (PRF law) to develop the dynamic model and it connects the dynamic model predictions with the results of chapter 1 (the identified noise sources).

Table 0.1 Methodology tasks

Chapter	**Task**
1	1-1, 1-2
2	2-1
3	2-2
4	3

0.6.1 Chapter 1- Article 1: Time domain identification and ranking of noise sources in a pneumatic nailing process.

This chapter identifies and ranks the noise sources in a pneumatic nailing process (tasks 1-1 and 1-2). The analysis is mostly carried out in the time domain for two reasons: a) the process includes the consecutive events, and b) the results can be well connected with the dynamic model predictions.

The study seeks the answers to the following questions: (1) which physical processes are responsible for the generated noise at different time instants?, (2) what is the noise level associated with each process and what is the contribution of each of the three involved noise sources (nailing device body, workpiece, and air exhaust) in each process noise?, (3) what are the major noise sources?, and (4) what is the influence of workpiece support on the generated noise? i.e. is the sandbox support suggested in the standard (BSI, 1999) efficient in minimizing the workpiece contribution?

Question 1 is addressed by using a range of instruments to detect every motion and change of variable during the nailing device operation. The physical processes at different time instants are then identified by observing and relating the measured data (Time-synchronized data analysis technique).

To answer questions 2 and 3, a selective wrapping and muffler technique is used to obtain the sound signal associated with each source. Frequency analysis of the signals results in overall generated noise associated with each process and contribution of each source in this noise. It also provides the overall generated noise by each source and thus ranking of the major noise sources.

To address question 4, the answers to questions 1 to 3 are compared for two workpiece supports, namely, a standardized sandbox support and a more realistic support.

0.6.2 Chapter 2- Article 2: An empirical prediction law for quasi-static nail-plywood penetration resistance.

This chapter develops an empirical prediction model for nail-plywood penetration resistance force at quasi-static velocity ranges (task 2-1). A universal testing machine is used to drive the nail into the wood samples at constant speeds. The machine measured PRF as a function of the position. The applied experimental procedure is simple yet very precise as it accounts for all the influencing factors at quasi-static velocity range, including: nail physical properties, wood physical and mechanical properties, and nail displacement. To generalize the model, the studied factors are reduced to dimensionless parameters. The final model is validated by comparing the model-predicted forces to measurements completed for nail geometries not considered during the model preparation.

0.6.3 Chapter 3- Design and fabrication of a test machine for high-velocity nail driving experiments

This chapter designs and fabricates a test machine for conducting the nail driving tests under high-velocity conditions (task 2-2). The machine is designed such that the tests fully cover the entire parameter space, including: nail physical properties, wood physical and mechanical properties, nail displacement, impactor mass, and penetration velocity. The range considered in the design for the impactor mass and the penetration velocity includes the nailing device impactor mass (or the piston-rod assembly mass) and the nailing device penetration velocity, respectively.

0.6.4 Chapter 4- Article 3: Nonlinear dynamic modeling of pneumatic nailing devices

This chapter develops a mathematical modeling procedure for pneumatic nailing devices (task 3). The model accounts for the dynamics of the chamber pressures, the moving parts, the interactions and impacts between the fixed and moving components, and includes the nailing device body and workpiece. All the system parameters integrated into the proposed model were established from experimental measurements. The model also integrates an empirical prediction law for nail-solid wood PRF developed following the approach introduced in chapter 2. The investigation includes a comprehensive experimental validation of the model.

0.6.5 Conclusion and future recommendations

This chapter first provides a summary of the main results obtained during this work together with a reminder of the research problems and objectives. The limitations of this study and future recommendations are then presented. Finally, the scientific and technological impacts of this work are discussed.

0.6.6 Appendix I: An empirical prediction law for quasi-static nail-solid wood penetration resistance

This appendix gives the unpublished results of the empirical prediction model for nail penetration resistance force at quasi-static velocity ranges in the case of solid wood based on the same procedure presented in article 2 (chapter 2) in the case of plywood. These results are used in article 3 (chapter 4) for the development of the nonlinear dynamic modeling of pneumatic nailing devices.

0.7 Contributions

This thesis contributes in three main areas. The following lists these areas along with the journal articles, the conference papers and the posters presented in each area:

1- Time-domain identification and ranking of the noise sources in a pneumatic nailing process.

Journal article,

- Z.N. Ahmadabadi, F. Laville, R. Guilbault, Time domain identification and ranking of noise sources in a pneumatic nailing process, submitted to Journal of Applied Acoustics (2016).

Conference papers,

- Z.N. Ahmadabadi, F. Laville, R. Guilbault, Studying of the noise sources in a pneumatic nail-gun process, The Journal of the Acoustical Society of America, 138 (2015) 1937-1937.

- Z.N. Ahmadabadi, F. Laville, R. Guilbault, Study of parameters influencing pneumatic nail-gun noise, in: INTER-NOISE and NOISE-CON Congress and and NOISE-CON Congress and Conference Proceedings, Institute of Noise Control Engineering, 2015, pp. 17-28.

Poster,

- Z.N. Ahmadabadi, F. Laville, R. Guilbault, Development of an advanced noise source identification technique for pneumatic nail guns, 2nd prize in the poster competition of ÉREST –AQHSST, January 2015.

2- Investigating the tribodynamics of nail penetration into wood and empirical modeling of the nail-wood penetration resistance force.

Journal article,

- Z.N. Ahmadabadi, F. Laville, R. Guilbault, An empirical prediction law for quasi-static nail–plywood penetration resistance, Construction and Building Materials, 88 (2015) 126-133.

3- Dynamic modeling of the pneumatic nailing devices.

Journal article,

- Z.N. Ahmadabadi, F. Laville, R. Guilbault, Nonlinear dynamic modeling of pneumatic nailing devices, submitted to the journal of Dynamics Systems Measurement and Control (2016).

CHAPTER 1

ARTICLE 1: TIME DOMAIN IDENTIFICATION AND RANKING OF NOISE SOURCES IN A PNEUMATIC NAILING PROCESS

Z. Nili Ahmadabadi[a], Frédéric Laville[a], Raynald Guilbault[a]

[a] Université du Québec, École de technologie supérieure, Department of Mechanical Engineering, 1100 Notre-Dame Street West, Montreal, Quebec, Canada H3C 1K3

This article has been submitted to the Journal of Applied Acoustics in February, 2016

1.1 Abstract

This paper investigates the noise sources in a pneumatic nailing process. The study combines two complementary experimental approaches. The first uses time-synchronized data analysis, with sound, acceleration and air pressure signals simultaneously recorded in conjunction with a nailing device motion high speed video. This strategy allows the identification of the physical processes involved in the operation of the machine at different time instants, as well as the associated noise generation mechanisms. However, since multiple noise sources radiate at the same time, this observation technique is not sufficient for noise source identification and ranking. Thus, a second approach introduces a selective wrapping and muffler procedure, and the strategy assures a reliable classification of the noise sources. The investigation considers the following noise origins: the air exhaust, the machine body and the workpiece/worktable.

In the standardized setup, the workpiece is placed in a sandbox to minimize its noise contribution. Since the final efficiency of this setup has never been established, the study evaluates the sandbox efficiency and compares it with a more realistic test arrangement, where the workpiece is placed on a worktable. The analysis shows that the sandbox setup does not sufficiently attenuate the workpiece noise. With the worktable setup, the workpiece/worktable noise source appears as the main contributor to the total emitted noise, while the air exhaust and the machine body noise are ranked as the second and third sources,

respectively. With the sandbox setup, the workpiece noise is reduced, but remains the dominant source with the air exhaust, in equal measure.

Keywords: Pneumatic nailing device, Noise sources, Nail penetration, Selective wrapping and muffler

1.2 Introduction

Pneumatic nailing devices, which are commonly used in the construction industry, emit noise at levels high enough to put workers at risk of hearing loss. A first step towards noise reduction at the source is an accurate identification of noise generation processes.

The objective of the present research is to identify and rank the noise sources in a pneumatic nailing process. In the standardized setup used for the measurement of noise emissions by nailing devices (BSI, 1999), the workpiece is a wooden block placed in a sandbox to minimize its noise contribution and obtain the nailing device noise itself. This raises two questions: (1) Is the sandbox setup efficient in reducing the workpiece radiation? (2) What is a typical workpiece contribution at an actual worksite? To answer these questions, the noise source identification is conducted in two cases, the standardized sandbox setup, and a more realistic arrangement, where the workpiece is placed on a worktable.

Although numerous publications are available covering noise sources in various machines and systems (Akay, 1978; Alonso et al., 2014; Badino et al., 2016; Bi et al., 2015; Campillo-Davo et al., 2013; Hodgson and Li, 2006; Kim et al., 2007; Koruk and Arisoy, 2015; Leclère et al., 2005; Lee et al., 2012; Lefebvre and Laville, 2008; Pallas et al., 2014; Pallas et al., 2011), only three studies (Adelberg et al., 2002; Jayakumar et al., 2015; Tisserand and Triomphe, 2011) have examined the noise problem in pneumatic nailing devices. Adelberg et al. (2002) used a simple experimental setup, in which one microphone captures the sound at the operator position to identify the noise sources. The authors distinguished four noise peaks in the sound pressure time history of the process. They attributed these peaks to the following four sources: (1) air exchange after trigger pulling, (2) piston impact with low piston bumper, (3) air exhaust, and (4) piston return impact.

Tisserand and Triomphe (2011) evaluated the noise reduction obtained during the air exhaust phase when using a silencer device. Recently, Jayakumar et al. (2015) used sound pressure time history and noise maps to determine the possible noise sources and the corresponding transmission paths. In the investigation, the workpiece was supported by a sand bed. The authors identified the impact noise transmitted through the structure and the exhaust-related noise as the first and second contributors, respectively, to the total noise. The study also identified four distinct peaks in the noise time history. The authors associated these peaks with the following sources: (1) compressed air flow through inlet port, (2) piston rod-nail impact, (3) nail-wood impact, and (4) air exhaust. The present study develops a time domain noise source identification strategy similar to the procedure introduced in Jayakumar et al. (2015) and Adelberg et al. (2002) and completes it by a selective wrapping and muffler procedure.

To identify the noise sources at different time instants, the study carries out a comprehensive experimental time domain analysis of the nailing device operation. The time domain identification uses time-synchronized data analysis: sound, acceleration and air pressure signals are simultaneously recorded, in conjunction with high speed video of the nailing device operation for post-process analysis. This strategy allows the identification of the physical processes involved in the machine operation at different time instants, as well as the associated noise generation mechanisms at play. However, since multiple noise sources possibly radiate at the same time, this observation technique is limited in the number of sources it can identify and rank. Thus, it is completed by a second approach, namely, a selective wrapping and muffler procedure. This strategy assures a reliable classification of the noise sources during the entire nailing operation. These two complementary experimental approaches are detailed in section 1.4, following a description of the nailing device operation in section 1.3. Section 1.5 presents the analysis of the test results.

1.3 Nailing device operation

Figure 1.1 shows a schematic representation of a pneumatic nailing device. When the trigger valve (20) is in the released position, the compressed air covers the area above the

head valve (10). The resultant force of the air pressure on both sides of the head valve and the compression spring (4) downward force keeps the head valve pressed against the cylinder top (5). Depressing the trigger closes the trigger valve, and stops the air flow to the upper area of the head valve. The remaining compressed air in this area flows out to the atmosphere through the air channel (1). As a result, the head valve opens, while simultaneously closing the air exhaust (7). Therefore, the compressed air flows to chamber no.1 (2) above the piston head, pushes the piston downward, and drives out the nail. As the piston moves downward, the air inside the cylinder flows through a series of holes to a return chamber (15). Releasing the trigger valve allows a backward motion of the head valve, which stops the compressed air discharge to the piston head, and opens the air exhaust. The pressurized air inside the return chamber then drives the piston upward, while pushing the air above the piston to the atmosphere (Air exhaust phase) simultaneously.

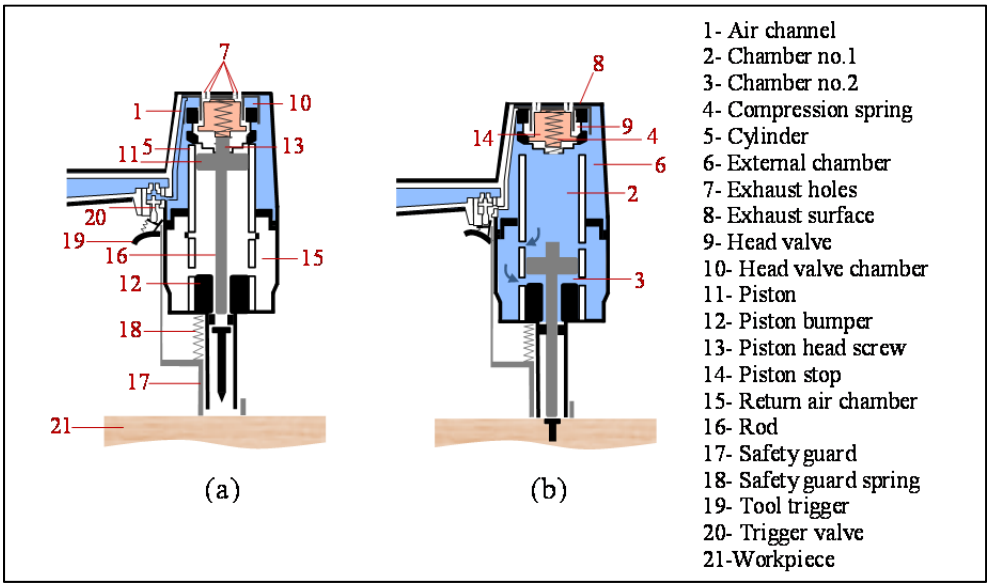

Figure 1.1 Schematic representation of a pneumatic nailing device:
(a) at rest, (b) during the driving stroke

1.4 Experimental Procedure

In previous study (Ahmadabadi et al., 2015b), the authors investigated and formulated the tribo-dynamic interactions developing between wood-based products and metal nails

during penetration at quasi-static velocities (20-500 mm/min range). The investigation published in Ahmadabadi et al. (2015a) demonstrates that the nail size, nail type, and wood type have only a negligible influence on the force, the noise and the vibrations generated during the nail penetration. Therefore, the present study only includes smooth shank nails (illustrated in Figure 1.2(a)) of 12d penny size that have a length of 82.55 mm (3.25 inch) and a diameter of 3.81 mm, all driven by a Bostitch N80 CB-Coil framing nailer.

1.4.1 Test wood specimens

The analysis concentrated on solid wood, and involved only dry pinewood specimens, with a straight grain, and being free of knots. The specimen size was chosen to reduce the boundary influence on the penetration process. According to preliminary tests (not included here), the optimal size $W \times L$ was 152.4 mm $\times$ 406.4 mm (6 inch $\times$ 16 inch), while, to avoid perforation, the thickness (t) was set to 95.25 mm (3¾ inch) (Figure 1.2(b)).

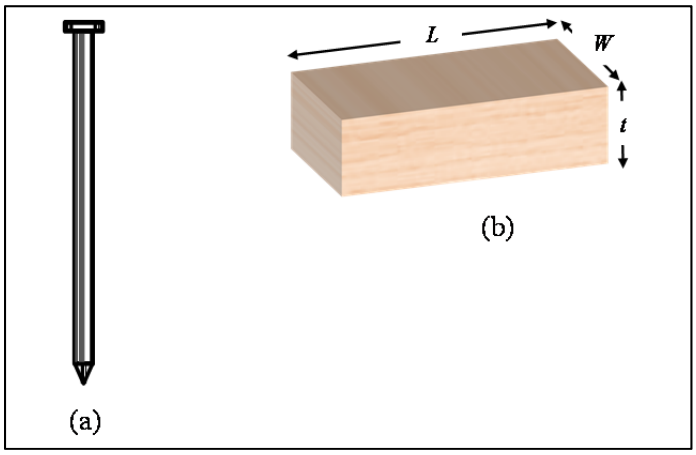

Figure 1.2 (a) Smooth nail, (b) Pinewood specimen

The hardness modulus, density, and moisture content of the wood specimens were measured according to the standard D1037-12 (ASTM, 2012) and standard D4442-07 (ASTM, 2007). Table 1-1 shows the values obtained. The moisture contents shown inTable 1-1 are similar to the conditions encountered in the construction industry.

Table 1-1 Hardness modulus, density values, and moisture content

	Pine
$\boldsymbol{H_M(\mathrm{N/mm})}$	383.64
$\boldsymbol{\rho(kg/m^3)}$	429.46
Moisture content (%)	5.6

1.4.2 Experimental Setups

As mentioned in the introduction, the tests were conducted using two different test setups: a standard sandbox setup and a worktable setup. For the sandbox option, the tests were carried out according to BSI (1999). This standard aims to eliminate or, at least, minimize the noise emanating from the workpiece: the workpiece is settled in dry sand, with its upper surface at the sand level, and the wood fibers are aligned with the sand bed width direction. The sand bed dimensions ($w \times l \times h$) shown in Figure 1.3(a) are 600mm×600mm×400mm. While the arrangement aims to isolate the tested device, in real working environments, the nailed wood parts usually also contribute significantly to the global sound level. Therefore, the investigation integrated a second setup, where the wood specimen was placed on a worktable (Figure 1.3(b)). This support reproduces more realistic testing conditions. The worktable dimensions ($w \times l \times h$) were 450mm×400mm×670mm (Figure 1.3(b)). The workpiece fibers were once again aligned with the worktable width direction. Moreover, to eliminate the extra noise generated by possible collisions at the worktable base/ground contact points, the worktable legs were glued to the ground. Figure 1.4 and Figure 1.5 present the worktable and sandbox experimental setups, respectively.

The measurements were all conducted in a semi-anechoic chamber. The nailing device operating air pressure was set to 763.2 kPa, which allowed the entire nail length (including the nail head) to penetrate the wood. The data was acquired at a sampling rate of 160 kHz.

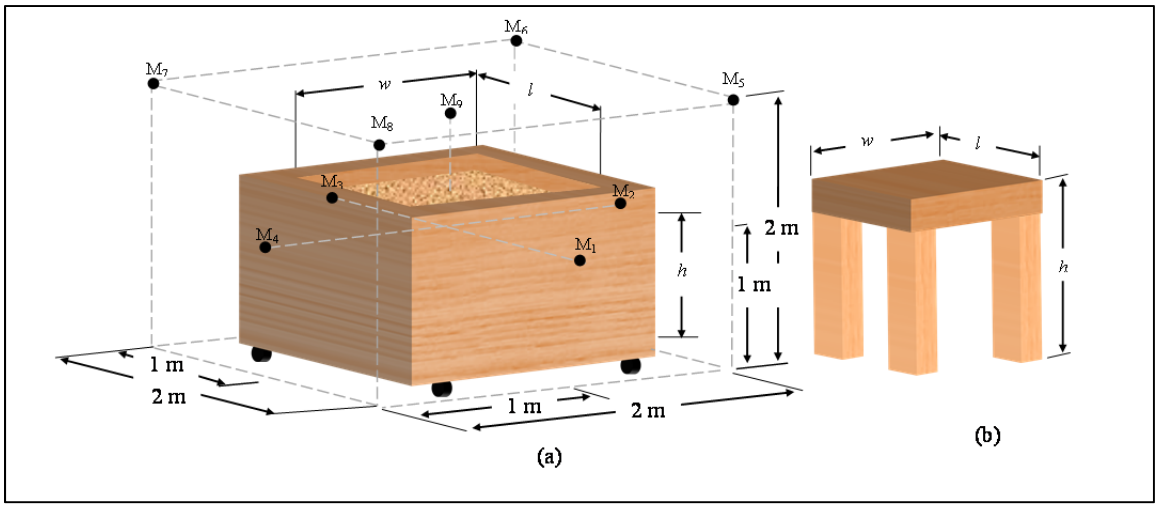

Figure 1.3 (a) Sandbox and microphone positions for sound power measurements, (b) Worktable

1.4.2.1 Time-synchronized data analysis technique

According to BSI (1999), a hypothetical parallelepiped simulated by a nine-microphone arrangement recorded the emitted sounds to measure the process sound pressure. The microphones positions are shown in Figure 1.3(a).

One accelerometer placed on the nailing device handle (Accelerometer-N in Figure 1.4) captured the nailing device acceleration in the penetration direction. The sandbox setup included two addition nail accelerometers mounted on the workpiece in the penetration direction (Accelerometers-W) and on the sandbox edge (Accelerometer-SE) (Figure 1.5). The worktable setup also included two additional accelerometers mounted under the worktable in the penetration direction: at the worktable center (Accelerometer-TC) and at the worktable edge (Accelerometer-TE) (Figure 1.4).

Two piezoelectric pressure transducers were incorporated into the nailing device to measure the air pressure variations inside the cylinder (PT-I) and return chambers (PT-R) (Figure 1.6). The maximum piston stroke was 121.25 mm; the cylinder chamber pressure transducer was placed at 50.51 mm from the stroke beginning. The transducer position and

installation method were selected to avoid perturbing the flow rate and the external chamber volume.

Figure 1.4 also shows the high speed camera integrated into the setup to capture the process motion (10,000 frames/sec). While the main data acquisition system recorded all the microphone, accelerometer and pressure transducer signals, the high speed camera had its own independent data acquisition system. The two were synchronized through the main data acquisition system. To begin the acquisition just before the nailing device operation, the tested nailing device was equipped with a trigger device (push-button switch) located under the nailing device trigger valve (Figure 1.4).

The nailing device operation requires the safety guard to always remain in contact with the wood piece. Filming the penetration process therefore appears impracticable, as the safety guard hides the nail. Preliminary tests indicated that carving 6.35 mm grooves in the wood specimen (Figure 1.4) solves this issue. The tests also demonstrated that the groove had no visible impact on the measurements. However, when penetrating the no-groove wood specimens, the nail penetration started sooner and lasted for a longer time period. The average penetration velocity was also slightly lower (Ahmadabadi et al., 2015a).

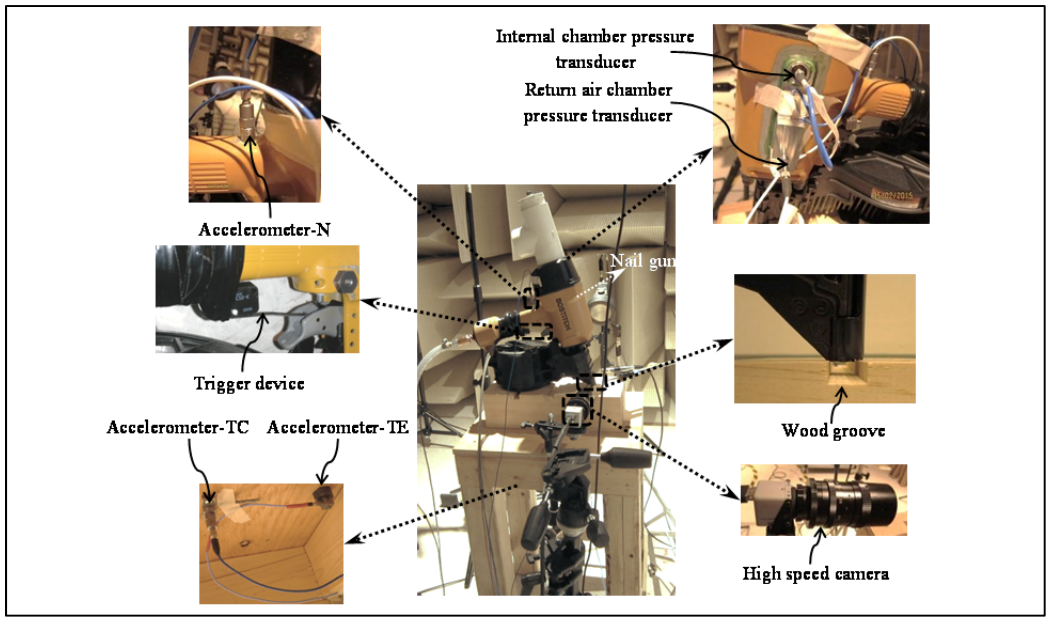

Figure 1.4 Worktable experimental setup for the time-synchronized data analysis technique

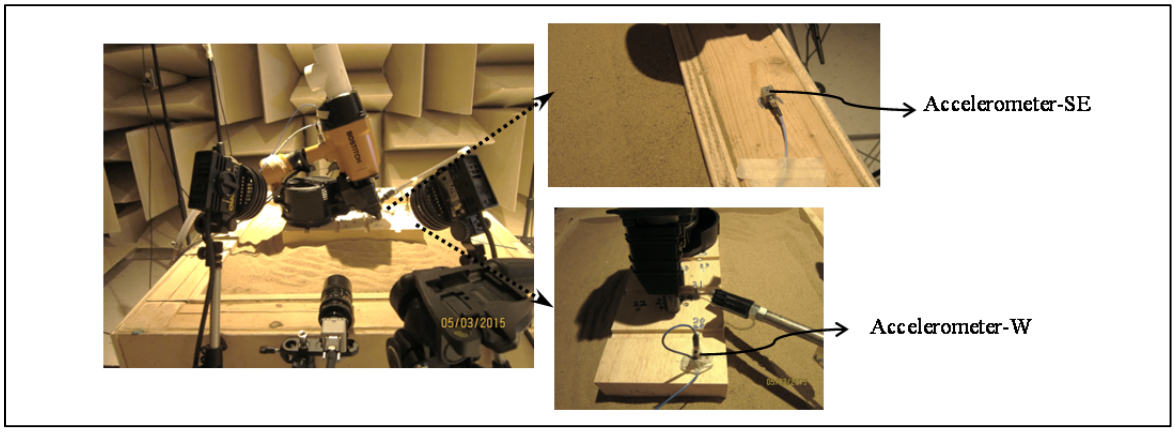

Figure 1.5 Sandbox experimental setup for the time-synchronized data analysis technique

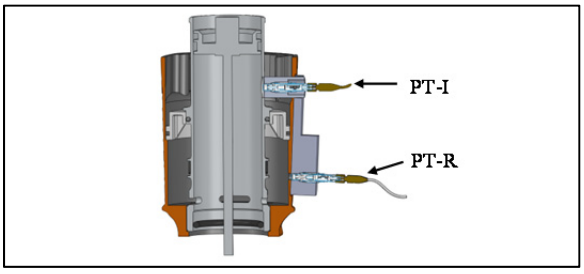

Figure 1.6 Section view of the nailing device instrumented with pressure transducers

1.4.2.2 Selective wrapping and muffler technique

This technique allows the measurement of the sound pressure and the determination of the sound power level of the following noise sources: (1) the air exhaust, (2) the machine body, and (3) the workpiece (sandbox setup) or the workpiece/worktable (worktable setup).

The air exhaust source comprises the air exhaust noise and other radiation sources activated by the exhaust process, such as the air exhaust surface and the nailing device cap (8 in Figure 1.1). In practice, the resulting radiation is detectable before, during and after the air exhaust phase. The machine body noise source encompasses all the noise radiation through the machine body or from different internal/external parts of the machine (except the air exhaust surface and the nailing device cap), caused by the internal air movements/exchange, and due to the impact between surfaces, such as the impact between the head valve and the cylinder surface. Finally, the workpiece noise source is limited to the radiation emanating from the vibrating surface of the workpiece, while the workpiece/worktable noise source includes the noise radiating from the vibrating workpiece and worktable surfaces.

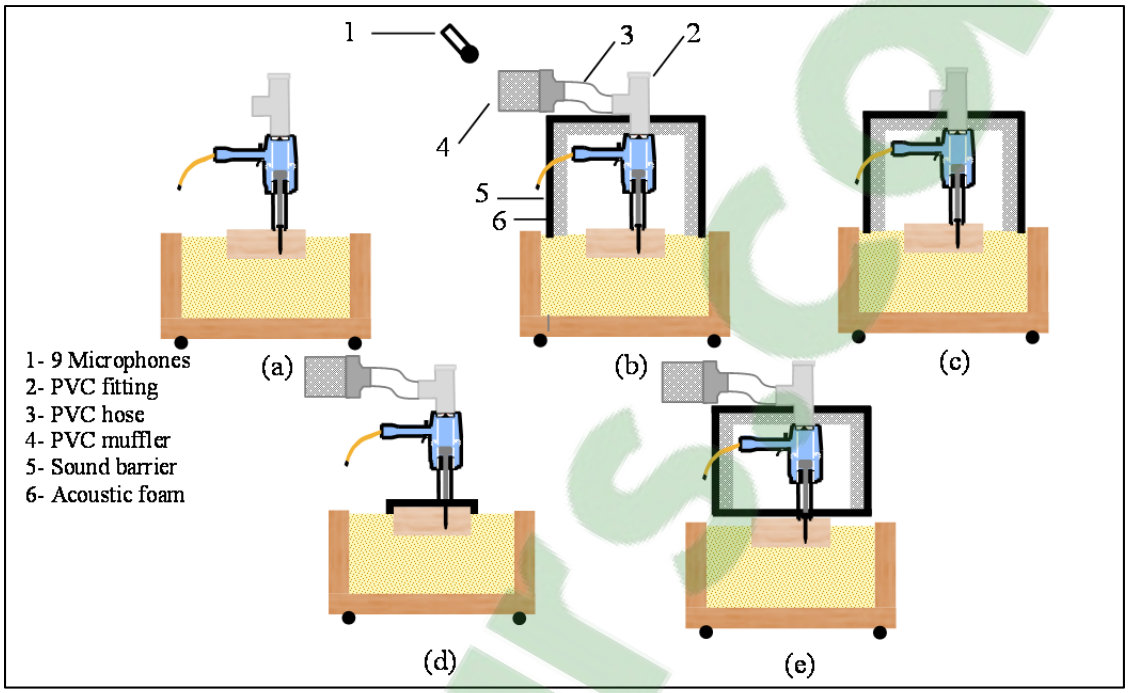

Figure 1.7 Selective wrapping and muffler technique in the Sandbox setup case: (a) total noise (Conf.S-1), (b) residual noise measurement (Conf.S-2), (c) air exhaust noise measurement (Conf.S-3), (d) machine body noise measurement (Conf.S-4), (e) workpiece noise measurement (Conf.S-5)

The selective wrapping and muffler approach comprises five steps, as illustrated in Figure 1.7 and Figure 1.8: Step 1) The total noise (all noise sources) was measured for both setups (Confs. W-1 and S-1); Step 2) The residual noise measurement, where all noise sources were isolated (Confs. W-2 and S-3). For Step 2), absorbing foams and sound barriers were wrapped around the machine body and workpiece/worktable noise sources, and a PVC muffler made of a thick-wall PVC pipe (diameter 150 mm and length 1.5 m) filled with acoustic foams was connected to the nailing device via a PVC hose (length 50 mm) and PVC pipe fittings to remove the air exhaust noise source (Figure 1.7). To maintain comparable test conditions, the PVC pipe fitting installed onto the nailing device remained on the device during the complete test series (see Figure 1.4 and Figure 1.5). To measure the noise associated with the different noise sources, the sources in Step 1) were exposed in Steps 3) to 5), one at a time.

As with the time-synchronized data analysis, the sound pressure was also measured using the nine microphones located at their standard positions (BSI, 1999). Accelerometers-N and -SE (sandbox setup) or Accelerometers -TC and -TE (worktable setup) were also recorded during all tests. Finally, because of the wrapping, the high speed camera could not be integrated into this arrangement. Therefore, the tests were realized with no-groove specimens.

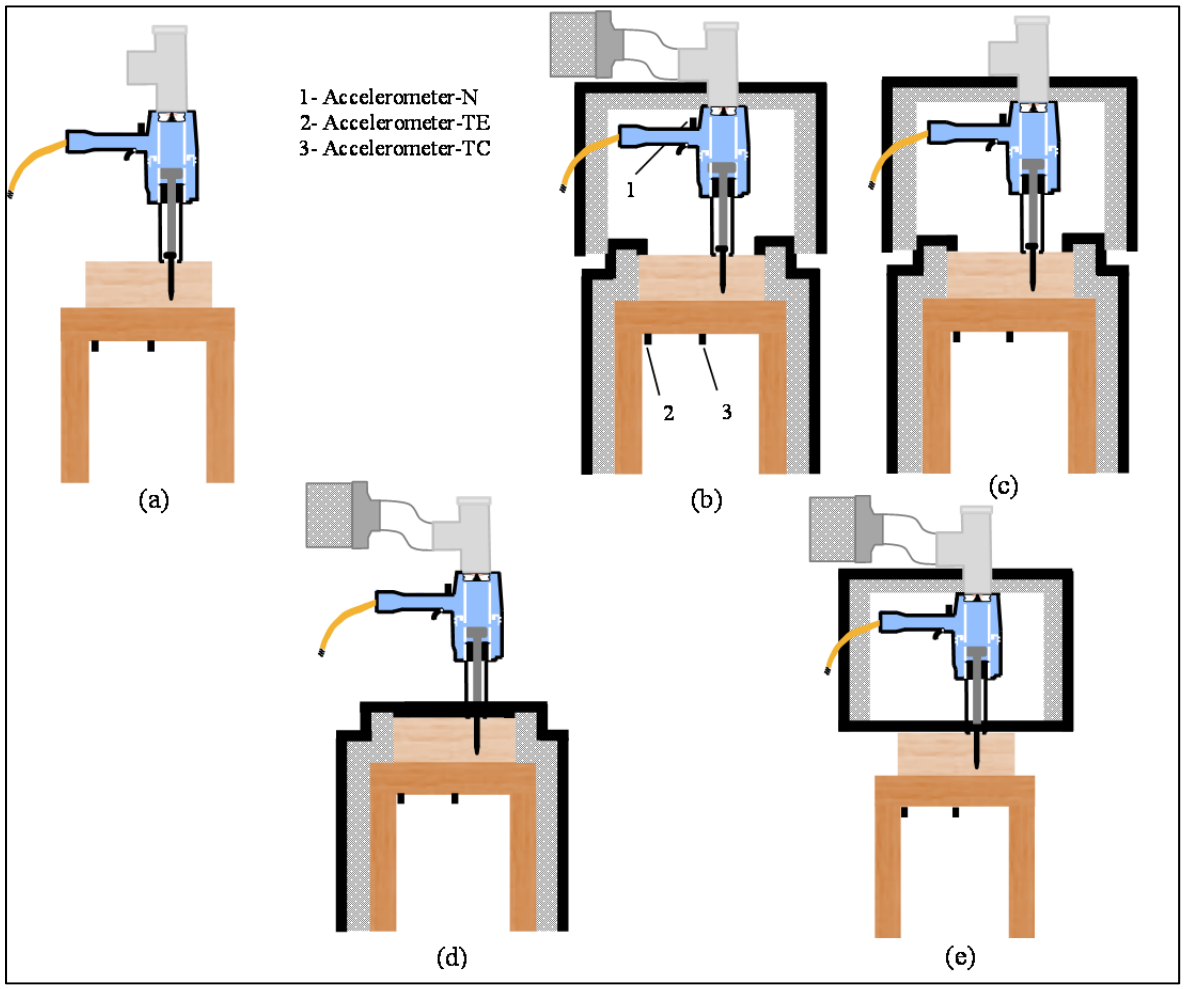

Figure 1.8 Selective wrapping and muffler technique in the worktable setup case: (a) total noise (Conf.W-1), (b) residual noise measurement (Conf.W-2), (c) air exhaust noise measurement (Conf.W-3), (d) machine body noise measurement (Conf.W-4), (e) workpiece/worktable noise measurement (Conf.W-5)

1.5 Results

The following sections analyze and aggregate the results obtained from the two complementary experimental approaches. The two setup versions are studied separately and then compared.

1.5.1 Time-synchronized data analysis approach

1.5.1.1 Worktable setup

Figure 1.9 shows typical signals obtained for the transducers. The charts include only the sound captured by microphone no. 5 (see Figure 1.3) situated at a corner of the hypothetical parallelepiped covered by the standard microphone arrangement (at 1.73 m from the device geometric center). Moreover, given the high repeatability observed during the tests, the signals are only presented for one test.

The time position t_0 to t_{13} marked on the signals shown in Figure 1.9 indicate the important events taking place during the nailing operation. Table 1-2 describes the event associated with the time markers t_i. Since the microphones are placed at prescribed standard distances from the nailing device geometric center, the microphone-signal time markers (Figure 1.9(a)) showed a delay with respect to the other transducers. In order to align the time markers of all graphs, the microphone-signal graph was shifted to the left by the amount of the time delay. The time markers were determined in two ways: (i) points t_0, t_2-t_4, t_6-t_8, t_{10}, and t_{13} were directly identified via the high speed videos or the signals, while (ii) points t_1, t_5, t_9, t_{11}, and t_{12} were calculated from the physical dimensions of the nailing device's internal parts, in combination with the videos and measured signals.

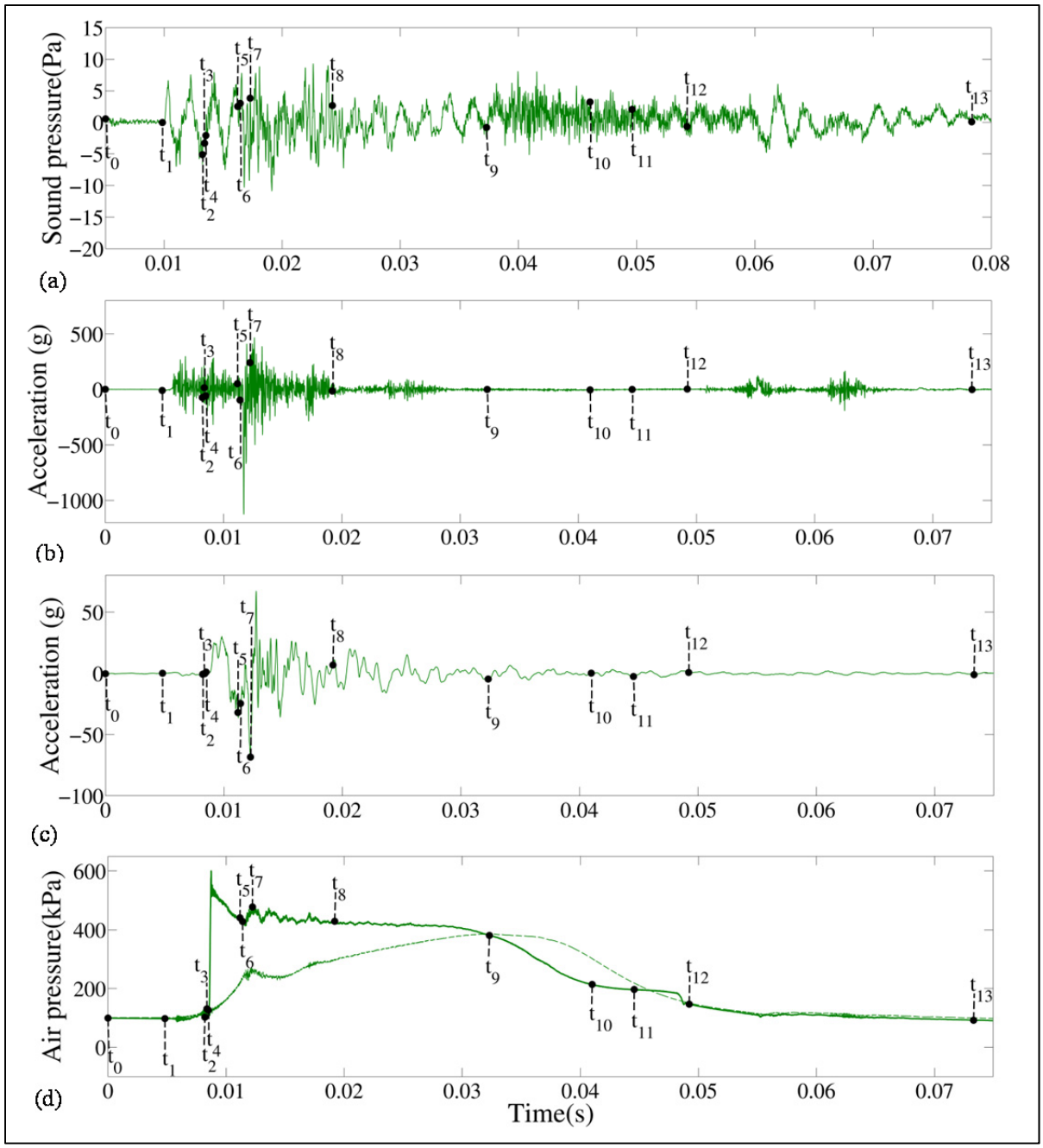

Figure 1.9 Transducer signals for the worktable setup: (a) sound pressure-Microphone no. 5, (b) acceleration-Accelerometer-N, (c) acceleration-Accelerometer-TC, (d) Air pressure: cylinder chamber (solid line) and return chamber (dashed-line)

Table 1-2 Identified events during nailing device operation

Point no.	Event description
t_0	The nailing device trigger is completely pressed down
t_1	Start of piston downward movement
t_2	Start of nail penetration into workpiece
t_3	Start of workpiece vibrations (|Acceleration|≥2g)
t_4	Start of pressure measurement in cylinder chamber
t_5	Air starts to flow from cylinder chamber to return chamber
t_6	End of nail penetration
t_7	Maximum worktable center vibration amplitude (worktable setup) or workpiece (sandbox setup)
t_8	End of cylinder chamber pressure fluctuations
t_9	Equilibrium position between upward and downward forces acting on piston
t_{10}	Nailing device acceleration (Accelerometer-N) becomes negligible |acceleration|<6g
t_{11}	End of chamber no. 1 pressure measurement
t_{12}	End of piston upward stroke; increase in nailing device acceleration (Accelerometer-N) |acceleration|>6g
t_{13}	End of nailing device acceleration signal (|Acceleration|≤6g)

The following describes the time intervals defined by the time markers introduced in Table 1-2. The different effects taking place during these intervals determine the noise generation mechanisms.

Period t_0-t_1: Pulling the trigger at t_0, releases the compressed air from above the head valve to the atmosphere, opens the head valve (closes the air exhaust), and consequently, opens the air path to the cylinder chamber. The pressurized air release from above the head valve, as well as the air flow to the cylinder chamber, constitute the main sound radiation mechanism during this period.

Period t_1-t_2: Slightly after t_1, the rod impacts the nail. The nail penetration starts at t_2, at which point the rod is subjected to the nail penetration resistance. This penetration force consists in the friction and rapid fracture/deformation of the workpiece. During this time

period, in addition to the air movement and exchange between the cylinder and external chambers, the impact between the head valve and the nailing device cap internal surface, the impact between the rod and nail and the associated upward reaction on the rod, the friction force caused by the downward piston-rod assembly movement generate the measured vibrations and noise radiations. The associated ejection of the air trapped between the head valve and nailing device air exhaust surface also generates noise.

Period t_2-t_5: Shortly after the nail penetration begins, the workpiece starts vibrating. Point t_3 is associated with this start. For the worktable setup, the workpiece vibrations start slightly sooner than the worktable vibrations. In addition, the ongoing air movement/exchange between the cylinder and external chambers still contributes to the noise generation. These mechanisms are believed to be the dominant mechanisms during this period.

Period t_5-t_6: Between t_5 and t_6, the nail continues to penetrate into the workpiece, and at t_5, the air starts flowing to the return chamber. The nail penetration ends at t_6. Additional nail driving tests conducted on both the plain and grooved wood showed that, for a 12d nail size, the piston does not impact the bumper at the end of the stroke.

Period t_6-t_8: The end of the nail penetration is associated with an important augmentation of the force imposed on the nailing device. This force increase results from the nail head/wood contact and the elastic force restoration from the wood. This force pushes the nailing device upward, and as a result, the safety guard starts reverting to its release position. The head valve can be liberated by releasing either the device trigger or the safety guard. According to the high speed videos, under normal conditions, the safety guard release occurs sooner than does the device trigger disengagement. The maximum workpiece/worktable and nailing device accelerations amplitudes are seen shortly after t_6, and result in the maximum sound pressure amplitude. The force rise imposed on the nailing device also generates strong oscillations of the piston-rod assembly, producing air pressure fluctuations in the cylinder and return chambers. The piston oscillations cause impacts between the piston and the bumper. Around t_8, the noise and nailing device vibrations associated with the upward force and piston oscillations are significantly reduced.

Period t_8-t_9: The trigger valve is completely released and the head valve starts closing more rapidly. The air exhaust starts slightly before t_9. The piston return to its upper position starts when the upward force acting on the piston-rod assembly is greater than the downward force (at t_9).

Period t_9-t_{12}: During this time period, the nailing device vibration level is very low, indicating a low level of the friction-excited vibrations induced by the piston upward movement. At t_{11}, the piston crosses the cylinder air chamber pressure transducer PT-I. Therefore, after a traveling distance equal to the entire piston thickness, PT-I measures the air pressure below the piston.

Period t_{12}-t_{13}: The piston head screw strikes the piston stopper at t_{12}, increasing the nailing device vibrations level. The air exhaust ends slightly after t_{12}. The collision between the piston head screw and the piston stopper causes additional vibrations of the piston-rod assembly and of the machine body. These vibrations last until t_{13}.

1.5.1.2 Sandbox setup

The sandbox setup recommended in BSI (1999) aims to minimize the workpiece vibrations and isolate the nailing device noise. The process phases and the noise generation mechanisms taking place during the sandbox setup tests are equivalent to those described for the worktable. Only the workpiece and worktable noise radiation durations differ; while with the worktable setup, the workpiece/worktable showed low vibration levels after t_9, the sandbox almost completely damped the workpiece vibrations slightly after t_8. The acceleration measurement provides a more descriptive illustration of the sand bed influence. The following compares the acceleration obtained with the sandbox setup to that measured with the worktable setup.

Figure 1.10 compares the acceleration signals measured during one test on the workpiece for both the sandbox and worktable setups (accelerometer W shown in Figure 1.5). In addition, Table 1-3 gives the RMS levels of the acceleration signals evaluated over a 1-second time period. Table 1-3 also includes the acceleration measured at the worktable

central position (accelerometer TC shown in Figure 1.4 and Figure 1.8). Comparing the W and Tc measurements for the worktable setup reveals the occurrence of contact losses between the wood specimen and the worktable.

Table 1-3 results indicate that when compared to the worktable tests, the sandbox reduced the workpiece RMS acceleration level by a little less than 4 g. More interestingly, the Table 1-3 reveals that the sandbox does not completely eliminate the wood specimen vibrations. By extension, it may be assumed that the sandbox does not completely eliminate the contribution of the wood specimen to the total emitted noise. The following section further investigates the final effect of the sand bed.

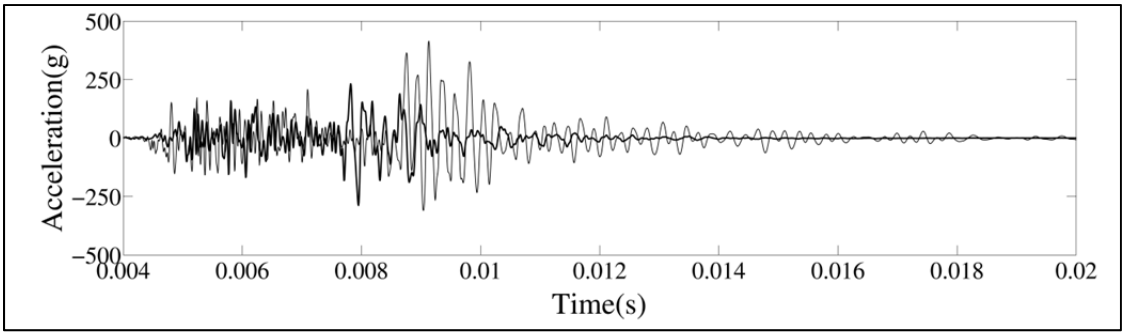

Figure 1.10 Workpiece accelerations: Solid line, worktable setup; Bold solid line, sandbox setup

Table 1-3 RMS level of workpiece and worktable acceleration signals

Setup	**RMS level(g)**	
	Accelerometer W	**Accelerometer TC**
Sandbox	5.33	-
Worktable	9.08	4.70

1.5.2 Selective wrapping and muffler technique

This section presents measurements carried out with the experimental procedure described in section 1.4.2.2. According to BSI (1999), the measurements were all repeated a minimum of five times. The sound power evaluation obtained for the test conditions shown

in Figure 1.7 and Figure 1.8 are first presented. However, while these graphs display the chronological contributions of the different sources, they do not allow a precise comparison or ranking of their contribution to the total noise. Thus, the analysis examines the information presented as an A-weighted single event sound power level normalized to 1 second ($L_{WA,1s}$), which represents the average of these measurements.

The trigger device is designed to start the measurement slightly before the start of the nailing process. However, because of the manual pulling of the trigger, the measurement and the nailing process start are subject to small variations, which are dependent on the operator hand speed. Therefore, to compare the different measurements in the time domain, the signals needed to be further synchronized. Moreover, the gun trigger valve disengagement plays an important role in starting the air exhaust, and since this operation is also dictated by the operator hand speed, in conjunction with the upward movement of the gun, the measured air exhaust start may vary from test to test; the nailing gun isolation material affects the operator hand movement and increases the nailing device weight. The additional weight opposes the upward force acting on the nailing device between t_1 and t_6, delaying the safety guard release, and consequently, the head valve disengagement. For example, the different measurements made with Confs.W-1 and S-1 showed no significant time difference among the air exhaust starts, whereas the following tests realized with configurations where the nailing device was isolated (Confs. W-2, W -3, W -4, W -5, S-2, S -3, S -4 and S -5) presented time delays as compared to configurations W-1 and S-1. However, during these periods, the noise levels remain very low. The delays were noticeable in the vibrations peaks appearing at the end of the nailing device acceleration signal (between t_{12} and t_{13} in Figure 1.9). These vibrations peaks were related to the end of the air exhaust phase. Thus, to compare the time responses measured for the different configurations, the time signals were shifted to the left by the amount of the corresponding time delay. Finally, it is also important to mention that since the tests did not include the camera, t_6 was calculated from the average penetration velocity estimated for full penetration of the nail length.

1.5.2.1 Worktable setup

Figure 1.11 presents the sound pressure evaluation obtained for the five tested conditions described in Figure 1.8. Figure 1.12(a) compares the 1/3 octave band values of $L_{WA,1s}$ established for the different noise sources from the raw measured data. Figure 1.13(a) shows the overall $L_{WA,1s}$ values calculated from the raw data over the time intervals defined by the time markers t_0 to t_{13} of Table 1-2. The graphs include all configurations. The curves in the graphs of Figure 1.13 were established from narrow band FFT. To maintain a constant signal 1 sec. length, the truncated time signals were padded with zeros.

Figure 1.12(a) and Figure 1.13(a) indicate that for some frequencies or time intervals, the residual noise energy comprises a non-negligible part of the measurement. Therefore, to improve the comparison precision, the residual noise contribution is removed from the measurements carried out for the other configurations.

The residual noise elimination procedure corresponds to the spectral subtraction strategy put forward by Boll (1979) for noise compensation and speech enhancement: the energy of the residual noise spectrum is subtracted from the energy spectrum established for all other test conditions. Eq. (1.1) formulates the procedure. In this equation, $Sp(e^{j\omega})$ is the configuration spectrum, $Sp_{rn}(e^{j\omega})$ is the residual noise spectrum, and $Sp_c(e^{j\omega})$ is the corrected configuration spectrum. Eq. (1.1) indicates that the noise subtraction only involves the magnitude spectra, and that the phase of the corrected spectrum is unmodified and equal to the original signal phase $e^{\theta sp\left(e^{j\omega}\right)}$. In order to avoid possible over-subtraction, Eq. (1.1) is completed by a floor factor β. In the present study, β was fixed at 3 dB based on the ISO 3746 standard (ISO, 2010). Thus, any frequency position in $Sp_c(e^{j\omega})$ presenting an amplitude lower than β was set to zero. The corrected time signatures were resynthesized for each source from their corrected spectrum.

$$Spc\left(e^{j\omega}\right)=\left[\left|Sp\left(e^{j\omega}\right)\right|^2-\left|Sp_{rn}\left(e^{j\omega}\right)\right|^2\right]^{\frac{1}{2}}e^{\theta sp\left(e^{j\omega}\right)} \tag{1.1}$$

The corrected 1/3 octave band $L_{WA,1}$ recalculated from the reconstructed time signals are presented in Figure 1.12(b). The narrow band FFT procedure is also reapplied to the corrected time signals. The resulting $L_{WA,1}$ evaluations conducted over the time intervals are shown in Figure 1.13(b). Further, the raw data presented in Figure 1.13(a) indicates that during the time interval t_2-t_6, which corresponds to the nail penetration into the wood specimen, the workpiece/worktable contribution remains low in comparison to the total noise. An underestimation of the workpiece/worktable noise radiation seems to be the reason for this evaluation. In reality, in order to prevent the noise radiation from the machine body, even the nailing device nose was completely isolated in Conf.W-5. As a result, the isolation material bottom surface stayed very close to the wood specimen and partly covered its upper surface, particularly during and just after the nail penetration, or when the nailing device separated from the wood due to the upward reaction. This condition most likely attenuated the wood noise radiation captured by the microphones. The workpiece/worktable noise emission attenuation remained present in the subsequent time periods t_6-t_9.

Similarly, the air exhaust noise is also partly under-evaluated over t_6 to t_9: the low frequency noise visible in Figure 1.11(a) over the period t_8-t_9 does not appear in any other noise source signal. This low frequency noise was presumably generated by the vibrations of the PVC fitting installed on the air exhaust surface (Figure 1.8). On the other hand, the air exhaust noise measurements conducted with Conf.W-3 (Figure 1.11(c)) do not show a corresponding response of the system. In reality, the PVC fitting vibrations were potentially reduced by the nailing device body enclosure wrapped tightly around the lower part of the fitting (Figure 1.8(c)), therefore eliminating the oscillation described in Figure 1.11(a), and causing a corresponding noise emission reduction.

Globally, the underestimation of the workpiece/worktable noise and air exhaust radiation led to a 3.9 dBA difference between $L_{WA,1s}$ of the total noise and the sum of $L_{WA,1s}$ of the different sources. It is almost impossible to distinguish between the workpiece and the air exhaust contribution to this global evaluation. Therefore, neglecting the role of the air exhaust, and incorporating this global estimate into the workpiece/worktable evaluation produces an upper bound sound power level evaluation for the workpiece/worktable source;

summing the energy levels established from the corrected air exhaust and machine body signals and subtracting the result from the energy level of Conf.W-1 produces the upper bound estimation of the workpiece/worktable noise. Figure 1.12(b) and Figure 1.13(b) present the upper bound workpiece/worktable $L_{WA,1s}$ estimates.

Figure 1.12 (b) shows that for $f \leq 0.1kHz$ the workpiece/worktable contribution remains mainly lower than the two other sources, while the air exhaust demonstrates a more significant influence; the machine body energy level only surpasses the air exhaust contribution over $0.4kHz \leq f \leq 0.6kHz$. For frequencies higher than $0.1\,kHz$, the workpiece/worktable contribution shows greater values than the two other sources for practically all frequencies. The maximum power level appears at $0.5\,kHz$ for both workpiece/worktable and air exhaust sources. Above 0.1 *kHz*, the machine body contribution only surpasses the air exhaust power level over the $2.0kHz \leq f \leq 5.0kHz$ range.

The chart in Figure 1.13(b) shows that the air exhaust dominates the measure before the nail penetration, starting at t_2, while the workpiece/worktable represents the main source during the nail penetration (t_2 to t_6), and remains dominant until t_9. Between t_6 and t_9, the machine body contribution surpasses that of the air exhaust. This time period corresponds to significant piston movements and internal air flows, while the air exhaust part remains closed. The air exhaust starts just before t_9. Figure 1.13(b) shows that after this position, the air exhaust contribution preponderates over those of the other two sources.

Finally, based on the results of Figure 1.12(b) and Figure 1.13(b), the worktable setup noise sources can be ranked as follows, in decreasing order of significance: 1- the workpiece/worktable, 2- the air exhaust, and 3- the machine body.

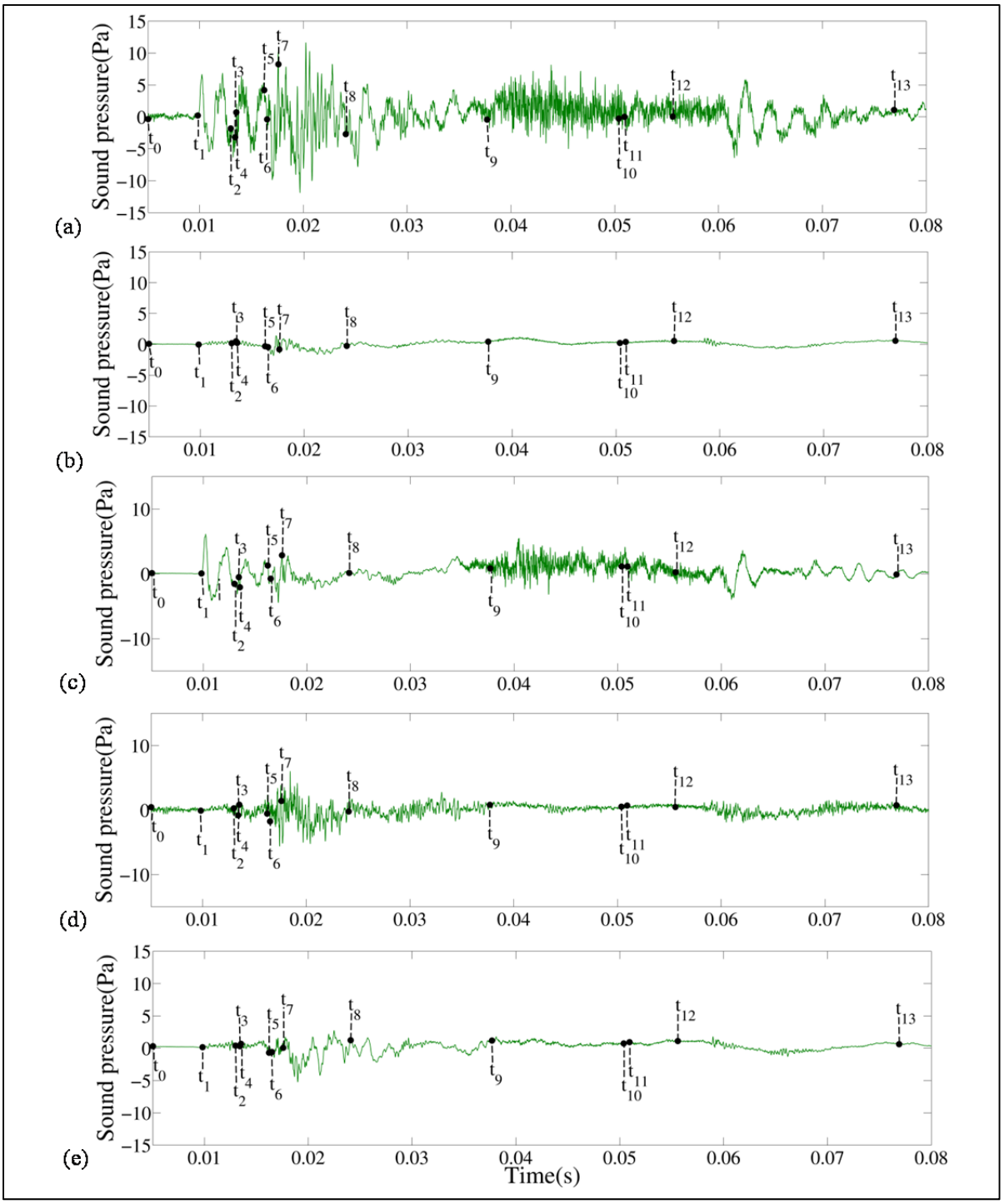

Figure 1.11 Sound pressure Microphone no. 5: (a) Total noise (Conf.W-1), (b) Residual noise (Conf.W -2), (c) Air exhaust noise (Conf.W -3), (d) Machine body noise (Conf.W -4), (e) Workpiece/worktable noise (Conf.W -5)

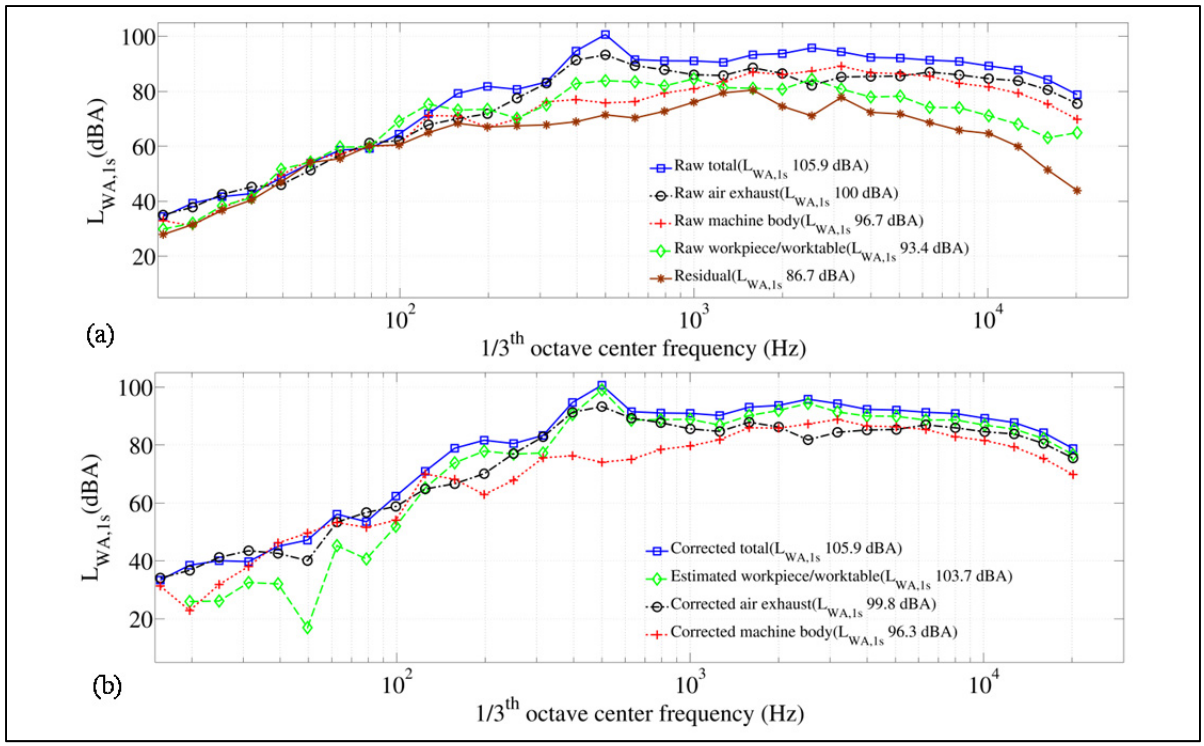

Figure 1.12 1/3 octave band analysis for worktable setup: (a) raw data, (b) corrected data

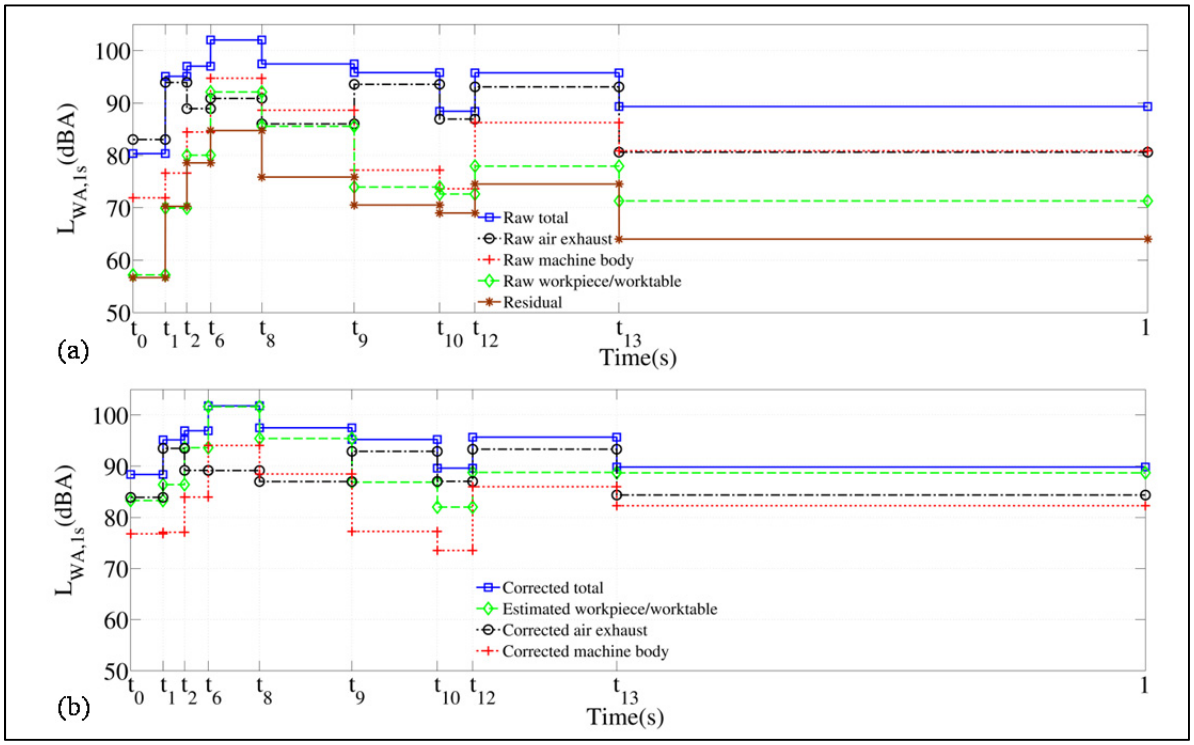

Figure 1.13 Overall sound power level for worktable setup: (a) raw data, (b) corrected data

1.5.2.2 Sandbox setup

Based on the observation made before for the workpiece/worktable setup, this part of the analysis does not present the time plot obtained for the sources. Figure 1.14 presents the 1/3 octave band evaluated for the different sources from the raw and corrected data in (a) and (b), respectively, while Figure 1.15 shows the $L_{WA,1s}$ values calculated over the previously indicated time intervals for the corrected data only.

As was the case earlier, the wood specimen measured noise was attenuated by the nailing device isolation material. The air exhaust contribution was also possibly affected by the nailing device-body enclosure wrapped in the vicinity of the fitting-nailing device connection. Therefore, the procedure described earlier to establish an upper bound of the workpiece contribution helped produce a better estimate of the maximum possible contribution of the wood specimen. The plots in Figure 1.14(b) and Figure 1.15 present this estimated contribution.

The curve in Figure 1.14 show that, as with the worktable setup, the air exhaust noise remains visible throughout the entire nailing process, and remains the dominant source up to 2 kHz. While the machine body contribution demonstrates a signature very close to the response presented in Figure 1.12(b), the workpiece influence is attenuated by the sand bed. However, as already underlined by the acceleration measurements of section 1.5.1.2, the real isolation efficiency of the sandbox appears to be much lower than believed. The maximum power level evaluated for the workpiece and the air exhaust are seen once again around 0.5 kHz. Also as earlier seen, the workpiece contribution surpasses the air exhaust at frequencies above 1.0 kHz. However, in the present situation, this period presents a larger span: 2.0 kHz to 10.0 kHz.

Globally, Figure 1.15 shows evaluations comparable to those of Figure 1.13(b). The air exhaust effect dominates the other sources. On the other hand, while the machine body noise part remains close to the measures presented in Figure 1.13(b), its influence increases over the t_2 to t_9 interval. This time period encompasses the nail penetration effects. In reality, it

may be conjectured that the stiffer support provided by the sandbox in comparison with the worktable reduces the wood specimen vertical displacement, which, in turn, reduces the required piston translation and associated energy consumption for a complete penetration. Therefore, the higher air energy remaining in the nailing device results in larger machine body vibration amplitudes.

Finally, in agreement with previous observations on the isolation performance of the sand bed, Figure 1.15 shows that the specimen contribution dominates the other sources as soon as the nail penetration begins, therefore confirming that the sandbox approach does not offer the expected noise elimination. Figure 1.12 and Figure 1.14 also indicate the overall noise radiations; while the workpiece/worktable value is 103.7 dBA, the workpiece evaluation remains at 100.6 dBA with the sandbox, which is almost equal to the air exhaust contribution (100.5 dBA).

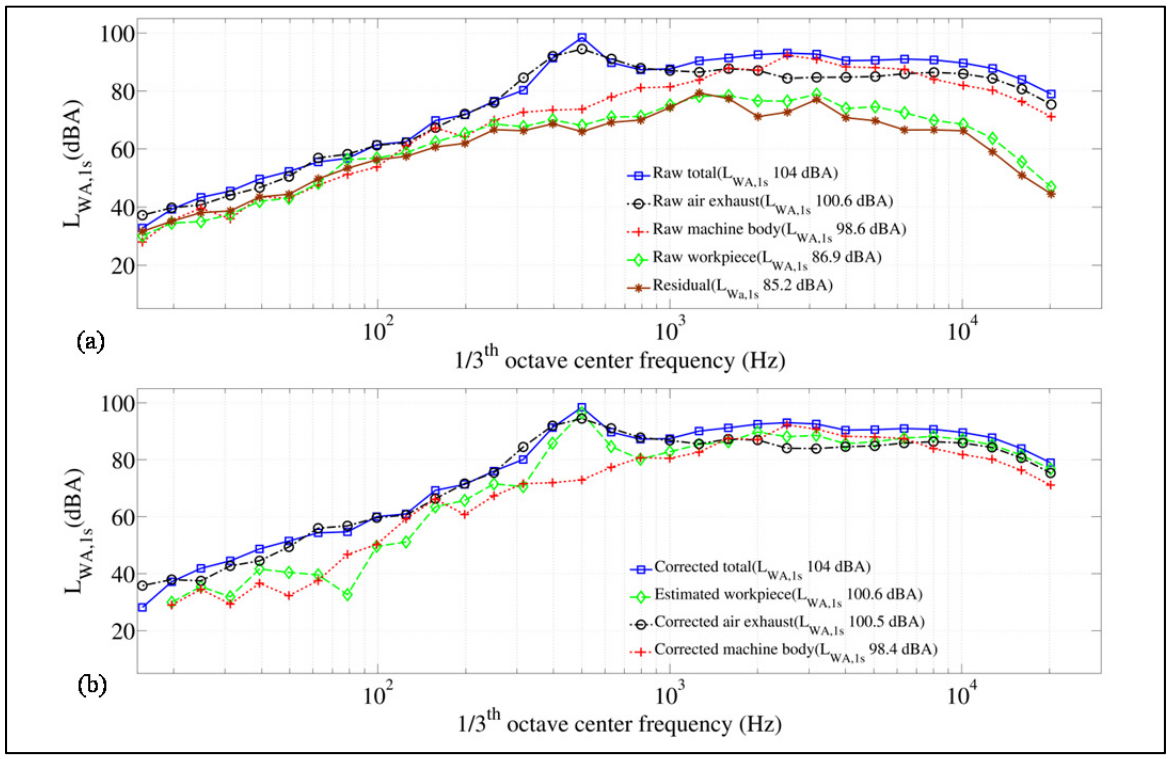

Figure 1.14 1/3 octave band analysis for sandbox setup: (a) raw data, (b) corrected data

To sum up, for the sandbox setup, the air exhaust and workpiece are the dominant noise sources, while the machine body comes in second. Globally, compared to the tests on the worktable setup, the sand bed reduced the overall sound emission of the process by 1.9 dBA.

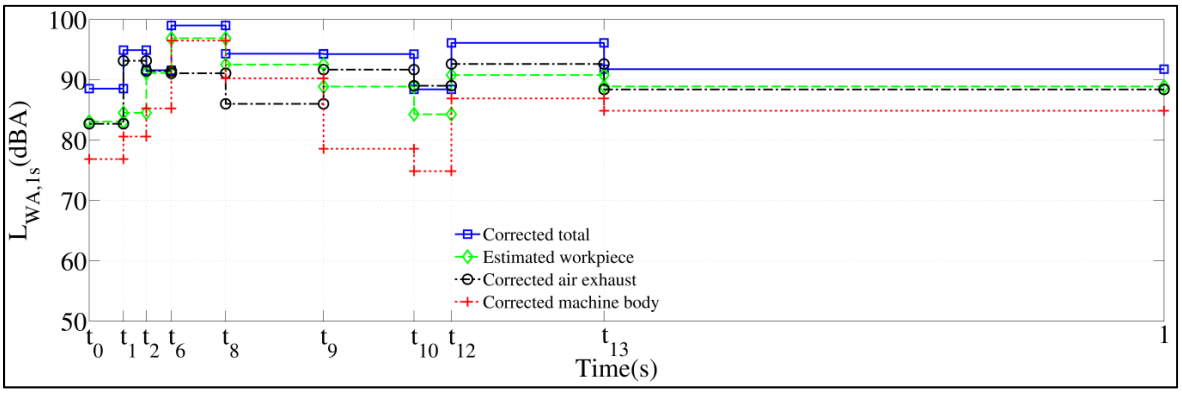

Figure 1.15 Overall sound power level for sandbox setup: corrected data

1.6 Conclusions

The research presented has brought a better understanding of the fairly complex noise generation mechanism in a pneumatic nailing device. The simultaneous observation of data pertaining to several variables during the nail driving process has provided a more detailed separation of the noise generation mechanism in successive time sequences (13 have been identified, versus 4 in previous work). The complementary selective enclosure approach has identified the relative contribution of the three major sources: (1) exhaust noise, (2) machine body vibrations, and (3) workpiece vibrations. A special investigation was conducted on the latter, using two cases: a workpiece/worktable setup representative of the actual field usage of a nailing device, and a workpiece/sandbox setup used in a standardized laboratory test. It was shown that the worktable represented the predominant source (exhaust noise and machine body vibrations being respectively ranked second and third) and, more surprisingly, that the workpiece in the sandbox was radiating at the same level as the exhaust noise source, hence showing that the standardized setup does not reduce the workpiece radiation as expected. A new approach to reducing the workpiece radiation needs to be implemented if

the standard is to efficiently measure the nailing device noise emission without the workpiece contribution.

This study has demonstrated how combining these two approaches provides a better understanding of the noise generation mechanism and an evaluation of their contribution to the total noise generation. Although some small noise reduction can be achieved by using a classical reduction technique, such as a muffler on the exhaust noise, bigger noise reductions will require addressing all three major noise sources, as they are very close in sound power level. The best approach to achieving this will require acting at the nailing device design stage. Design parameters of the nailing device need to be related to the sound generation mechanisms that have been identified, and achieving that will require a remodeling of the nail driving process, which should be covered in future research.

1.7 Acknowledgments

The support of NSERC (Natural Sciences and Engineering Research Council of Canada) is gratefully acknowledged.

CHAPTER 2

ARTICLE 2: AN EMPIRICAL PREDICTION LAW FOR QUASI-STATIC NAIL-PLYWOOD PENETRATION RESISTANCE

Z. Nili Ahmadabadi[a], Frédéric Laville[a], Raynald Guilbault[a]

[a] Université du Québec, École de technologie supérieure, Department of Mechanical Engineering, 1100 Notre-Dame Street West, Montreal, Quebec, Canada H3C 1K3

This article was published in the Journal of Construction and Building Materials in July, 2015

2.1 Abstract

This paper presents an empirical model predicting penetration resistance forces (PRF) imposed on nails when penetrating plywood samples at quasi-static velocities (20-500 mm/min range). The formulation covers various nail geometries and sizes and three plywood types. A universal testing machine was used to drive the nail into the wood samples at constant speeds. The machine measured PRF as a function of the position. The analysis reduces the studied factors to dimensionless parameters. More than 200 experiments were conducted over the parameter space, and the final formulation derives from regressions. Test cases showed an overall precision of PRF prediction above 89%.

2.2 Introduction

The present paper describes and formulates the tribo-dynamic interactions developing between wood-based products and metal nails during fastening process motions.

For centuries, nails have been used to connect wood pieces. Until the emergence of nail guns, which revolutionized the speed of construction in the 50s, hammering was the only nail fastening option. Even though emitted noise may cause health problems, nail guns have been used despite generating high noise levels.

Over the years, the different nail geometries have been modified to make the fastening process more efficient by increasing the withdrawal resistance force and the load resistance of the connections (Stern, 1950a; 1950b; Stern and Blacksburg, 1956a; 1956b). Nevertheless, nail improvements have never been considered from a noise or vibration reduction perspective.

Under normal operation conditions, nail guns generate noises and vibrations. Improving the concept design to reduce the emission levels certainly represents an ineluctable operation. However, modifying the device design requires a precise understanding of its dynamics, as well as the influence of any modification. A dynamic model of the system is therefore essential.

Zhong et al. (2008) presented a simplified mathematical pneumatic nail gun model. The authors simulated the air chamber pressure and considered the piston as acting against a constant penetration resistance force. Later, Hu (2009) examined the gas dynamics influence on the performance of a pneumatic nail gun. This investigation also reduced the nail penetration resistance to a constant force. However, it may be assumed that neglecting the complex tribo-dynamic conditions involved in the nail penetration process affects the model precision.

Despite numerous studies on the resistance of wood-based connections (AITC, 1986; Aytekin, 2008; Branco et al., 2009; Carvalho and Carrasco, 2010; Celebi and Kilic, 2007; Dias et al., 2007; Gong et al., 2014; Lin and LaFave, 2012; Lukaszewska et al., 2008; Mascia and de Oliveira Santana, 2009; Rammer et al., 2001; Tomasi and Sartori, 2013; Wang et al., 2011; Wills et al., 1996; Zarnani and Quenneville, 2014; Zhou and Guan, 2011) have examined nail penetration tribo-dynamic aspects. Villaggio (2005) studied nail penetration into soft materials as a result of hammering. The author idealized the nail as a cylindrical shaft, and developed an analytical formulation of the penetration rate per hammer blow. For their part, Bartelt et al. (1994) employed numerical models to simulate impact penetration of nails driven by power-actuated fastening devices into hard construction materials such as steel or concrete.

Since wood products correspond to highly heterogeneous domains, the precise numerical modeling of such materials results in computationally onerous simulations. Therefore, to ensure precise and rapid representations, the present study derives a nail penetration model from experimental measurements. The objective is to prepare a formulation predicting the nail penetration resistance force as a function of nail size and type. Since this paper is seen as the first part of a broader investigation, the wood products examined are restricted to plywood, and the penetration speed range to quasi-static conditions. To eliminate the possible influence of acceleration, the penetration speed is maintained constant. The measurements are all realized on a universal testing machine. In order to extend the prediction formula application range, the analysis first reduces the studied factors to dimensionless parameters. Section 2.3 describes the experimental procedure. Section 2.4 analyses the penetration resistance force (PRF) results, and presents a parametric study. Finally, the empirical nail penetration model is derived from regression analyses in Section 2.5.

2.3 Experimental procedure

2.3.1 Influential parameters and dimensional analysis

Initial qualitative evaluation indicated that the parameters controlling PRF may be collected in two classes mainly: 1) the size and material properties (parameter set 1), and 2) the penetration process (parameter set 2).

Parameter set 1 includes: 1- the wood density, 2- the wood hardness modulus, 3- the nail geometry type or the nail shank type, 4- the nail diameter, and 5- the nail length. It may be intuitively supposed that parameters 1 and 2 have direct and proportional effects on PRF; denser or harder materials should result in PRF of greater amplitude. While the same information could be deduced from the wood-specific gravity combined with moisture content, the wood density parameter allows a reduction of the number of parameters included in the analysis. The hardness modulus parameter describes the material resistance to

penetration deformation. Moreover, since the steel Young modulus is significantly higher than the plywood Young modulus, the analysis assumes that the nails are perfectly rigid.

Parameter set 2 includes the following two factors: 6- the penetration velocity, and 7- displacement. Investigations on high velocity impact penetration (Goldsmith, 1960) have shown that PRF may be highly affected by the penetration velocity and the penetrating object displacement.

Table 2-1 shows the identified parameters and the corresponding dimensions. *L*, *M* and *T* indicate the length, mass and time units, respectively. Table 2-1 shows that six of the parameters are independent. A dimensional analysis based on Buckingham's π-theorem (Szirtes, 2007) leads to a parameter number reduction. Dimensionless parameters also generalize the validity range of the results. Since the nail shank type cannot be associated with any dimension, it is excluded from the dimensional analysis. PRF corresponds to the dependent parameter, while H_M, *NL* and *v* represent the base parameters. In the following, the variable F_r replaces PRF.

Table 2-1 Parameter sets 1 & 2

	Parameters	**Dimension**
Parameter set 1	1- wood density(ρ)	ML^{-3}
	2- wood hardness(H_M)	MT^{-2}
	3- nail shank type (*ST*)	-
	4- nail diameter (*D*)	L
	5- nail length(*NL*)	L
Parameter set 2	6- penetration velocity (v)	LT^{-1}
	7- displacement (y)	L

Mathematical manipulations not included here yield the following four Π terms (or dimensionless parameters). Combined with *ST*, they describe the investigated space:

$$\Pi_1 = \frac{F_r}{H_M NL}, \quad \Pi_2 = \frac{y}{NL}, \quad \Pi_3 = \frac{NL\rho v^2}{H_M}, \quad \Pi_4 = \frac{D}{NL} \tag{2.1}$$

2.3.2 Test wood specimens

The present analysis concentrates on plywood products. These products are wood-based composite materials made from oriented wood veneers bonded with adhesives. The study includes three plywood categories: (1) Canadian softwood plywood (*CSP*), (2) Douglas-Fir plywood (*DFP*), and (3) Poplar plywood (*PP*). Figure 2.1 (a) shows a plywood panel specimen. The specimen size is chosen to reduce the boundary influence on the penetration process. According to preliminary tests (not included here), the optimal size (Width X Length) is 152.4 mm x 406.4 mm (6 inch x 16 inch), while to avoid perforation by the longest nail specimen, the thickness is set to 95.25mm (3¾ inch). Given that the maximum panel thickness is 19.05mm (¾ inch), 5 panels are screwed together, as shown in Figure 2.1 (b).

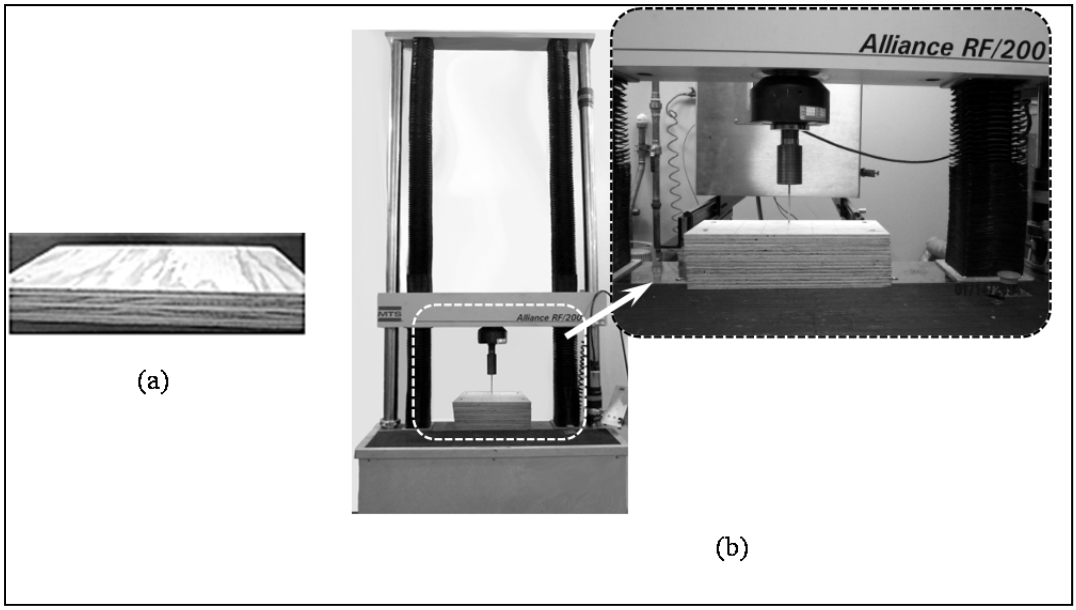

Figure 2.1 (a) Douglas-Fir plywood panel, and (b) experimental set-up

The hardness modulus, density, and moisture content of the plywood categories were measured according to the standard D1037-12 (ASTM, 2012) and standard D4442-07 (ASTM, 2007). Table 2-2 shows the measured values. The present analysis only includes dry plywood products. The moisture contents indicated in Table 2-2 are similar to the conditions encountered in the construction industry.

Table 2-2 Hardness modulus, density values, and moisture content

	DFP	***CSP***	***PP***
$\boldsymbol{H_M}(\mathbf{N/mm})$	560.11	371.77	478.96
$\boldsymbol{\rho}(\boldsymbol{kg/m^3})$	543.59	449.71	464.00
Moisture content (%)	5.7	5.6	5.6

2.3.3 Nails

In order to assure a reliable coverage of the nail forms available in the construction industry, the proposed investigation examines three shank types: (1) smooth, (2) annularly threaded, and (3) helically threaded. Figure 2.2 shows the three types. The study also includes a total of seven nail lengths and diameters. Table 2-3 presents the evaluated diameters for each shank type. These parameter values were dictated by industry practice. Table 2-4 indicates the other important nail dimensions.

Table 2-3 Nail shank types

Nail penny size	**Smooth nails**	**Annularly threaded nails**	**Helically threaded nails**
3d	✓	✓	
4d	✓	✓	
6d	✓		
8d	✓	✓	✓
10d	✓	✓	✓

Table 2.3 (Continued)

Nail penny size	Smooth nails	Annularly threaded nails	Helically threaded nails
12d	✓		
16d		✓	✓

Table 2-4 Nail penny sizes

Nail penny size	Nail nominal length (mm) *NL*	Nail nominal diameter *D* (mm) and (Π_4)					
		Smooth nails		Annularly threaded nails		Helically threaded nails	
3d	31.75 (1.25 inch)	2.032	(0.0640)	2.032	(0.0640)	-	-
4d	38.10 (1.5 inch)	2.794	(0.0733)	2.794	(0.0733)	-	-
6d	50.80 (2 inch)	3.048	(0.0600)	-	-	-	-
8d	63.50 (2.5 inch)	3.302	(0.0520)	3.302	(0.0520)	3.048	(0.0480)
10d	76.20 (3 inch)	3.810	(0.0500)	3.810	(0.0500)	3.556	(0.0467)
12d	82.55 (3.25 inch)	3.810	(0.0462)	-	-	-	-
16d	88.90 (3.5 inch)	-	-	4.064	(0.0457)	3.810	(0.0429)

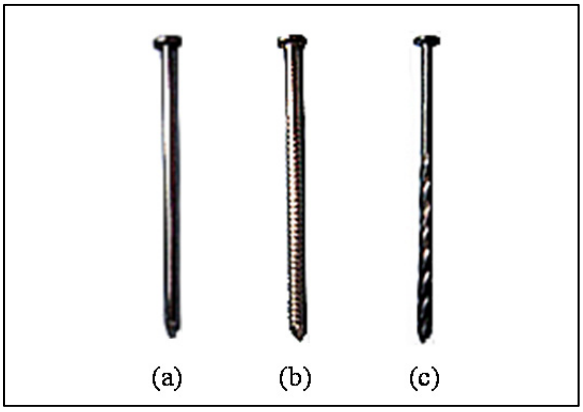

Figure 2.2 Nails: (a) Smooth, (b) Annularly threaded, (c) Helically threaded

2.3.4 Quasi static tests

Constant speed penetration tests were realized on a universal testing machine. Table 2-5 shows the velocities tested for each nail geometry. The tests corresponding to the smooth nail type involve six velocity levels. Since preparatory evaluations with this nail type indicated that under quasi-static conditions, the penetration speed has a moderate influence on the penetration force, the velocity levels were reduced from six to three for nail types (b) and (c). For similar reasons, the velocity levels were not fixed at strict positions imposing a constant separation between them.

Table 2-5 Velocity levels

Nail geometry type	**Velocity levels (m/s)**					
	0.000333	**0.000833**	**0.00166**	**0.00333**	**0.00666**	**0.00833**
Smooth nails	✓	✓	✓	✓	✓	✓
Annularly threaded nails	✓			✓		✓
Helically threaded nails	✓			✓		✓

2.4 Experimental results - general discussion

This section presents a global analysis of the measured values, evaluates the influence of the different parameters, and discusses the data processing.

2.4.1 Measured value analysis

The first part of the analysis compares the plywood response to natural wood, while a second part identifies the force component leading to the measured F_r. Figure 2.3 presents the raw F_r measurements obtained (setup Figure 2.1) for smooth nails in different plywood types and pinewood samples. The pinewood measurements are included in the graph for comparison purposes. They were realized on samples respecting the plywood specimen

dimensions. Figure 2.4 illustrates the nail extremity. On average, the tip portion corresponds to Π_2=0.09.

The graph of Figure 2.3 clearly shows the tip penetration influence ($\Pi_2 \leq 0.09$). In this region, the force increases with a high slope by up to 25% of the maximum F_r value. The shank penetration start causes a slope reduction. The natural wood curve describes a less fluctuating response, and since the selected pinewood sample represents a quasi-homogeneous structure, the fluctuation observed for the plywood curves are assumed to be generated by the composite and heterogeneous nature of the plywood. Because of this particular structure, the panel stacking up generates no significant penetration resistance alteration. In fact, for $\Pi_4 = 0.052$, the panel joints are situated at Π_2 positions equal to 0.3 multiples. The plywood curves in Figure 2.3 do not exhibit any distinct perturbation at those positions.

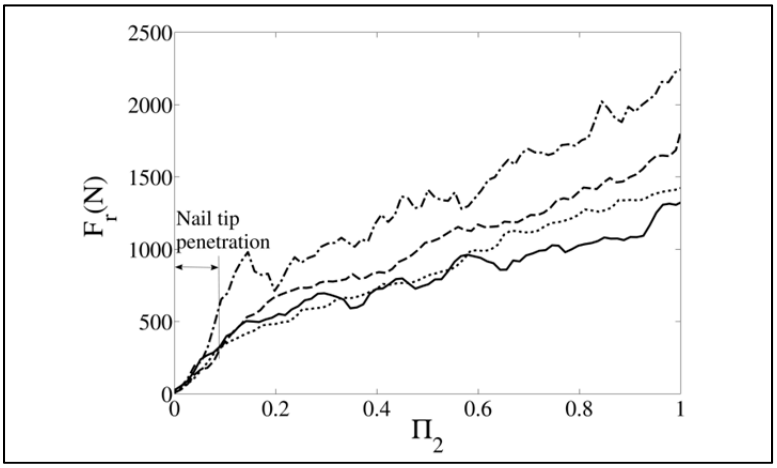

Figure 2.3 F_r curves (nail size: Π_4=0.052, *ST*=smooth, v=8.33x10^{-3}). Solid line: *CSP*; Dotted line: Pinewood; Dashed line: *PP*; Dash dotted line: *DFP*

The measured penetration forces amalgamate numerous sources, the dominant ones being the Coulomb friction and the force associated with the wood deformation-fracture. The following experimental procedure allows the separation of the dominant F_r components. First, the nail is driven into the sample to evaluate F_r, and secondly, the nail is withdrawn, and then driven back into the hole generated during the initial penetration, and the resistance

force is recorded. The initial penetration F_r includes the Coulomb friction and the deformation-fracture components. Following the nail extraction, the remaining resistance force appearing during the penetration is assumed to be entirely generated by the Coulomb friction. Therefore, subtracting F_r measured during the second penetration from the first measurements isolates the wood deformation-fracture force.

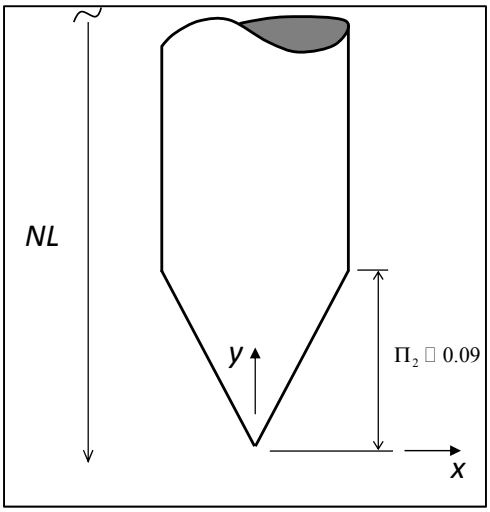

Figure 2.4 Nail extremity

Since the penetration proceeds without any rotation, the experiment is easily carried out for smooth and annularly threaded nails, with their penetration remaining unchanged for the second penetration movement. In contrast, helically threaded nails rotate while penetrating, and depending on the interaction at the wood-nail interface, the rotation appears to be irregular and hardly predictable. Therefore, precise withdrawal involving no alteration of the interface is virtually impossible. For this reason, the experiment only includes the smooth and annularly threaded nails.

Figure 2.5 shows F_r evaluated during the first penetration, F_r measured during the second penetration (or the Coulomb friction force), and finally, the wood deformation-fracture force obtained after subtraction of the friction force from the first force distribution. In addition to the raw data, the graphs include fitted model evaluations. For both nail geometries, the curves indicate that the tip penetration period $\Pi_2 \leq 0.09$ is dominated by the

deformation-fracture force. While this force component remains practically constant at 200 N after Π_2 = 0.1 for the smooth nail, the cross-section increase above the nail tip of the annularly threaded nail extends the deformation influence development up to roughly Π_2 = 0.4, and leads to a maximum value close to 400 N, which remains nearly constant thereafter. On the other hand, the friction forces show a linear influence for both nail shanks. However, since this component results mainly from adhesion at the wood-nail interface, the real contact area reduction resulting from the annular surface of the second shank type decreases the friction contribution compared to the smooth shank. The maximum friction reaches 708 N at Π_2 = 1 for the smooth nail, which corresponds to 81% of F_r, while for the annular shank the friction maximum value is 419 N or 55% of F_r. Finally, based on these observations, and comparing the three nail geometries, it could be conjectured that the penetration resistance force generated by a helically threaded nail should be dominated by an adhesive friction force component.

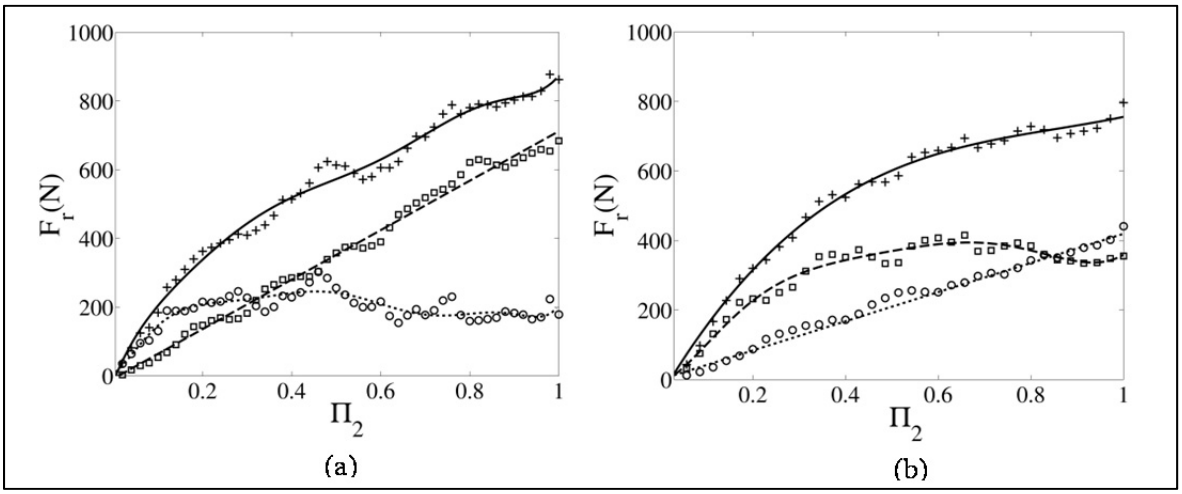

Figure 2.5 F_r constituents (wood type: *PP*, v=8.33x10^{-3} m/s): (a) Smooth nails (Π_4=0.0600), (b) Annularly threaded nails (Π_4=0.0733). Solid line and cross: F_r fitted model and data; Dashed line and square: Friction force fitted model and data; Dotted line and empty circle: Deformation-fracture force fitted model and data

2.4.2 PRF curves treatment

Figure 2.3 evidenced the normal experimental value oscillations resulting from a single test. Therefore, to increase the evaluation stability and reliability, the tests were repeated

seven times for the remaining parts of the study. In addition, instead of the raw data, the following figures present evaluations established with mathematical models fitted to the seven repetitions. To illustrate the data processing outcomes, Figure 2.6 compares the model predictions to the experimental measurements, when a smooth shank type with Π_4=0.052 is driven into poplar plywood (*PP*) at an 8.33x10^{-3} m/s velocity.

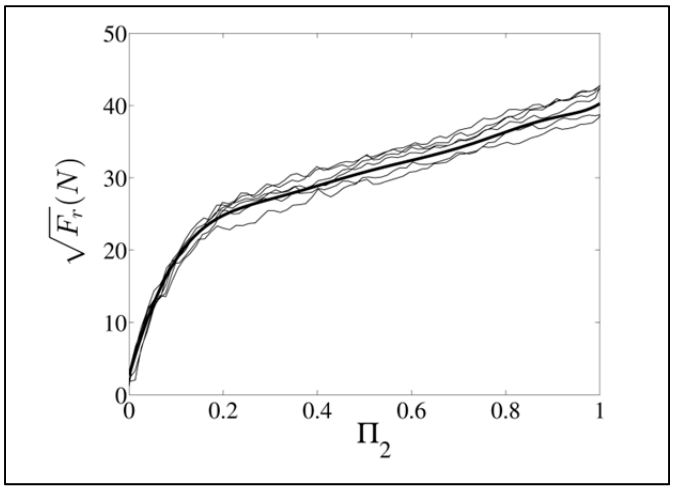

Figure 2.6 F_r predictions and experimental values.
Bold solid line: Model; Solid lines: raw data

2.4.3 Parametric analysis

The following analysis presents a first estimation of the influence on F_r of the parameters listed in section 2.3. The parameters are considered in the following order: Plywood categories, Π_4, nail shank type, and penetration velocity. The coefficient of determination (R^2) and standard error of estimate (*SEE*) of the fitted models vary between 93% and 99%, and 0.0154 and 0.0034, respectively. The following analysis considers only the smooth shank type, with Π_4=0.0052 and one penetration velocity of 8.33x10^{-3} m/s.

2.4.3.1 Plywood categories

Figure 2.7 compares F_r evaluations for the three categories: (1) *CSP*, (2) *DFP*, and (3) *PP*. The graph of Figure 2.7(a) shows the $\sqrt{F_r}$ evaluations. The curves reveal the influence of

the plywood categories; *DFP* presents the highest values, while *CSP* shows the lowest evaluations, and *PP* leads to force amplitudes in between the two other categories. On the other hand, Figure 2.7(b) presents the $\sqrt{\Pi_1}$ values. Table 2-2 indicates that the hardness increases in the following order: *CSP*, *PP* and *DFP*. Therefore, since Π_1 implies a division of F_r by H_M, this second group of results illustrates the influence of H_M; F_r appears to be practically proportional to the hardness. Moreover since the presented force responses include both the deformation-fracture and Coulomb friction, it may be considered that both resistance sources exhibit a practically linear relationship with H_M. While the connection between H_M and the deformation-fracture resistance controlling F_r in the $\Pi_2 < 0.1$ region may be perceived as a matter of course, given that the hardness evaluates the wood capacity to resist indentation, the dependence of the friction force on H_M remains questionable.

In reality, the friction resistance is related to the modulus of elasticity. However, since a portion of the deformation generated during a hardness test is elastic, the hardness evaluation is not completely independent of the Young modulus. This apparent dependence relationship is more visible with soft materials. The plywood types examined in the present research are all made of softwoods. Figure 2.8 draws the hardness of various wood species as a function of the modulus of elasticity. The curves demonstrate that for softwoods, the two properties tend to increase together, thus explaining the observed correlation between the friction force and the hardness. This observation validates the normalization of F_r by H_M in Π_1 at the same time.

clicours.com

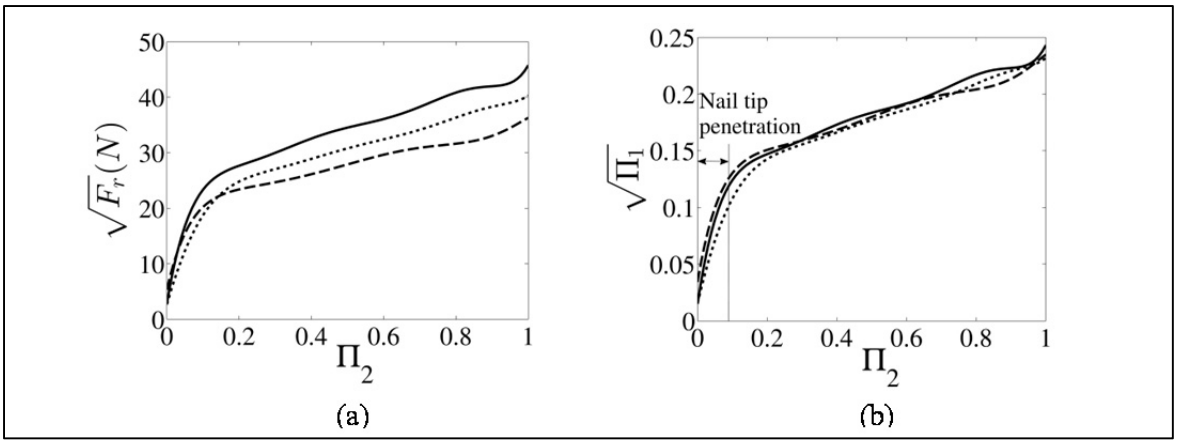

Figure 2.7 Influence of wood properties on F_r: (a) $\sqrt{F_r}$ versus Π_2, (b) $\sqrt{\Pi_1}$ versus Π_2. Solid line: *DFP*; Dotted line: *PP*; Dashed line: *CSP*

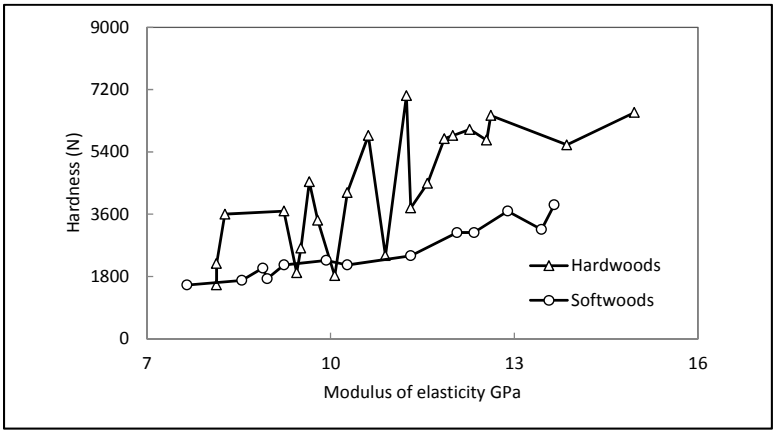

Figure 2.8 Wood hardness vs modulus of elasticity
(taken from Wilcox et al. (1991))

In order to better isolate the influence of the other parameters, the graphs of the following sections only include Π_1.

2.4.3.2 Nail size (Π_4)

Figure 2.9 (a) and (b) present the Π_1 results obtained for smooth nails. Figure 2.9(a) includes four Π_4 values: 0.0412, 0.0500, 0.0520 and 0.0733 for the *DFP* category. Figure 2.9(b) shows the values obtained for the *CSP* category and Π_4 values: 0.0412, 0.0520 and

0.0640. The penetration velocity was $v = 8.33\text{x}10^{-3}$ m/s. Overall, the curves show that enlarging the nail size increases Π_1 .

The F_r response measured for the smooth shank is dominated by adhesion friction forces. Therefore, increasing the nail diameter or length produces a commensurate wood-nail interface augmentation (πDNL), causing proportional effects on F_r. The results in Figure 2.9 display this relationship. Conversely, for the annularly threaded type, the deformation-fracture component corresponds to a significant part of the penetration force over the complete nail penetration. The nail diameter should therefore produce a stronger impact on F_r than the nail length.

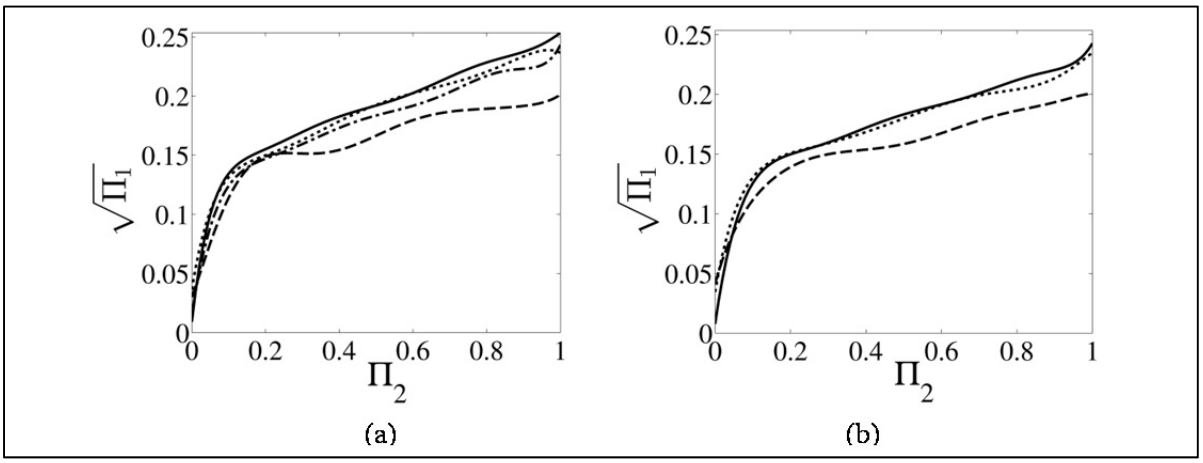

Figure 2.9 Influence of the nail size on $\sqrt{\Pi_1}$ for smooth nails (a) –plywood type *DFP*: Solid line: $\Pi_4 = 0.0462$; Dotted line: $\Pi_4 = 0.0500$; Dash dotted line: $\Pi_4 = 0.0520$; Dashed line: $\Pi_4 = 0.0733$ and (b) -plywood type *CSP*: Solid line: $\Pi_4 = 0.0462$; Dotted line: $\Pi_4 = 0.0520$; Dashed line: $\Pi_4 = 0.0640$

2.4.3.3 Nail shank type

The previous section compared the nail size influence for the different shank types separately. The graph presented in Figure 2.10 juxtaposes Π_1 values evaluated for the three shank types, when the nail penny size is 10d ($\Pi_4 = 0.0500$ for the smooth and annularly threaded nails and $\Pi_4 = 0.0467$ for the helically threaded nails), the penetration velocity is $v = 8.33\text{x}10^{-3}$ m/s, and the plywood category is *PP*. A rapid observation of the chart

indicates that after complete penetration, the nail types generating greater adhesive friction forces lead to higher penetration resistance. The curves also reveal that even with a smaller diameter, helically threaded nails generate penetration forces similar to smooth nails; the helical form leads to larger wood-nail contact interfaces and most likely to greater resulting adhesive forces.

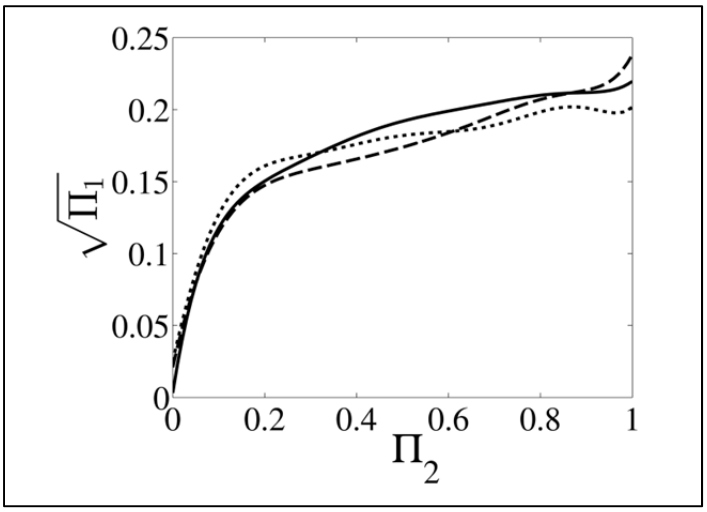

Figure 2.10 Influence of the nail geometry on $\sqrt{\Pi_1}$: Solid line: helically threaded; Dotted line: annularly threaded; Dashed line: smooth

2.4.3.4 Velocity

The following figure presents the penetration resistance measured for the smooth shank type $\Pi_4 = 0.0462$, driven into *PP* plywood at the velocity levels indicated in Table 2-5. Since the penetration resistance is dominated by adhesion, a reduction of the penetration force with a penetration velocity increase was initially expected. However, the curves of Figure 2.11 reveal that for quasi-static conditions, small velocity fluctuations have no significant consequence. This observation is also valid for helically threaded nails, and since the deformation-fracture component is not affected by the driving velocity, may be extended to annularly threaded nails.

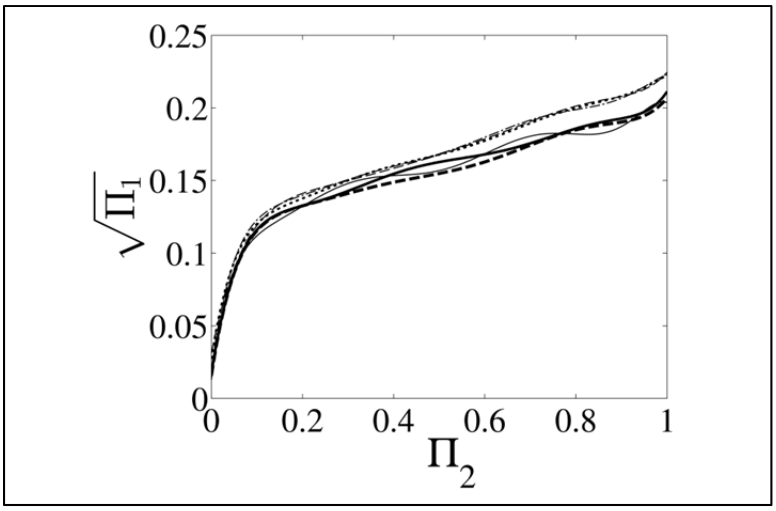

Figure 2.11 Influence of the penetration velocity on $\sqrt{\Pi_1}$. Solid line: 0.000333 m/s; 0.00667 m/s; Dashed line: 0.00833 m/s; Bold dashed line: 0.000833 m/s; Bold solid line: 0.00167 m/s; Dash dotted line: 0.00333; Dotted line: 0.00667 m/s; Dashed line: 0.00833 m/s

2.5 Nail penetration prediction model

The nail penetration resistance formula results from nonlinear regressions fitted to the data sets. Since the composition of F_r depends on the nail shank type, and no parameter precisely describes this influence, it seems more appropriate to prepare a formula variant for each geometry separately. On the other hand, the curve similarity revealed in Figure 2.10 suggests that one single general formula might be sufficient to describe all shank types.

Eq. (2.2) formulates the nail penetration resistance. Table 2-6 gives the coefficient values established for the individual shank types as well as for the general model merging the three data sets. These factors were derived from the measurements carried out for all Π_4 values, penetration velocities and plywood categories. Table 2-7 presents the statistical measures of the model average performances. In addition to R^2 and *SEE*, Table 2-7 includes the mean absolute error (*MAE*).

$$\sqrt{\Pi_1} = C_0 + C_1\Pi_2 + C_2(\Pi_2)^2 + C_3(\Pi_2)^3 + C_4(\Pi_2)^4 + C_5(\Pi_2)^5 + C_6(\Pi_2)^6 + C_7(\Pi_2)^7 + C_8\Pi_3 + C_9\Pi_4 \quad (2.2)$$

Table 2-6 Eq. (2.2) Coefficients

Coefficients	Individual nail shank type model			General model
	Smooth	Annularly threaded	Helically threaded	
C_0	0.029	0.040	0.078	0.014
C_1	1.818	2.008	1.953	1.924
C_2	-12.253	-11.942	-12.262	- 12.171
C_3	46.080	40.305	42.953	43.241
C_4	-98.877	-79.911	-83.472	- 87.738
C_5	121.013	92.291	90.517	101.653
C_6	-78.382	-57.107	-51.420	-62.521
C_7	20.800	14.556	11.939	15.813
C_8	3.910×10^6	-1.3378×10^6	-2.795×10^5	5.547×10^5
C_9	-0.332	-0.351	-1.198	0.067

Table 2-7 Statistical measures of model average performances

Descriptors	Individual nail shank type model			General model
	Smooth	Annularly threaded	Helically threaded	
R^2	94.88%	90.74%	94.10%	85.76%
SEE	0.00899	0.01255	0.01097	0.01628
MAE	0.00675	0.00975	0.00841	0.01334

Table 2-7 shows that, despite a slight fit quality decrease compared to the individual formulas, the general model still explain more than 85% of the variance of Π_1. Therefore, it may be concluded that the global approach represents a valuable option. On the other hand, this general model still involve ten terms. In order to further reduce the model complexity, Table 2-8 and Table 2-9 illustrate the contribution of the Π parameters in the formula. The analysis involves six reduced general models obtained after elimination of successive terms

starting from the end. Table 2-8 presents the model coefficients, while Table 2-9 displays the associated performance measures.

Table 2-8 Coefficients of the reduced models

Coefficients	**Reduced model no.**					
	1	**2**	**3**	**4**	**5**	**6**
C_0	0.018	0.019	0.023	0.030	0.043	0.062
C_1	1.924	1.920	1.670	1.358	0.939	0.559
C_2	- 12.164	- 12.139	- 8.679	- 5.516	- 2.552	- 0.834
C_3	43.219	43.154	23.753	11.034	3.112	0.442
C_4	- 87.706	- 87.666	- 34.117	- 10.237	- 1.332	-
C_5	101.641	101.738	24.553	3.554	-	-
C_6	-62.533	-62.698	-6.986	-	-	-
C_7	15.822	15.893	-	-	-	-
C_8	5.813×10^5	-	-	-	-	-
C_9	-	-	-	-	-	-

Table 2-9 Statistical measures of the reduced models

Descriptors	**Reduced model no.**					
	1	**2**	**3**	**4**	**5**	**6**
R^2	85.75%	85.65%	85.56%	85.30%	84.25%	81.95%
SEE	0.01629	0.01634	0.01639	0.01654	0.01712	0.01832
MAE	0.01336	0.01332	0.01338	0.01349	0.01392	0.01494

Table 2-9 shows that the six reduced general models offer a suitable evaluation of Π_1. The performance descriptors also indicate that up to no 5, the model response remains nearly stable, while model no 6 demonstrates an evident quality diminution. Reduced model no 5

appears therefore as the optimal trade-off. The descriptors of Table 2-9 also reveal that Π_3 and Π_4 have a negligible influence on the quasi-static penetration resistance.

In order to illustrates the model quality, additional tests were carried out with the *PP* category at a penetration velocity of $8.33\text{x}10^{-3}\,\text{m/s}$ for annularly (Case a) and helically (Case b) threaded nail sizes not included in the model preparation: Case a: nail penny size 6d, D=3.048mm and $\Pi_4 = 0.0600$; Case b: nail penny size 12d, D=3.556mm and $\Pi_4 = 0.0431$. The individual nail shank model predictions, as well as the evaluations obtained from the general model and from the reduced models no 5 and 6 were then compared to the measurements. Table 2-10 presents the resulting statistical measures of the model prediction quality.

Table 2-10 Statistical measures of the reduced models

Descriptors	**Individual model**		**General model**		**Reduced model no.5**		**Reduced model no.6**	
	Case a	**Case b**	**Case a**	**Case b**	**Case a**	**Case b**	**Case a**	**Case b**
SEE	0.0133	0.0113	0.0143	0.0132	0.0124	0.0148	0.0152	0.0161
MAE	0.0097	0.0086	0.0112	0.0110	0.0095	0.0110	0.0106	0.0124
MAPE	10.5%	8.9%	13.0%	9.1%	16.7%	10.6%	21.7%	13.6%
Precision	89.5%	91.1%	87.0%	90.9%	83.4%	89.4%	78.3%	86.4%

For the tested conditions, the *MAPE* measures correspond to an individual nail shank model precision of 89.54% and 91.08% for Case a and Case b, respectively. On the other hand, for Case a the general model offers a precision of 87.03%, the reduced model no 5 offers 83.35%, and the reduced model no 6 presents a precision of 78.29%. For Case b, the obtained precision is 90.93% with the general model, while the reduced model no 5 and 6 maintain a precision of 89.43 % and 86.39%, respectively. These results reinforce the conclusions drawn previously from Table 2-9. Also, in order to better illustrate the model responses, Figure 2.12 (a) and Figure 2.12 (b) juxtapose the model estimates and experimental values for Cases a and b, respectively.

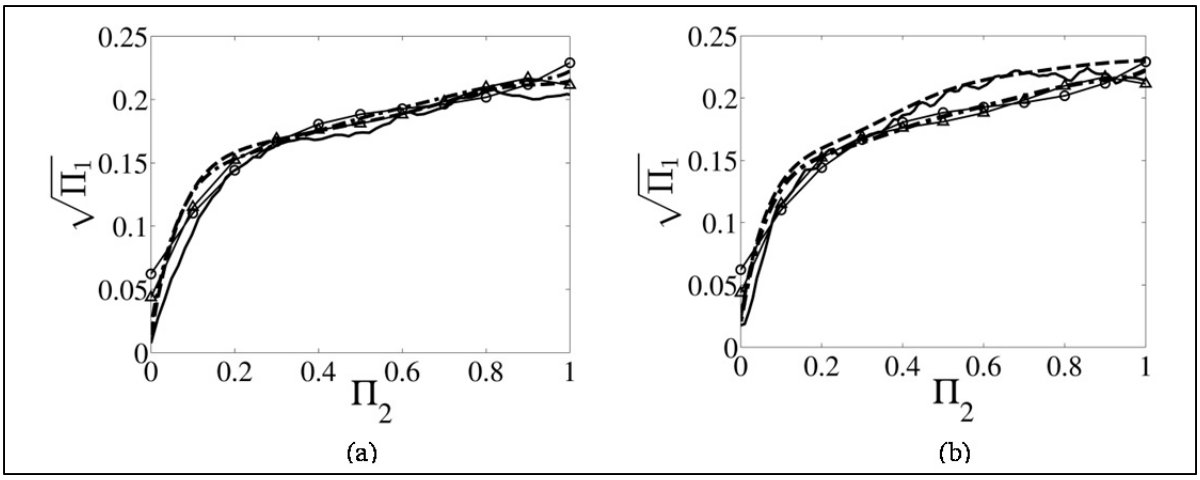

Figure 2.12 Comparison of Eq. (2.2) predictions to experimental values. Dashed line: predicted data by individual nail shank models, solid line: measured data, dashed-dot line: predicted data by the general model, solid line with empty triangles: predicted data by the reduced model no.5, solid line with empty circles: predicted data by the reduced model no.6

2.6 Conclusion

This paper investigated the tribo-dynamic interactions appearing at the wood-nail interface during fastening, and developed a prediction model of the nail penetration resistance force when driven into plywood at quasi-static velocities. The analysis first reduced the studied factors to four dimensionless parameters, $\Pi_{1 \text{ to } 4}$.

The analysis considered that the nail penetration resistance is mainly composed of a wood deformation-fracture force acting in parallel with a friction force component. The measures showed that depending on the shank geometry, one of these components dominates the response. For instance, the annularly threaded shank type generates a penetration resistance largely dictated by the deformation-fracture component, while the smooth shank type, and by extension, the helically threaded geometry, lead to penetration resistance controlled by the friction. Therefore, given that the wood-nail interface temperature possibly affects the adhesion phenomenon determining the friction force component, and that the interface temperature depends on the speed, the investigation examined the penetration rate influence. The experimental results demonstrated that, for a quasi-static speed range, penetration velocity variations result in inconsequential effects, and could be neglected.

The analysis also evaluated the wood hardness role, and showed that for softwoods, both wood deformation-fracture and friction force components appear to vary in concert with the hardness modulus. Therefore, the global penetration resistance could be considered as largely determined by the wood hardness. However, since the Young modulus-hardness apparent relationship remains indistinct for hardwoods, this assertion only remains acceptable for softwoods and softwood-based products.

The last section of the paper derived a penetration resistance prediction model from the experimental data. The examination results demonstrated that the resistance force components vary with the nail shank type. Therefore, in addition to a general representation, the model also provides a particular variant for each shank geometry. While the general model and its reduced version model no 5 offer rapid and sound evaluations for any nail types, the individual nail shank models assure higher precision levels. The study compared the model-predicted forces to measurements completed for nail geometries not considered during the model preparation, and showed agreement levels higher than 89%, 87% and 83% for the individual nail shank model, the general model and the reduced model no 5, respectively. Therefore, considering the extensive experimental campaign and these exploratory verification tests, the developed penetration force predictor is deemed to offer reliable evaluations. Future works should examine the high velocity range and extend the prediction model.

2.7 Acknowledgments

The support of NSERC (Natural Sciences and Engineering Research Council of Canada) is gratefully acknowledged.

CHAPTER 3

DESIGN AND FABRICATION OF A TEST MACHINE FOR HIGH-VELOCITY NAIL DRIVING EXPERIMENTS

This chapter designs and fabricates an advanced test machine to carry out the high-velocity nail driving tests. This test machine includes a pneumatic accelerator and various measurement devices. Using this machine, the measurements can be conducted over various penetration speeds, impactor masses, nail geometries and sizes, and wood types.

The following presents details of the machine design requirements, the machine design, and the experimental procedure for future tests.

3.1.1 Design requirements

The machine should be designed such that:

(1) a wide range of penetration velocities (including the penetration velocity in the nail gun process) are covered in the tests;
(2) the nail driving tests are conducted using a range of projectile (impactor) masses, with the smallest mass equal to the nail gun piston-rod assembly mass;
(3) the nail driving tests are conducted at least with the same average energy of the nail penetration in the nail gun process (using different projectile masses), as well as, the lower energy levels;
(4) the machine operation is safe as the projectile speed is very high;
(5) the damage to the machine and workpiece is prevented by controlling the speed of the projectile at the end of nail penetration process.

3.1.2 Machine design

To fulfill the velocity coverage requirement (requirement 1), free fall acceleration of the projectile was not sufficient due to the laboratory height limitation. A rapid acceleration

of the projectile was required to generate high penetration speeds. After evaluating different design options, the study found an optimal design including a pneumatic accelerator to produce the required acceleration. Another challenge was to maintain the lowest projectile mass equal to the nail gun piston-rod assembly mass (requirement 2). The following presents the implemented solution while describing the designed machine operation. Through meeting requirements 1 and 2, requirement 3 will be automatically covered.

Figure 3.1 shows the designed and fabricated test machine. The machine consists of a compressed air reservoir with the capacity of 1.38 MPa, a projectile, a carrier, three valves, four elastomeric bumpers, and two pneumatic cylinders. To ensure safety of the operator, a frame made of steel and Plexiglas attached to the floor supports the machine. Opening the frame door cuts off the electricity and stops the machine from working.

Before each test, the primary piston-rod assembly (3) is raised to its highest level inside the primary pneumatic cylinder (2) and it is locked at this position by a locking rod system (5) manually.

Pressing the trigger switch (5), allows the air flow to the trigger pneumatic cylinder (5) through a directional control valve. The air pressure pushes back the locking rod. A reed switch sensor detects the locking rod when it reaches its rear position and sends an activation signal to the gas shutoff valve (8). This valve opens the poppet valve (9) allowing the compressed air inside the reservoir (1) to flow to the primary pneumatic cylinder above the piston. The air pressure pushes the primary piston-rod assembly along with its attached mechanical carrier (4) and projectile (11) downward (Figure 3.1). The projectile is incorporated into the carrier. Free fall of the projectile is used to drive the nail into the wood (7). There are two reasons for not using the primary piston-rod assembly as the projectile: 1- to eliminate the air pressure factor during the penetration, 2- to maintain the lowest projectile mass equal to the nail gun piston-rod assembly mass (0.131 kg) which was otherwise hard to achieve due to the additional length (and so the mass) needed for the primary piston-rod assembly. At the end of the nail penetration, the carrier collision with the wood might damage the machine and wood severely. To avoid this damage (requirement 5), four elastomeric bumpers (6) are used to absorb the energy of the carrier and prevent it from

impacting the wood. The bumpers stop the carrier but the projectile continues to move downward as long as its energy lasts.

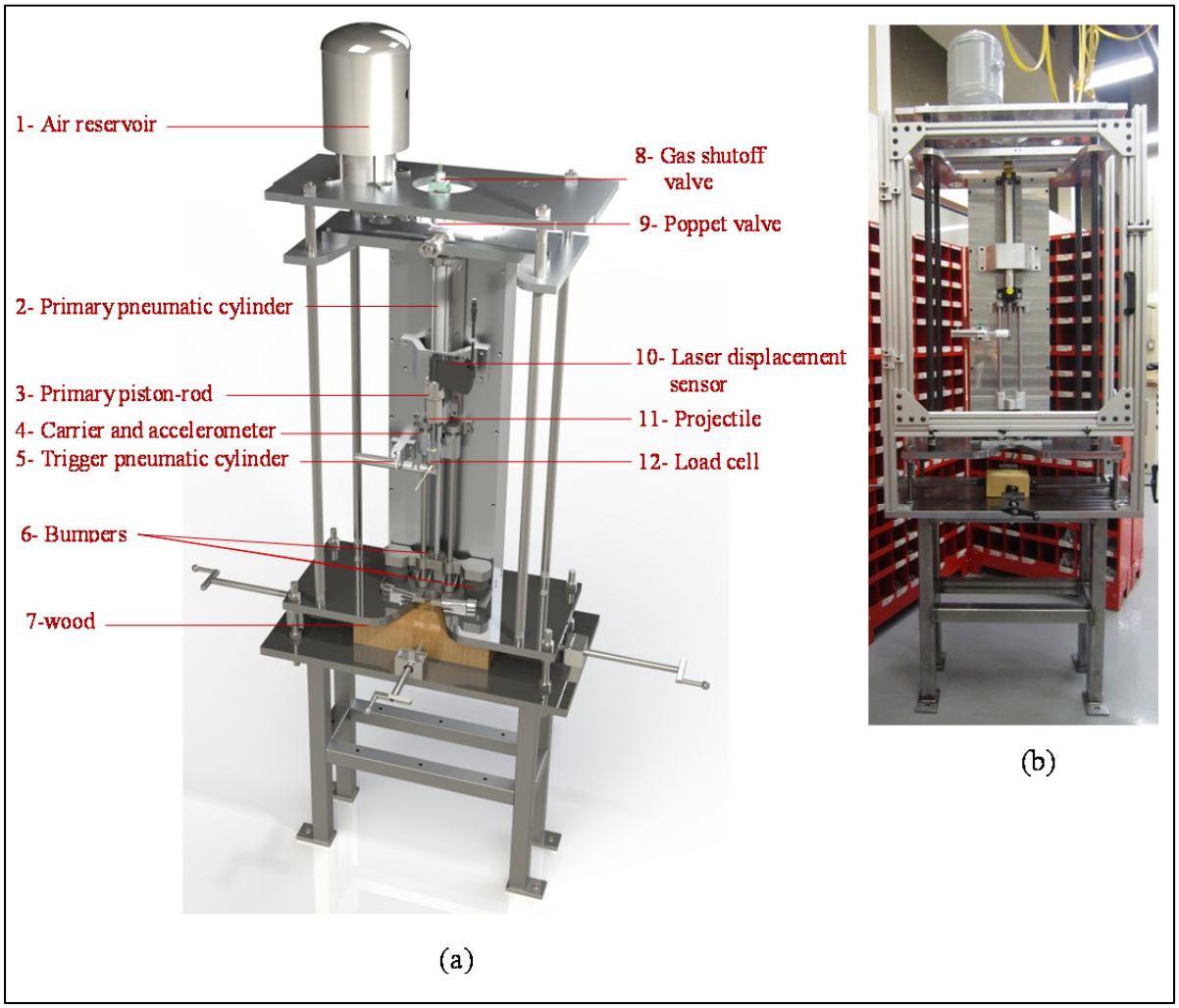

Figure 3.1 Test machine: (a) CAD, (b) fabricated

The velocity of the projectile during penetration is adjusted by changing the reservoir air pressure. The penetration energy can be regulated through varying the projectile mass and/or the penetration velocity.

Various measurement devices are incorporated to the machine to record the required variables for developing the nail penetration model. A high speed laser displacement sensor (10) measures the displacement of the projectile. An accelerometer (4) measures the

acceleration of the mechanical carrier. A load cell (12) is installed on the projectile end to measure the penetration force. A high speed camera (not shown in Figure 3.1) is also integrated into the setup to capture the process motion (10,000 frames/sec).

3.1.3 Experimental procedure

3.1.3.1 Influential parameters and dimensional analysis

Initial qualitative evaluation indicated that the parameters controlling PRF may be collected in two classes mainly: 1) the size and material properties (parameter set 1), and 2) the penetration process (parameter set 2).

Parameter set 1 includes: 1- the wood density, 2- the wood hardness modulus, 3- the nail geometry type or the nail shank type, 4- the nail diameter, and 5- the nail length.

Parameter set 2 includes the following three factors: 6- the penetration velocity, 7- the displacement, 8- the impact velocity between nail and impactor, 9- the projectile mass.

Table 3-1 shows the identified parameters and the corresponding dimensions. *L*, *M* and *T* indicate the length, mass and time units, respectively. A dimensional analysis based on Buckingham's π-theorem (Szirtes, 2007) leads to a parameter number reduction. Dimensionless parameters also generalize the validity range of the results. Since the nail shank type cannot be associated with any dimension, it is excluded from the dimensional analysis. *PRF* corresponds to the dependent parameter, while H_M, *NL* and *v* represent the base parameters. In the following, the variable F_r replaces PRF.

Mathematical manipulations not included here yield the following four *Π* terms (or dimensionless parameters). Combined with *ST,* they describe the investigated space:

$$\Pi_1 = \frac{F_r}{H_M NL}, \quad \Pi_2 = \frac{y}{NL}, \quad \Pi_3 = \frac{NL\rho v_0^{\,2}}{H_M}, \quad \Pi_4 = \frac{v}{v_0}, \tag{3.1}$$
$$\Pi_5 = \frac{D}{NL}, \quad \Pi_6 = \frac{Mv_0^{\,2}}{H_M NL^2}$$

Table 3-1 Parameter sets 1 & 2

	Parameters	**Dimension**
Parameter set 1	1- wood density(ρ)	ML^{-3}
	2- wood hardness(H_M)	MT^{-2}
	3- nail shank type (*ST*)	-
	4- nail diameter (*D*)	L
	5- nail length(*NL*)	L
Parameter set 2	6- penetration velocity (v)	LT^{-1}
	7- displacement (y)	L
	8- impact velocity(v_0)	LT^{-1}
	9- projectile mass(M)	M

3.1.3.2 Projectile mass and velocity

Table 3-2 shows a list of the projectile masses and average penetration velocities included in the study for 12d nail penny size. Five projectile masses are considered. The smallest mass is chosen close to 0.131 kg; the piston-rod assembly mass in Bostitch N80 CB-Coil framing nailer. The same projectile masses will be tested for other nail sizes. Each mass is examined for three velocity levels. The middle velocity level is chosen to provide average penetration energy equal to that of Bostitch N80 CB-Coil framing nailer. The upper and lower velocity levels are $\pm$5 m/s of the middle value. The reason for choosing three velocity levels for each mass is to cover a wide range of velocities as the velocity might have a strong influence on PRF. The penetration energy required for full penetration of the nail varies with

the nail size. Therefore, the tested velocity levels vary based on the nail size. The approach introduced in Table 3-2 is used to define the velocity levels for other nail sizes.

Table 3-2 Projectile masses and velocities for 12d nail size

Projectile mass (Kg)	**Average penetration velocity (m/s)**	**Average penetration energy(J)**
0.1293	20.36	27.15
	25.36	42.12
	30.36	60.37
0.2	15.52	24.10
	20.52	42.12
	25.52	65.15
0.3	11.76	20.74
	16.76	42.12
	21.76	71.01
0.4	9.51	18.10
	14.51	42.12
	19.51	76.15
0.5	7.98	15.92
	12.98	42.12
	17.98	80.83

3.1.4 Conclusion

The test machine fabricated in this work can be used in the future to develop a high-velocity PRF law which fully covers the entire parameter space of the nail penetration in the pneumatic nail gun process. Incorporating this law in the dynamic model (chapter 4) will improve the model accuracy.

CHAPTER 4

ARTICLE 3: NONLINEAR DYNAMIC MODELING OF PNEUMATIC NAILING DEVICES

Z. Nili Ahmadabadi[a], Raynald Guilbault[a], Frédéric Laville[a]

[a] Université du Québec, École de technologie supérieure, Department of Mechanical Engineering, 1100 Notre-Dame Street West, Montreal, Quebec, Canada H3C 1K3

This article has been submitted to the Journal of Dynamic Systems, Measurement, and Control in June, 2016

4.1 Abstract

This paper develops a mathematical modeling procedure for pneumatic nailing devices. The representation integrates all the device operation phases composing the nailing process. The model accounts for the dynamics of the chamber pressures, the moving parts, the nonlinear interactions and impacts between the fixed and moving components, and includes the nailing device body and workpiece. All the system parameters integrated into the proposed model were established from experimental measurements. This model also integrates a nonlinear empirical formulation to predict the nail penetration resistance force. The final representation is validated through a comparison of the predicted piston motion and air pressures to experimental measurements made on a specific nailing device. Averaging the measured to simulated air pressure ratios established at important time positions shows an agreement level higher than 93%.

Keywords: nailing device dynamics; pneumatic; wood-nail tribo-dynamics

4.2 Introduction

The present study belongs to a broader three-step research project aiming at finding means to reduce noise emissions in pneumatic nailing devices. During the first step, the noise sources were identified and ranked (Ahmadabadi et al., 2015a; 2016; Ahmadabadi et al.,

2015c). During the second step, which is presented in this paper, a nonlinear dynamic model covering the complete nailing process is developed. During the third step, the force and exhaust flow outputs of this dynamic model will then be used as inputs to a vibro-acoustic/air flow-acoustics model of the system that will predict the noise emissions. Also, with the dynamic model alone and due to the linearity between acceleration and noise, design modifications can be proposed to change the noise emission by changing the structural excitation forces and exhaust flow.

The main objective of the dynamic model development presented in this paper is to set up a simulation tool able to describe the influence of design modifications on the dynamic response of nailing devices. Most of the operation phases involved in the nailing process may be described through mathematical relations. In fact, only the penetration resistance forces resulting from the tribo-dynamic interactions taking place at the wood-nail interface required particular experimental investigations that resulted in establishing a nonlinear empirical prediction law for the penetration resistance (Ahmadabadi et al., 2015b).

Despite numerous publications on pneumatic systems modeling (Bharath et al., 1990; Lu et al., 2011; Ma et al., 2010; Miller et al., 2014; Nieto et al., 2008; Porumamilla et al., 2008; Pu et al., 2011; Sorli et al., 2004; Subramanian et al., 2004), only two studies considered the mathematical modeling of pneumatic nailing devices. For instance, Zhong et al. (2008) presented a simplified model of a nailer. The authors simulated the air pressure in three sections of the nailer chambers and considered the piston as acting against a constant penetration resistance force. Later, Hu (2009) examined the gas dynamics influence on the performance of a pneumatic nailer. This second reference also neglected the complex tribo-dynamic conditions involved in the nail penetration process, and reduced the nail penetration resistance to a constant force. In reality, the model in both of these studies neglected the influence of the air channel connecting the chambers, the dynamics of the impacts occurring between the different moving and fixed components of the system (impact between piston and bumper or between the workpiece and supports, etc.), the nailing device body and valve dynamics, as well as the workpiece dynamics.

The two previously cited references on nailer dynamic modeling considered the valve as a fixed restriction. However, precise modeling of the outflows through restrictions is essential, since these elements can generate significant mechanical vibrations and noise, more specifically the air exhaust through nailing device flow restrictions was found to be a significant contributor to emitted noises by the present authors (Ahmadabadi et al., 2016) and others (Adelberg et al., 2002; Jayakumar et al., 2015; Tisserand and Triomphe, 2011). During the exhaust phase, the generated aerodynamic noise depends on the outflow restriction level. When the flow is subsonic, turbulent mixing noise becomes the dominant contributor to the acoustic power (Lighthill, 1962; 1963; Ribner, 1964; Witczak, 1976). This noise type results from turbulent mixing of jet flow with the ambient fluid. On the other hand, supersonic conditions are engendered when the flow is choked and the flow velocity at the restriction exit reaches the sound speed. Under such conditions, two additional noise sources appear and predominate over the turbulent mixing noise (Witczak, 1976): broadband shock-associated noise, and screech tones (acoustic feedback). The broadband shock-associated noises result from interactions between downstream propagating large-scale turbulence structures passing through quasi-periodic shock cell structures (Tam, 1995). Screech tones are discrete frequency noises (Crocker, 2007; Tam, 1995; Witczak, 1976). They result from unsteady interactions between large amplitude instability waves and quasi-periodic shock cell structures. Chow and Reethof (1980) demonstrated that choked valve noise mechanisms are affected by the valve configuration, the downstream to upstream pressure ratio, and the valve opening.

The model developed in the present paper accounts for the following elements: 1- the device body; 2- the piston-rod assembly; 3- the valve and the flow through the valve variable restriction; 4- the workpiece; 5- the impacts between the fixed and moving components (internal and external components); 6- the chamber pressures; 7- the time delay and flow amplitude attenuation generated by connecting air channel.

Also, since Ahmadabadi et al. (2016) demonstrated that the dynamic interactions between the nail and the wood element play a significant role in the generated noise and vibration, the model integrates a nonlinear empirical formulation to predict the nail

penetration resistance force in solid woods (F_r). This formulation was developed following the approach introduced in Ahmadabadi et al. (2015b).

The final representation is validated through a comparison of the predicted piston motion and air pressures to experimental measurements made on a specific nailing device. The following system parameters were established from experimental measurements and integrated into the proposed model: the friction between moving surfaces; the stiffness and damping properties of the internal parts; and the spring stiffness.

Section 4.3 describes nailing device operation. Section 4.4 presents the structural dynamic model. In the structural dynamic model, the activation forces result from the air pressure acting in the different chambers, therefore section 4.5 develops the gas dynamic model. Section 4.6 describes the experimental procedures for system parameters measurement. Section 4.7 presents the details of the model numerical resolution. Finally, section 4.8 presents the experimental validation of the model.

4.3 Nailing device operation

Figure 4.1 offers a schematic representation of pneumatic nailing devices, and indicates the common components of a pneumatic device system. Figure 4.2 illustrates the successive phases involved in nailing operation. Finally, Table 4-1 groups the important time positions identified in the following description.

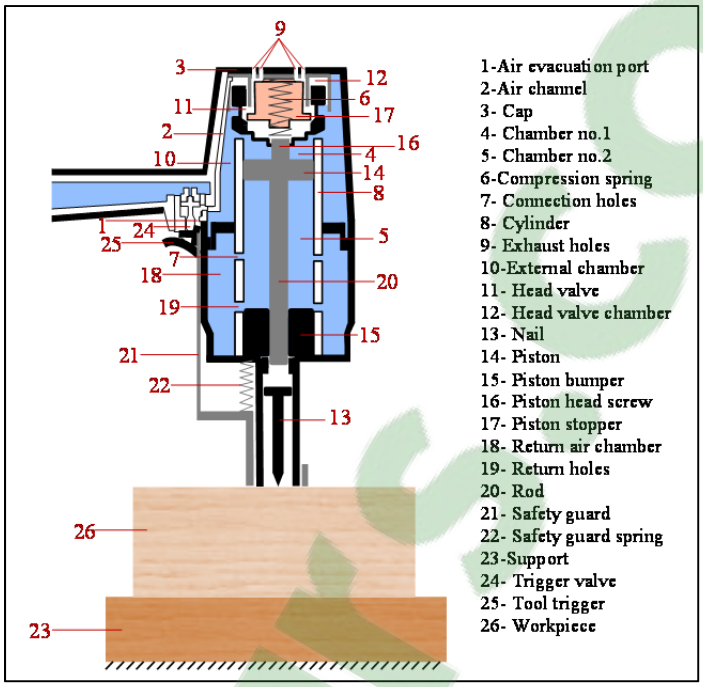

Figure 4.1 Common pneumatic nailing device components

Before t_0, or when the trigger valve is in the released position, the compressed air flows to the head valve chamber (12) through the air channel (2). The resultant of the air pressure force on both sides of the head valve combined with the compression spring (6) downward force keeps the head valve pressed against the cylinder top (8). Pulling the device trigger (and actuating the trigger valve) at t_0 closes the trigger valve and stops the air flow to the head valve chamber. The remaining compressed air in this area flows out to the atmosphere through the air channel (2). The head valve starts moving up and opens at t_1, when the resultant force is in the upward direction. At t_2 the expulsion to the atmosphere of the compressed air above the head valve is completed. The head valve upward displacement closes the air exhaust. The compressed air starts flowing to the area above the piston head (chamber no.1 (4)) at t_3.

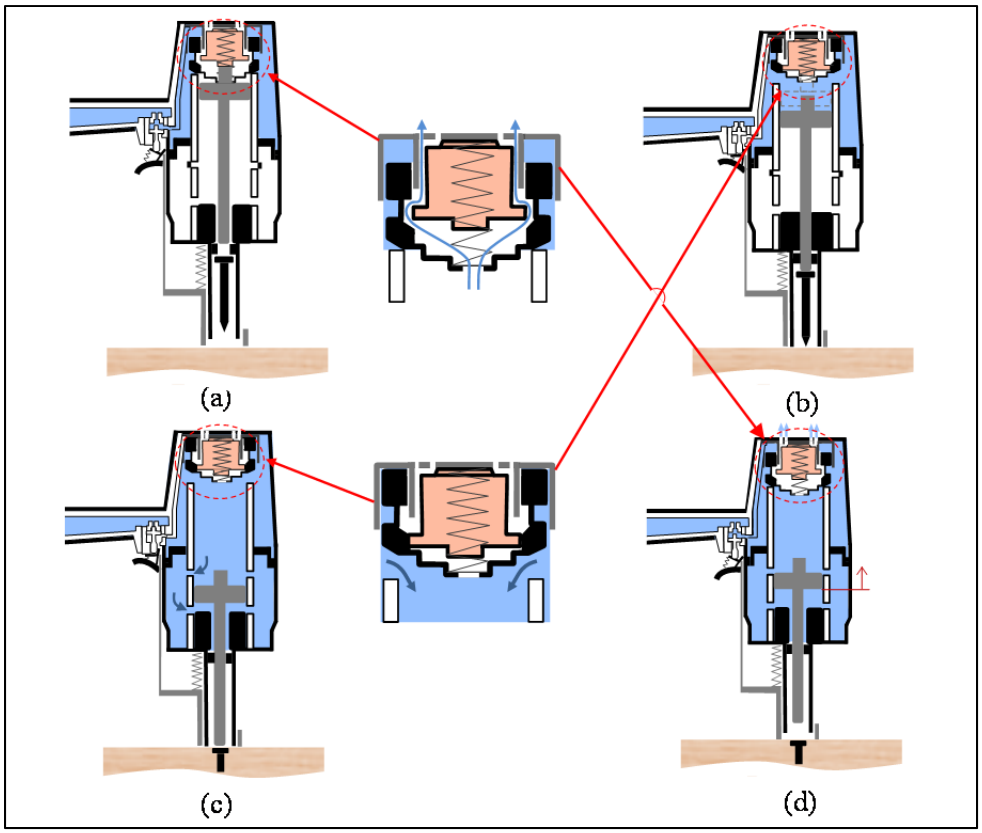

Figure 4.2 Schematic representation of pneumatic nailing device operation: (a) device at rest, (b) nail driving stroke, (c) end of stroke, (d) air exhaust

The air pressure pushes the piston which starts its downward movement at t_4. At t_5, after a displacement of y_{pbin}, the rod impacts the nail. The nail penetration into the wood starts at t_6 after a piston displacement of y_{pbp}. The rod is then subject to the nail penetration resistance force (F_r). This penetration force is composed of the nail-wood friction and the fracture/deformation of the workpiece.

Table 4-1 Description of events occurring during pneumatic nailing device operation

Point no.	**Event description**
t_0	Trigger valve actuated
t_1	Start of head valve opening

Table 4-1 (Continued)

Point no.	Event description
t_2	Complete evacuation of air above head valve
t_3	Start of compressed air flow to chamber no.1
t_4	Start of piston downward movement
t_5	Impact between rod and nail
t_6	Start of nail penetration into workpiece
t_7	Start of pressure measurement in chamber no.1
t_8	Start of air flow from chamber no.1 to return chamber
t_9	End of nail penetration
t_{10}	Impact between the piston and bumper
t_{11}	End of piston oscillations
t_{12}	Complete release of the trigger valve
t_{13}	Start of the air exhaust
t_{14}	Start of the piston return to its upper position
t_{15}	End of chamber no. 1 pressure measurement
t_{16}	End of piston upward stroke
t_{17}	End of air exhaust process
t_{18}	End of piston oscillations

At t_7, after a traveling distance of y_{pt}, the piston crosses the pressure transducer incorporated into the cylinder to measure the chamber no.1 pressure. As the piston head traverses at t_8 the connection holes (7) situated at the distance of y_{hr}, the air inside chamber no.1 starts flowing to the return air chamber (18). The return air chamber is connected to chamber no.2 (5) through return holes (19); therefore, the compressed air inside the return air chamber easily flows to chamber no.2. The nail penetration ends at t_9 when the piston stops.

The end of the nail penetration is associated with an important augmentation of the force imposed on the nailing device. This force increase results from the nail head/wood

contact, and the wood restitution force. Depending on the supply pressure and nail size, there might be over penetration of the nail and the piston might impact the piston bumper (15). Under this condition, the elastic restitution force from the bumper further increase the upward force on the piston. The resultant upward force pushes the nailing device upward. As a result, the safety guard starts to go back to its release position.

The head valve can be liberated by releasing either the device trigger or the safety guard. According to high speed videos recorded during experimental evaluations, under normal conditions the safety guard release occurs sooner than the device trigger disengagement. As the safety guard is releasing, the resultant force acting on the piston becomes positive as a result of higher pressure in chamber no.1. This again gradually changes the piston movement to the downward direction. The piston moves down until it impacts the piston bumper at t_{10} and bounces back. The ensuing piston oscillations end at t_{11}.

At t_{12} the trigger valve is completely released. The head valve then starts closing more rapidly. The air exhaust starts at t_{13} through the exhaust holes (9). The final piston return to the upper position starts at t_{14}. During the experiments, the cylinder chamber pressure transducer measured the air pressure of chamber no.1 until t_{15}, at the position where the piston crosses the transducer. The piston head screw (16) strikes the piston stopper (17) at t_{16}. This impact also causes piston oscillations lasting until t_{18}. The air exhaust phase ends at t_{17}.

4.4 Structural dynamic model

Figure 4.3 shows the dynamic model of the system. Figure 4.3 also defines the global coordinate system (x_{gl},y_{gl}) as well as the local coordinate systems. The following list describes the variables:

Areas:

- A_1 and A_2 are the piston effective areas on the piston head screw and rod side, respectively;
- A_{h1} is the area of the head valve supporting the downward pressure;
- A_{h2} is projection of the head valve area supporting the upward pressure;
- A_r is the rod cross-sectional area.

Forces:

- F_{hm} is the operator hand force;
- F_r is the nail penetration resistance force.

Stiffness:

- k_b and β_b are the piston bumper/piston stopper stiffness and viscous damping coefficient, respectively;
- k_c is the contact stiffness between head valve and cylinder/nailing device cap;
- k_{esg} is the equivalent safety guard stiffness;
- k_s is the compression spring (6) stiffness;
- k_w is the wood stiffness;
- k_{ws} is the wood- support contact stiffness;
- k_{wsn} is the wood-nailing device contact stiffness.

Masses:

- M_g is the nailing device mass;
- M_h is the head valve mass;
- M_n is the nail mass;
- M_p is the piston-rod assembly mass;
- M_w is the wood mass.

Pressures:

- P_1 and P_2 are the absolute pressures in chamber no.1 and 2, respectively;
- P_a is the absolute ambient pressure;
- P_{ext} is the absolute air pressure in the external chamber;
- P_h is the absolute air pressure in the head valve chamber.

Displacements:

- y_h is the head valve displacement;
- y_g is the nailing device displacement;
- y_p is the piston-rod assembly displacement;
- y_w is the wood displacement.

Friction coefficients:

- μ_{fh} is the head valve-cap wall friction coefficient;
- μ_{fp} is the piston-cylinder wall friction coefficient;

- μ_r is the nail-wood friction coefficient.

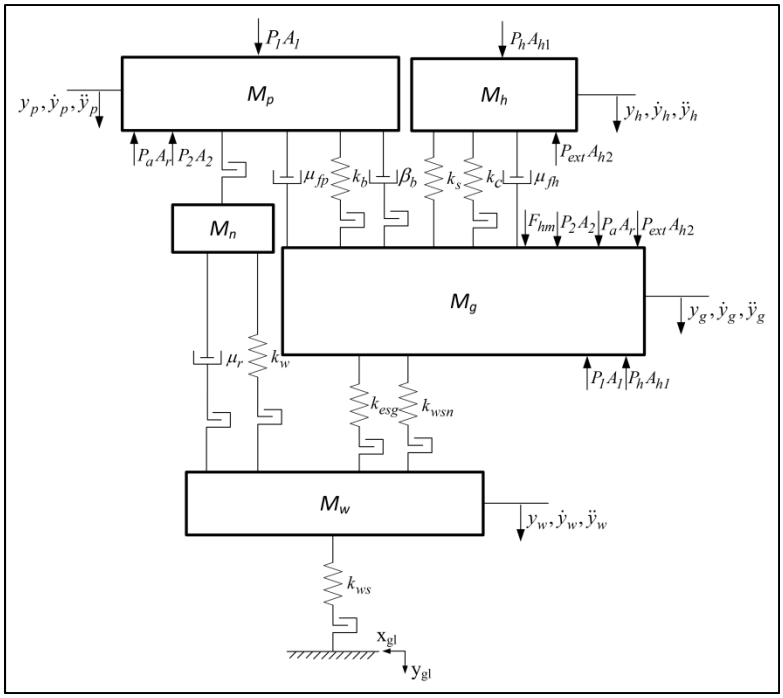

Figure 4.3 Pneumatic nailing device dynamic model.
Nonlinear elements: μ_r, k_w, μ_{fp}, k_b, β_b, k_c, μ_{fh}, k_{esg}, k_{wsn}, k_{ws}, and k_s.

The following subsections (4.4.1 to 4.4.4) present the motion equations written for the masses shown in Figure 4.3, while Section 4.5 develops the pressure modeling procedures.

4.4.1 Piston-rod assembly

Eq.(4.1) is the motion equation of the piston-rod assembly:

$$M_t\ddot{y}_{pr}+\beta_b\dot{y}_{pr} + k_b(y_{pr} + y_b) + k_w(y_p - y_w - l_n - y_{pbp}) + F_{fp} = F_{p0} \qquad (4.1)$$

where y_{pr} (= y_p-y_g) is the piston-rod assembly displacement relative to that of the nailing device, l_n is the nail length, and F_{fp} is the friction force between piston and cylinder wall

(= $\mu_{fp}F$). In the present model the friction force was directly evaluated from experimental measurements (see Section 4.6). M_t, β_b , k_b, y_b, k_w, and F_{p0} are described below,

$$M_t = \begin{cases} M_p + M_n & y_{pr} \geq y_{pbin} \; and \; n_{dc} < 1 \\ M_p & y_{pr} < y_{pbin} \; or \; n_{dc} \geq 1 \end{cases} \tag{4.2}$$

$$\beta_b = \begin{cases} \beta_{pb} & y_{pr} \geq L \\ \beta_{ps} & y_{pr} \leq 0 \\ 0 & 0 < y_{pr} < L \end{cases} \tag{4.3}$$

$$k_b = \begin{cases} k_{pb} & y_{pr} \geq L \\ k_{ps} & y_{pr} \leq 0 \\ 0 & 0 < y_{pr} < L \end{cases} \quad , \quad y_b = \begin{cases} -\mathrm{L} & y_{pr} \geq L \\ & \\ 0 & y_{pr} < L \end{cases} \tag{4.4}$$

$$k_w = \begin{cases} H_{Mw} & (y_p - y_w) > (l_n + y_{pbp}) \; and \; n_{dc} < 1 \\ 0 & (y_p - y_w) \leq (l_n + y_{pbp}) \; or \; n_{dc} \geq 1 \end{cases} \tag{4.5}$$

$$F_{p0} = P_1 A_1 - P_2 A_2 - P_a A_r - c_r F_r + M_t g \tag{4.6}$$

where n_{dc} counts the number of times the piston changes direction, β_{pb} is the damping coefficient of the piston bumper, β_{ps} is the damping coefficient of the piston stopper, k_{pb} is the piston bumper stiffness, k_{ps} is the piston stopper stiffness, L is the piston stroke, H_{Mw} is the wood hardness modulus, y_{pbin} and y_{pbp} are constant distances defined at t_0 between the rod end and the nail head or the workpiece surface, F_{p0} is the force resultant on the piston, g is the gravitational acceleration, and c_r is a parameter representing the nail penetration condition. Eq.(4.7) describes c_r,

$$c_r = \tag{4.7}$$

Clicours.COM

$$\begin{cases} 1 & (y_p - y_w) \geq y_{pbp} \; and \; n_{dc} < 1 \; and \; (y_p - y_w) \leq (l_n + y_{pbp}) \\ 0 & (y_p - y_w) < y_{pbp} \; or \; n_{dc} \geq 1 \; or \; (y_p - y_w) > (l_n + y_{pbp}) \end{cases}$$

4.4.2 Head valve dynamics

The head valve equation of motion is:

$$M_h \ddot{y}_{hr} + k_c(y_{hr} + y_c) + F_{fh} = F_{h0} \tag{4.8}$$

where y_{hr} is the head valve displacement relative to that of the nailing device (= y_h-y_g), F_{fh} is the friction force between head valve and cap wall (= $\mu_{fh}F$). In the present model the friction force was directly evaluated from experimental measurements (see Section 4.6). k_c, y_c , and F_{h0} are given by,

$$k_c = \begin{cases} k_{hc2} & y_{hr} \geq L_h \\ k_{hc1} & y_{hr} \leq 0 \\ 0 & 0 < y_{hr} < L_h \end{cases} \quad , \quad y_c = \begin{cases} -L_h & y_{hr} \geq L_h \\ 0 & y_{hr} < L_h \end{cases} \tag{4.9}$$

$$F_{h0} = P_h A_{h1} - P_{ext} A_{h2} + F_s + M_h g \tag{4.10}$$

where L_h is the maximum head valve displacement, k_{hc1} is the contact stiffness between head valve and the nailing device cap surface, k_{hc2} is the contact stiffness between the head valve and cylinder, F_{h0} is the force resultant acting on head valve, F_s is the compression spring force. Since F_s is non-linear, instead of considering a spring stiffness, the F_s expression was derived from experimental measurements (see Section 4.6) and is directly introduced in the model.

4.4.3 Nailing device body dynamics

The nailing device body equation of motion is written as,

$$M_g\,\ddot{y}_g - \beta_b \dot{y}_{pr} - k_b(y_{pr} + y_b) + c_{wsn}k_{wsn}(y_g - y_w) - k_c(y_{hr} + y_c) - F_{fh} - F_{fp} + k_{esg}(y_g - y_w + y_{msg}) = F_{g0} \tag{4.11}$$

where c_{wsn} is a parameter representing the nail-wood interactions. c_{wsn}, k_{esg}, and F_{g0} are,

$$c_{wsn} = \begin{cases} 1 & y_g > y_w \\ 0 & 0 \end{cases} \tag{4.12}$$

$$k_{esg} = \begin{cases} \frac{k_{sg}k_{wsn}}{k_{sg}+k_{wsn}} & (y_g - y_w) > -y_{msg} \\ 0 & (y_g - y_w) \le -y_{msg} \end{cases}$$

$$F_{g0} = F_{hm} - F_s - P_1A_1 + P_2A_2 + P_aA_r - P_hA_{h1} + P_{ext}A_{h2} + M_g g \tag{4.13}$$

where k_{sg} is the safety guard spring stiffness, and y_{msg} is the maximum compression of safety guard spring. The trigger is released when $y_g = y_w - y_{msg}$.

4.4.4 Workpiece dynamics

The workpiece equation of motion is expressed as,

$$M_w\,\ddot{y}_w + c_{wsn}k_{wsn}(y_w - y_g) + k_w(y_w - y_p + l_n + y_{pbp}) + k_{esg}(y_w - y_g - y_{msg}) + c_{ws}k_{ws}y_w = F_{w0} \tag{4.14}$$

where c_{ws} is a parameter representing the workpiece condition. c_{ws} and F_{w0} are,

$$c_{ws} = \begin{cases} 1 & y_w > 0 \\ 0 & 0 \end{cases} \tag{4.15}$$

$$F_{w0} = c_r F_r + M_w g \tag{4.16}$$

Eqs. 4.1, 4.8, 4.11 and 4.14 describe the motion of the system shown in Figure 4.3. In these equations the activation forces result from the air pressure acting in the different chambers. These pressures depend on the input/output mass flow rates and the piston translational speed. Section 4.5 presents the pressure relations.

4.5 Gas dynamic model

This section presents the mathematical expressions describing the chamber pressures and the input/output mass flow rates. The analysis assumes that: 1 the pressure and temperature within the chambers are homogenous, 2 the gas is ideal, and 3 kinetic and potential energy terms are negligible. Eq.(4.17) shows the ideal gas law:

$$P = \rho R T \tag{4.17}$$

where P is the pressure, ρ is the air density, R is the ideal gas constant and T is the temperature. The input and output mass flow rates ($\dot{m}_{in}$ *and* $\dot{m}_{out}$) can be expressed through the continuity equation, where V is the volume:

$$\dot{m}_{in} - \dot{m}_{out} = \dot{\rho} V + \rho \dot{V} \tag{4.18}$$

The energy equation is given by:

$$q_{in} - q_{out} + \gamma C_v (\dot{m}_{in} T_{in} - \dot{m}_{out} T) - \dot{W} = \dot{U} \tag{4.19}$$

where q_{in} and q_{out} are the heat transfer terms, γ is the specific heat ratio ($\gamma = 1.4$ for air), C_v (=R/(γ-1)) is the specific heat at constant volume, T_{in} is the input gas temperature, while $\dot{W}$ and $\dot{U}$ are the work change rate and the change rate of the internal energy given by Eqs.(4.20) and (4.21), respectively.

$$\dot{W} = P\dot{V} \tag{4.20}$$

$$\dot{U} = \frac{d}{dt}(C_v mT) = \frac{1}{\gamma-1}(V\dot{P} + P\dot{V}) \tag{4.21}$$

Substituting $\dot{W}$ and $\dot{U}$ into Eq.(4.19) and assuming that the input flow is already at the temperature of the gas in the chamber leads to Eq.(4.22),

$$\frac{\gamma-1}{\gamma}(q_{in} - q_{out}) + \frac{1}{\rho}(\dot{m}_{in} - \dot{m}_{out}) - \dot{V} = \frac{V}{\gamma P}\dot{P} \tag{4.22}$$

If the process is assumed to be adiabatic, the pressure change rate is,

$$\dot{P} = \gamma\frac{RT}{V}(\dot{m}_{in} - \dot{m}_{out}) - \gamma\frac{P}{V}\dot{V} \tag{4.23}$$

Assuming an isothermal process, Eq. (4.22) becomes,

$$q_{in} - q_{out} = P\dot{V} - \frac{P}{\rho}(\dot{m}_{in} - \dot{m}_{out}) \tag{4.24}$$

Therefore using Eqs. (4.17) and (4.18), the time derivative of the chamber pressure is obtained as:

$$\dot{P} = \frac{RT}{V}(\dot{m}_{in} - \dot{m}_{out}) - \frac{P}{V}\dot{V} \tag{4.25}$$

Considering Eqs. (4.23) and (4.25), the only difference between the isothermal and adiabatic process is the specific heat ratio. Therefore both equations can be expressed as follows:

$$\dot{P} = \frac{RT}{V}(\alpha_{in}\dot{m}_{in} - \alpha_{out}\dot{m}_{out}) - \alpha\frac{P}{V}\dot{V} \tag{4.26}$$

where the coefficients of α, α_{in}, α_{out} are estimated based on the actual heat transfer process (Richer and Hurmuzlu, 2000a; 2000b). Al-Ibrahim and Otis (1992) experimentally measured the temperature inside the chambers of a pneumatic cylinder during both charging and discharging processes. For the charging process, the experimental temperature values were close to the theoretical adiabatic curve, while during the discharging process, the measured temperature values were closer to the isothermal curve. Therefore for the charging process, α_{in} is considered to be close to γ, whereas during the discharging process, a value of α_{out} close to 1 is considered. On the other hand, based on Al-Ibrahim and Otis (1992) evaluations, for chamber expansion/compression processes caused by the piston movements, the value of α is set to be 1.2.

The first term in Eq.(4.26) accounts for the influence of the input/output air mass flow on the chamber pressure, while the second term integrates the moving element effects (such as piston or head valve). Section 4.5.1 introduces the mass flow expression, while section 4.5.2 adapts Eq.(4.26) to the chamber 1 and 2 and to the return air chamber definitions.

4.5.1 Mass flow rate

This section introduces the mass flow expressions for flow calculation through fixed restrictions (nozzles) or variable restrictions (valves). Since such restrictions produce large pressure drops, the flow is considered compressible and turbulent. The mass flow generally depends on the downstream-upstream pressure ratio (P_d/P_u). When this pressure ratio reaches a critical value P_{cr}, the conditions are defined as sonic/choked. When the pressure ratio is less than P_{cr}, the flow is supersonic and the mass flow becomes linearly dependent on the upstream pressure. Alternatively, when the pressure ratio becomes larger than P_{cr}, the flow is considered as subsonic and the mass flow describes a nonlinear function of both pressures. Therefore the mass flow through a restriction of effective area A_{eff} is expressed as follows,

$$\dot{m}(P_u, P_d) = \frac{C_f K P_u A_{eff} N_{12}}{\sqrt{T}} \tag{4.27}$$

$$N_{12} = \begin{cases} 1 & \frac{P_d}{P_u} \le P_{cr} \\ \left[\frac{(P_d/P_u)^{\frac{2}{\gamma}} - (P_d/P_u)^{\frac{\gamma+1}{\gamma}}}{\frac{\gamma-1}{2}\left(\frac{2}{\gamma+1}\right)^{\frac{\gamma+1}{\gamma-1}}} \right]^{\frac{1}{2}} & \frac{P_d}{P_u} > P_{cr} \; and \quad \frac{P_d}{P_u} < 1 \end{cases} \tag{4.28}$$

where P_u and P_d are respectively the upstream and downstream pressures, and C_f is the restriction discharge coefficient. Eq.(4.29) gives P_{cr} and K factor is defined by Eq. (4.30),

$$P_{cr} = \left(\frac{2}{\gamma+1}\right)^{\frac{\gamma}{\gamma-1}} \tag{4.29}$$

$$K = \left[\frac{\gamma}{R}\left(\frac{2}{\gamma+1}\right)^{\frac{\gamma+1}{\gamma-1}}\right]^{\frac{1}{2}} \tag{4.30}$$

4.5.2 Cylinder and return air chambers

The chamber pressure change rate introduced by Eq.(4.26) requires to be adapted to the different chamber configurations. Eqs.(4.31), (4.32) and (4.33) describe the adapted pressure change rate for Chamber 1, Chamber 2 and the return air chamber, respectively.

$$\dot{P}_1 = \frac{RT}{V_{01} + A_1 y_{pr}} (\alpha_{in} \dot{m}\,(P_{ext}, P_1) - \alpha_{in} c_{1tr} \dot{m}\,(P_1, P_r) - \alpha_{out} c_{ex} \dot{m}\,(P_1, P_m)) - \alpha \frac{P_1 A_1}{V_{01} + A_1 y_{pr}} \dot{y}_{pr} \tag{4.31}$$

$$c_{1tr} = \begin{cases} 1 & y_{pr} > y_{rh} \;\; and \;\; P_1 > P_r \\ 0 & y_{pr} \le y_{rh} \;\; or \;\; P_1 \le P_r \end{cases}$$

$$c_{ex} = \begin{cases} 1 & (L_h - y_{hr}) < Y_{he1} \;\; and \;\; P_1 > P_a \\ 0 & (L_h - y_{hr}) \ge Y_{he1} \;\; or \;\; P_1 \le P_a \end{cases}$$

$$\dot{P}_2 = \frac{RT}{V_{02} + A_2(L - y_{pr})}(\alpha_{in}\dot{m}_2) + \alpha\frac{P_2 A_2}{V_{02} + A_2(L - y_{pr})}\dot{y}_{pr} \tag{4.32}$$

$$\dot{m}_2 = \begin{cases} -\dot{m}\,(P_2, P_r) & P_2 > P_r \\ \dot{m}\,(P_r, P_2) & P_2 < P_r \\ 0 & P_2 = P_r \end{cases}$$

$$\dot{P}_r = \frac{RT}{V_r}(-\alpha_{in}\dot{m}_2 + \alpha_{in}c_{1tr}\dot{m}\,(P_1, P_r)) \tag{4.33}$$

where V_{01} and V_{02} are the inactive volumes of chamber no.1 and 2 respectively, V_r is the return air chamber volume, and P_r is the return air chamber absolute pressure.

The head valve plays a critical role in controlling the input flow from the external chamber to chamber no.1. The head valve also controls the output flow from chamber no.1 to the atmosphere (during the exhaust process). The valve restriction controls these input and output mass flow rates. The following describes the input/output flow through the valve restriction.

4.5.2.1 Input flow

In order to calculate the mass flow rate entering the cylinder chamber no.1 through the head valve, the effective flow area (A_{eff}), as well as discharge coefficient (C_f) need to be determined. Figure 4.4 illustrates the head valve conditions.

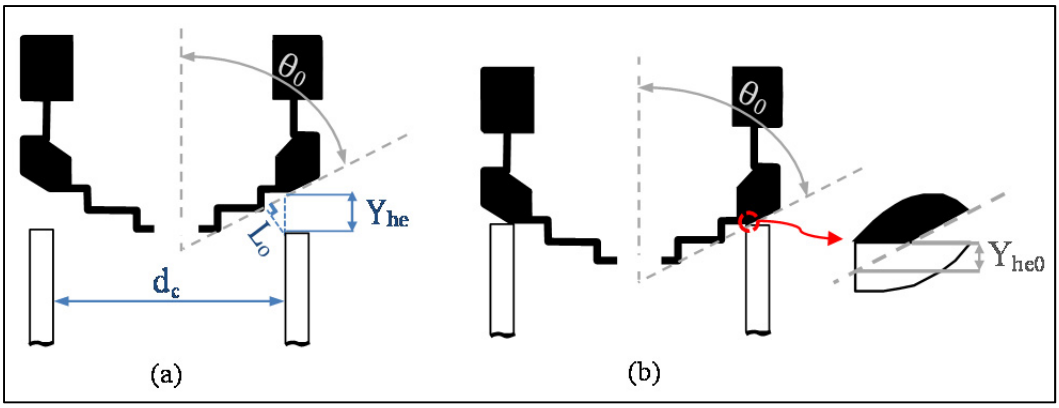

Figure 4.4 Head valve conditions: (a) Opened, (b) Close

For the cylinder chamber inflows, the head valve can be considered as a conical poppet valve. Therefore, the effective flow corresponds to the frustum of a cone with the element L_0 normal to the surface of the valve (Andersen, 2001) (Figure 4.4(a)). Eq.(4.34) gives this effective area:

$$A_{e1} = \pi Y_{he} \sin\theta_0 (d_c - Y_{he} \sin\theta_0 \cos\theta_0) \tag{4.34}$$

where d_c is the chamber no.1 diameter, and θ_0 is shown in Figure 4.4. During the head valve movement, $Y_{he} = L_h - y_{hr} - Y_{he0}$. Y_{he0} is shown in Figure 4.4(b). A_{e1} is zero for $Y_{he} \leq 0$.

The discharge coefficient was evaluated from the data published in Tsai and Cassidy (1961) for 45° conical poppet valves. The data covers the 0.390 to 0.913 pressure ratio range. Eq. (4.35) represents a fitted curve to this data,

$$C_f = -0.14\left(\frac{P_d}{P_u}\right)^3 + 0.49\left(\frac{P_d}{P_u}\right)^2 - 0.71\left(\frac{P_d}{P_u}\right) + 1.1 \tag{4.35}$$

For pressure ratios smaller than 0.390, C_f is considered to be constant and equal to C_f at 0.390. For pressure ratios greater than 0.913, C_f is considered to be constant and equal to C_f at 0.913.

Having the effective flow area (A_{e1}) and discharge coefficient (C_f), the mass flow rate entering the cylinder chamber no. 1 through the head valve can be obtained from Eq.(4.27).

4.5.2.2 Output flow

During the exhaust process, the air in chamber no.1 flows out to the atmosphere (P_a), passing through two restrictions in series: the head valve restriction with effective flow area A_{1m} and the air exhaust holes. These holes have an effective flow area A_{ma}. Figure 4.5 gives a schematic description of the restrictions series.

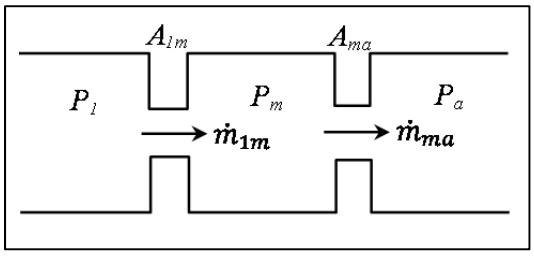

Figure 4.5 Exhaust restrictions

In a steady state, the mass flow rate through the two restrictions should be equal to (Andersen, 2001):

$$\frac{C_f K P_1 A_{1m} N_{1m}}{\sqrt{T_1}} = \frac{C_f K P_m A_{ma} N_{ma}}{\sqrt{T_m}} \tag{4.36}$$

Assuming $T_1=T_m$, Eq. (4.36) becomes:

$$\frac{P_1}{P_m} N_{1m} = C_{1m} = \frac{A_{ma}}{A_{1m}} N_{ma} \tag{4.37}$$

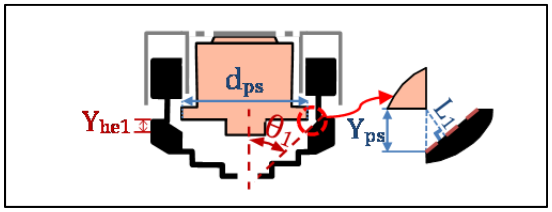

Figure 4.6 Head valve geometry for output flow

where P_m is the air pressure after passing through the head valve restriction, and A_{ma} is the total area of the air exhaust holes. As before for A_{e1}, A_{1m} is taken as the frustum of a cone, with L_1 normal to the surface of the valve, as shown in Figure 4.6. Eq. (4.38) establishes this effective area,

$$A_{1m} = \pi Y_{ps} \sin\theta_1 (d_{ps} + Y_{ps} \sin\theta_1 \cos\theta_1) \tag{4.38}$$

where $Y_{ps} = Y_{he1} - (L_h - y_{hr})$, and A_{1m} is zero for $Y_{ps} \leq 0$.

Coefficients C_{1m} in Eq.(4.39a) and C_{ma} in Eq. (4.39b) are required to calculate P_m, Eqs. (4.39) give the coefficients:

$$C_{1m} = \frac{P_1}{P_m} N_{1m} = \left[\frac{(P_1/P_m)^{\frac{\gamma-1}{\gamma}} \left[(P_1/P_m)^{\frac{\gamma-1}{\gamma}} - 1 \right]}{\frac{\gamma-1}{2} \left(\frac{2}{\gamma+1} \right)^{\frac{\gamma+1}{\gamma-1}}} \right]^{\frac{1}{2}} \tag{4.39a}$$

$$C_{ma} = \frac{P_m}{P_a} N_{ma} = \left[\frac{(P_m/P_a)^{\frac{\gamma-1}{\gamma}} \left[(P_m/P_a)^{\frac{\gamma-1}{\gamma}} - 1 \right]}{\frac{\gamma-1}{2} \left(\frac{2}{\gamma+1} \right)^{\frac{\gamma+1}{\gamma-1}}} \right]^{\frac{1}{2}} \tag{4.39b}$$

The functions C_{1m} and C_{ma} may be explicitly inverted to obtain the pressure ratios,

$$\frac{P_1}{P_m} = \left\{ \frac{1}{2} + \left[\frac{1}{4} + \frac{\gamma-1}{2} \left(\frac{2}{\gamma+1} \right)^{\frac{(\gamma+1)}{(\gamma-1)}} C_{1m}^2 \right]^{\frac{1}{2}} \right\}^{\frac{\gamma}{(\gamma-1)}} \tag{4.40a}$$

$$\frac{P_m}{P_a} = \left\{ \frac{1}{2} + \left[\frac{1}{4} + \frac{\gamma - 1}{2} \left(\frac{2}{\gamma + 1} \right)^{\frac{(\gamma+1)}{(\gamma-1)}} C_{ma}^2 \right]^{\frac{1}{2}} \right\}^{\frac{\gamma}{(\gamma-1)}} \tag{4.40b}$$

Using Eq. (4.39b) to replace N_{ma} in Eq. (4.37) yields,

$$C_{1m} = \frac{A_{ma}}{A_{1m}} C_{ma} \frac{P_a}{P_m} \tag{4.41}$$

The P_m calculation requires an iteration procedure. The procedure presented in Andersen (2001) assumes an initial value for C_{ma}, then calculates L_{ma} (=P_m/P_a) with Eq.(4.40b) and L_{1m} (=P_1/P_m) with Eqs.(4.40a) and (4.41), and, finally, compares the product of L_{1m} and L_{ma} to the ratio L_{1a} (=P_1/P_a). Then the following relation allows evaluating an improved value for C_{ma},

$$C_{ma-new} = (1 + \frac{L_{1a}/L_{1m}L_{ma} - 1}{\frac{1}{1+K_{ma}} + (1 - \frac{1}{1+K_{ma}}) \frac{1}{1+K_{1m}}}) C_{ma} \tag{4.42}$$

where k_{ma} and k_{1m} are defined as follows,

$$K_{ma} = \frac{(\gamma-1)/2\gamma}{L_{ma}^{(\gamma-1)/\gamma} - 1} - \frac{1}{\gamma}, \quad K_{1m} = \frac{(\gamma-1)/2\gamma}{L_{1m}^{(\gamma-1)/\gamma} - 1} - \frac{1}{\gamma} \tag{4.43}$$

The procedure is repeated until the calculated pressure ratio (L_{1m} L_{ma}) reaches L_{1a} within a prescribed tolerance.

The air channel influences the inflows/outflows from/into the head valve chamber and the outflow from the external chamber. Section 4.5.3 develops the air channel model.

4.5.3 Air channel model

The air channel connects the head valve to the external chamber and to the atmosphere. This channel causes a pressure drop in the steady state air flow between the outlet and inlet resulting in a delay. This delay corresponds to the time required for the acoustic wave to travel the entire length of the channel. Some studies (Andersen, 2001; Elmadbouly and Nour, 1994; Hougen et al., 1963; Schuder and Binder, 1959; Whitmore et al., 1990) analyzed flows along the pneumatic lines; most of them assumed fully developed laminar flow through the channel.

Andersen (2001) and Schuder and Binder (1959) derived the two basic flow equations for pneumatic line,

$$\frac{\partial P_{ch}}{\partial s} = -\frac{R_{ch}}{\rho A_{ch}}\dot{m}_{ch} - \frac{1}{A_{ch}}\frac{\partial \dot{m}_{ch}}{\partial t} \tag{4.44}$$

$$\frac{\partial \dot{m}_{ch}}{\partial s} = -\frac{A_{ch}}{c^2}\frac{\partial P_{ch}}{\partial t} \tag{4.45}$$

In the equations above, P_{ch} is the pressure along the channel, R_{ch} is the channel resistance, A_{ch} is the channel cross sectional area, $\dot{m}_{ch}$ is the mass flow through the channel, c is the sound speed, and s is the coordinate along the channel. Differentiating Eq. (4.44) with respect to the time (t) and Eq. (4.45) with respect to the position (s) yields,

$$\frac{\partial^2 \dot{m}_{ch}}{\partial t^2} - c^2\frac{\partial^2 \dot{m}_{ch}}{\partial s^2} + \frac{R_{ch}}{\rho}\frac{\partial \dot{m}_{ch}}{\partial t} = 0 \tag{4.46}$$

This mass flow equation may be solved using the form (Chester, 1970; Richer and Hurmuzlu, 2000a),

$$\dot{m}_{ch}(s,t) = \phi(t)v(s,t) \tag{4.47}$$

where $v(s,t)$ and $\phi(t)$ are unknown functions. The boundary and initial conditions are,

$$v(s,0)=0,\frac{\partial v}{\partial t}(s,0)=0,v(0,t)=h(t) \tag{4.48}$$

These conditions indicate that there is no flow in the channel at *t=0*. Moreover, there is no reflection from the end, and the flow profile at the inlet is an arbitrary function *h(t)*.

After manipulations (Chester, 1970; Richer and Hurmuzlu, 2000a), the mass flow at the outlet of the channel ($s=L_{ch}$) becomes

$$\dot{m}_{ch}(L_{ch},t)=\begin{cases}0 & t<L_{ch}/c\\ \phi h\left(t-\dfrac{L_{ch}}{c}\right) & t>L_{ch}/c\end{cases} \tag{4.49}$$

$$\phi=e^{-\frac{R_{ch}RT}{2P_{che}}\frac{L_{ch}}{c}} \tag{4.50}$$

where the term ϕ represents the flow attenuation through the length of the channel, L_{ch} is the channel length, and P_{che} is the pressure at the end of the channel. Eq. (4.49) shows that the flow at the outlet of the channel is delayed by L_{ch}/c. The pressure drop along the channel is:

$$\Delta \mathrm{P_{ch}}=\frac{\mathrm{R_{ch}}L_{ch}\dot{m}_{ch}RT}{P_{ch}A_{ch}}+c_{ch}\frac{P_{ch}gL_{ch}}{RT} \tag{4.51}$$

$$c_{ch}=\begin{cases}1 & trigger\ valve\ actuated\\ -1 & trigger\ valve\ released\end{cases}$$

While the first term in Eq.(4.51) represents the pressure drop caused by the channel resistance, the second term expresses the pressure gradient due to an elevation change. For fully developed laminar flow, the channel resistance becomes (Richer and Hurmuzlu, 2000a),

$$\mathrm{R_{ch}}=\frac{32\mu}{{D_{ch}}^2} \tag{4.52}$$

where μ is the air dynamic viscosity and D_{ch} is the inner diameter of the channel. In the present study, we assumed a sinusoidal input flow with 6×10^{-3} Kg/s amplitude and a frequency of 30 Hz.

4.5.4 Head valve and external chambers

The time derivatives for the pressure in the external chamber, and head valve chamber is given by:

$$\dot{P}_h = \frac{RT}{V_{0h} + A_{h1}y_{hr}}(\alpha_{in}\dot{m}_h) - \alpha\frac{P_h A_{h1}}{V_{0h} + A_{h1}y_{hr}}\dot{y}_{hr} \tag{4.53}$$

where

$$c_{tv} = \begin{cases} 1 & trigger\ valve\ released \\ 0 & trigger\ valve\ actuated \end{cases}, \dot{m}_h = \begin{cases} \phi_{in}\bar{\dot{m}}(P_{ext}, P_h) & c_{tv} = 1 \\ -\phi_{out}\bar{\dot{m}}(P_h, P_a) & c_{tv} = 0 \end{cases}$$

$$\dot{P}_{ext} = \frac{RT}{V_{ext}}(-\alpha_{in}\dot{m}\,(P_{ext}, P_1) - \alpha_{in}c_{tv}\dot{m}\,(P_{ext}, P_h)) \tag{4.54}$$

In the previous equations, V_{ext} represents the external chamber volume, and ϕ_{in} and ϕ_{out} correspond the flow attenuations given by Eq. (4.50). The variables marked by overbars represent the values delayed by the channel time delay (L_{ch} /c). Since the nailing device trigger is pulled and actuates the trigger valve at t_0, in the simulation (see Section 4.7), c_{tv} is initially set to zero.

4.6 System parameters estimation

A number of the parameters introduced above in the model (such as chamber volumes, piston effective areas, piston stroke, etc.) may be evaluated from direct measurements. Some other parameters such as the channel resistance may be calculated using available formulas.

The following develops specific experiments for the remaining parameters that cannot be evaluated from direct measurements or calculations.

The friction force between the piston and cylinder wall can be written as,

$$F_{fp} = \begin{cases} F_{sfp} sign(F_{p1}) & |\dot{y}_{pr}| < 10^{-8} \; and \; | \; F_{p1}| > F_{sfp} \\ F_{p1} & |\dot{y}_{pr}| < 10^{-8} \; and \; | \; F_{p1}| \leq F_{sfp} \\ (F_{dfp} + \beta_p \, |\dot{y}_{pr}|) sign(\dot{y}_{pr}) & |\dot{y}_{pr}| \geq 10^{-8} \end{cases} \tag{4.55}$$

$$\begin{aligned} F_{p1} = P_1 A_1 - P_2 A_2 - P_a A_r - c_r F_r - \beta_b(\dot{y}_{pr}) - k_b(y_{pr} + y_b) \\ - k_w(y_p - y_w - l_n - y_{pbp}) + M_t g \end{aligned} \tag{4.56}$$

where F_{sfp} is the static friction force, F_{dfp} is the dynamic friction force, and β_p is the viscous friction coefficient. A series of measures were conducted on a universal testing machine. This approach allows measuring the friction force as a function of the piston position inside the cylinder. The tests were repeated at constant speeds for piston velocities ranging from 5E-2 to 8.3 mm/s. As an example, Figure 4.7 shows the friction force measured at a constant velocity of 3.3 mm/s. F_{sfp} represents the average of the maximum force measured over the piston velocity range. To evaluate F_{dfp}, the static portions of the measurement curves were identified based on the maximum force decay, and eliminated from the calculation. In order to obtain a unique dynamic friction force evaluation for each speed, the portion corresponding to the dynamic force were averaged between the limits illustrated by the dashed lines shown in Figure 4.7. Finally, the averaged dynamic force F_{dfp} is described as a function of the piston velocity by a curve fit.

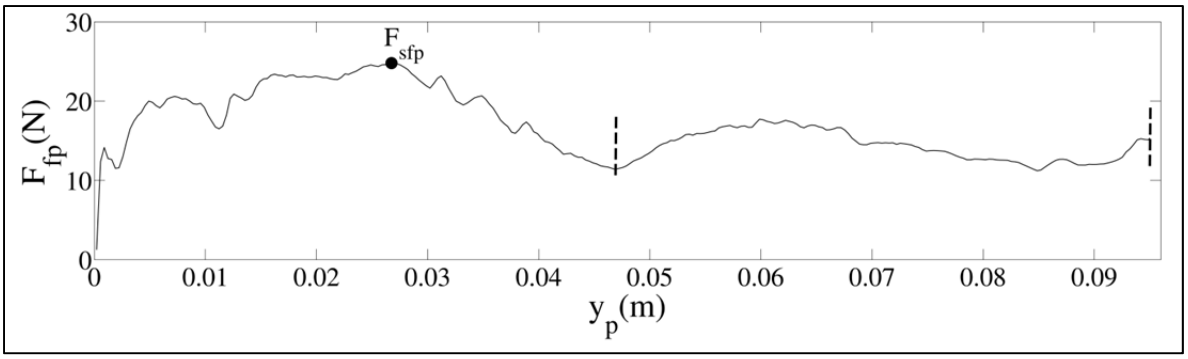

Figure 4.7 F_{fp} versus piston displacement

The friction force between the head valve and cap wall (F_{fh}) is expressed as follows,

$$F_{fh} = \begin{cases} F_{sfh} sign(F_{h1}) & |\ \dot{y}_{hr}| < 10^{-8}\ \ and\ \ |\ F_{h1}| > F_{sfh} \\ F_{h1} & |\ \dot{y}_{hr}| < 10^{-8}\ \ and\ \ |\ F_{h1}| \le F_{sfh} \\ \left(F_{dfh} + \beta_h\ |\ \dot{y}_{hr}|\right) sign(\ \dot{y}_{hr}) & |\ \dot{y}_{hr}| \ge 10^{-8} \end{cases} \quad (4.57)$$

$$F_{h1} = P_h A_{h1} - P_{ext} A_{h2}\ \ + F_s - k_c(y_{hr} + y_c) + M_h g \quad (4.58)$$

where F_{sfh} is the static friction force, F_{dfh} is the dynamic friction force, and β_h is the viscous friction coefficient. The experimental approach described above for F_{fp} was repeated to establish F_{fh}.

The stiffness and damping of the piston bumper (k_{pb} and β_{pb}) and stopper (k_{ps} and β_{ps}) were determined through measurement of the displacement transmissibility using the test set-up recommended in the ISO 18437-5:2011(E) standard (ISO, 2011).

Ahmadabadi et al. (2015b) presented an empirical model predicting F_r imposed on nails when penetrating Plywood panels at quasi-static velocities (velocity range 20 to 500 mm/min). This study uses the approach put forward in Ahmadabadi et al. (2015b) to develop a solid wood empirical model ((Eq. (4.59)). The resulting equation accounts for different nail sizes and geometries, and solid wood species. More details about development of solid wood PRF model can be found in Appendix I. Eq. (4.59) is integrated in the calculation procedure to evaluate F_r during the nail penetration.

$$F_r = H_{Mw} l_n \left[0.085 + 2.038 \frac{(y_p - y_w - y_{pbp})}{l_n} - 12.95 \left(\frac{y_p - y_w - y_{pbp}}{l_n}\right)^2 + 46.49 \left(\frac{y_p - y_w - y_{pbp}}{l_n}\right)^3 - 94.97 \left(\frac{y_p - y_w - y_{pbp}}{l_n}\right)^4 + 110.18 \left(\frac{y_p - y_w - y_{pbp}}{l_n}\right)^5 - 67.56 \left(\frac{y_p - y_w - y_{pbp}}{l_n}\right)^6 + 16.99 \left(\frac{y_p - y_w - y_{pbp}}{l_n}\right)^7 - 122.91 \left(\frac{\mathrm{l_n} \rho_w}{H_{Mw}}\right) - 1.15 \left(\frac{D}{l_n}\right)\right]^2 \quad (4.59)$$

where D is the nail diameter. The wood hardness modulus (H_{Mw}), wood density (ρ_w), and the moisture content of the wood specimens were measured according to the ASTM-D1037(ASTM, 2012) and ASTM-D4442-07(ASTM, 2007) standards. The present paper only considers Pine wood. Table 4-2 shows the values corresponding to this wood type. The moisture content shown in Table 4-2 is similar to the conditions encountered in the construction industry.

The compression spring force (F_s) was also measured on the same universal testing machine. The force was evaluated as a function of the spring compression. The test speed was 1.67E-5 m/s. Eq.(4.60) gives the curve fitted on the measured data.

$$F_s = 4.17 + 79135.7\, y_s - 7.55\text{E}7\, y_s^2 + 3.56\text{E}10\, y_s^3 - 8.57\text{E}12\, y_s^4 + 1.13\text{E}15\, y_s^5 - 8.28\text{E}16\, y_s^6 + 3.14\text{E}18\, y_s^7 - 4.79\text{E}19\, y_s^8 \quad (4.60)$$

where y_s is the spring displacement, which due to its preload length (y_{sp}) is given by:

$$y_s = L_h - y_{hr} + y_{sp} \quad (4.61)$$

Figure 4.8 shows the experimental data and the curve fitted for F_s.

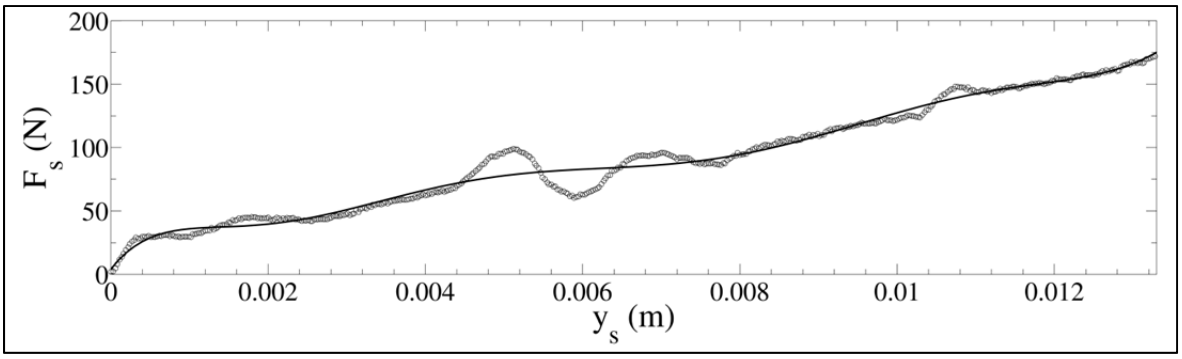

Figure 4.8 Compression spring force. Circles: Experimental data; Solid line: fitted model

Table 4-2 Wood parameter values

Parameter	**value**
H_{Mw} (N/mm)	383.64
ρ_w (kg/m^3)	429.46
Wood moisture content (%)	5.6

The contact stiffness k_{hc1}, k_{hc2} describe the nailing device cap and cylinder stiffness established from the following relation,

$$k = \frac{E_e A_e}{L_e} \tag{4.62}$$

where k, E_e, A_e, and L_e are the element stiffness, elastic modulus, cross sectional area and length, respectively. The nailing device cap and the cylinder are made of steel and aluminum, respectively. Eq.(4.62) was also used to calculate k_{wsn} and k_{ws}. For those stiffness (k_{wsn} and k_{ws}) E_e is the elastic modulus of the pine wood (Green et al., 1999).

Table 4-3 System parameter values

Parameter	**value**
F_{sfp}(N)	21.05

Table 4-3 (Continued)

Parameter	value
F_{dfp}(N)	11.73
β_p(Ns/mm)	0
F_{sfh}(N)	26.36
F_{dfh}(N)	17.68
β_h(Ns/mm)	0
$k_{pb}(N/mm)$	9.8E2
β_{pb}(Ns/mm)	0.265
$k_{ps}(N/mm)$	11.2E2
β_{ps}(Ns/mm)	0.226
k_{hc1}(N/mm)	1.10E8
k_{hc2}(N/mm)	2.14E05
k_{wsn}(N/mm)	5.1E5
k_{ws}(N/mm)	5.1E5
k_{sg}(N/mm)	2.97

Finally to determine the safety guard spring stiffness, k_{sg}, the spring compression force was measured as a function of the displacement. The final spring constant represents an average evaluation over the displacement range evaluated. Table 4-3 shows all the experimentally measured parameter values.

4.7 Numerical resolution

Eqs.(4.1), (4.8), (4.11), (4.14), (4.31)-(4.33), (4.53), and (4.54) describe the complete pneumatic nailing device operation. Figure 4.9 describes the solution algorithm, where $Cond_1$, $Cond_2$, and $Cond_3$ are expressed as follows,

$$Cond_1 = sign\left(\dot{y}_p(t_i)\right) + sign\left(\dot{y}_p(t_{i-1})\right) \tag{4.63}$$
$$Cond_2 = t_{END} - t_i$$
$$Cond_3 = y_g - y_w + y_{msg}$$

where t_i and t_{i-1} are the i^{th} and $(i\text{-}1)^{th}$ time iteration, and t_{End} is the time at the end of the entire process. The numerical resolution was performed using ODE15s function of MATLAB.

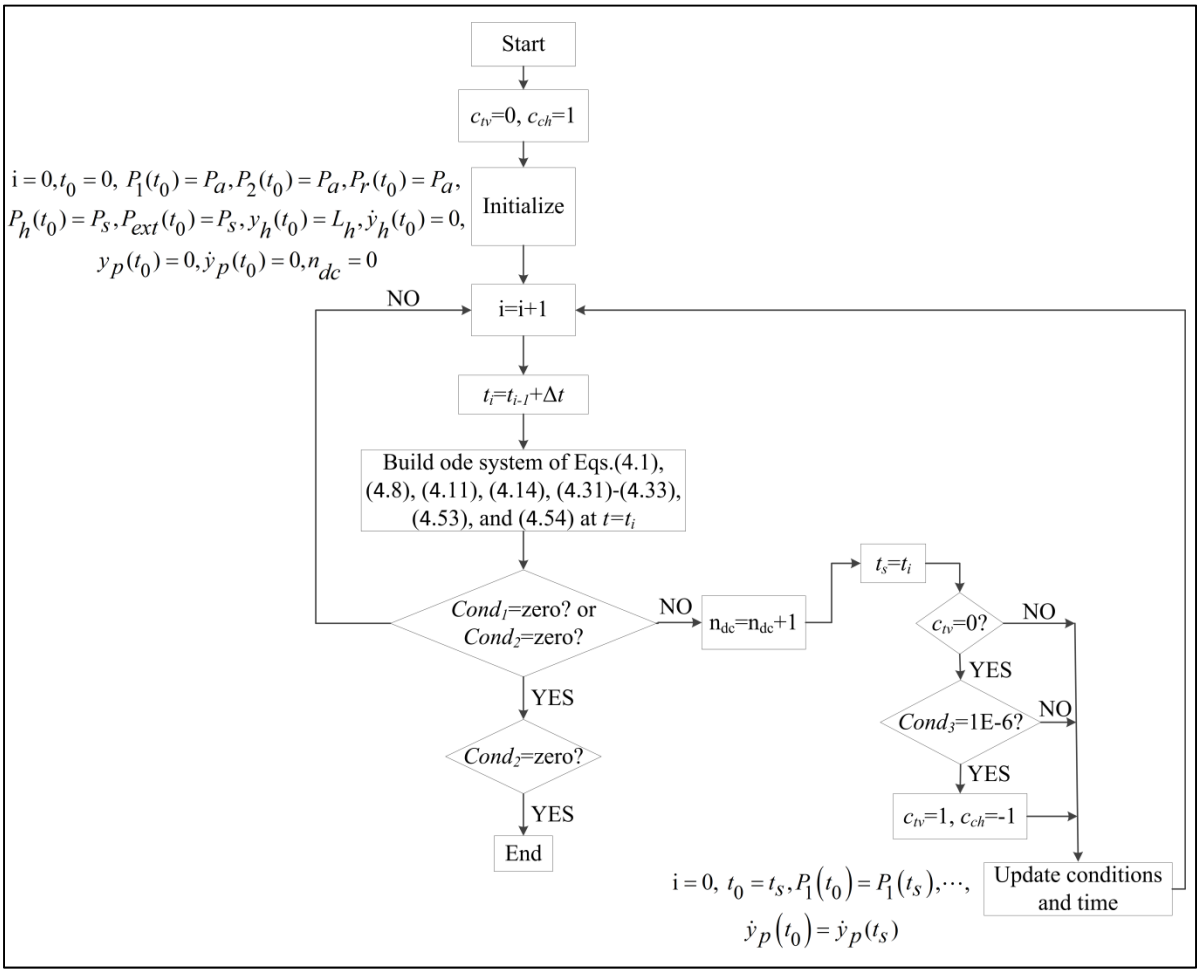

Figure 4.9 Algorithm flow chart

4.8 Model experimental validation and simulation results

A series of experiments were conducted on a Bostitch N80 CB-Coil framing nailer to validate the developed model. The nailer air pressure was set to 763.2 kPa. These tests measured the air pressures in chamber no.1 and in the return chamber from two piezoelectric pressure transducers integrated into the nailer. The pressure transducers positions are shown in Figure 4.10 and Figure 4.11. The transducer position and installation method were selected to avoid perturbing the flow rate and the external chamber volume. The maximum piston stroke is 121.25 mm; the chamber no.1 pressure transducer (PT-I) is placed at 50.51 mm from the stroke beginning. Figure 4.10 also shows the high speed camera integrated into the setup to capture the process motion (10,000 frames/sec).

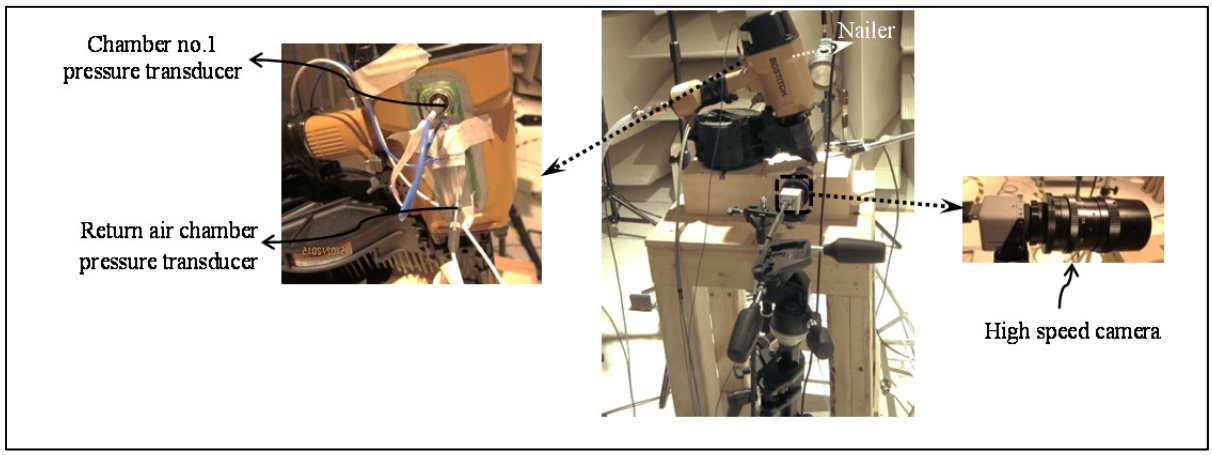

Figure 4.10 Experimental set-up

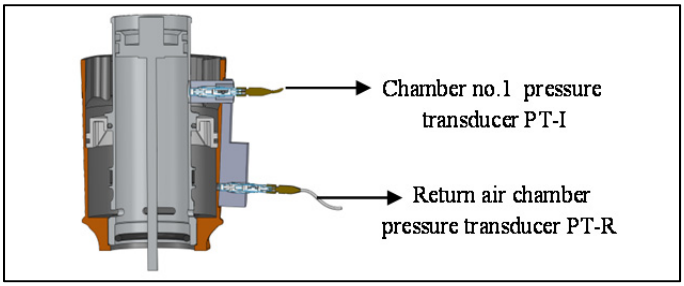

Figure 4.11 Section view of the nailer instrumented with pressure transducers

Figure 4.12 compares the air pressures predicted by simulation to the experimental air pressure measurements (P_1 and P_r). The time positions t_0 to t_{18} indicated on the signals correspond to the events described in section 4.3. In addition to the simulation time indicators identified by an *s*, the graph also includes the experimental time markers t_6, t_7, t_9, t_{14} and t_{15}. These time positions were identified by means of high speed videos analysis (t_6 and t_9) or from the pressure signals (t_7, t_{14}, and t_{15}).

The precision of the model predictions is established at these four points. Because of its position, the transducer PT-I measurement starts at t_7. Therefore, in Figure 4.12 the P_1 experimental curve starts at t_7 and position t_6 is indicated on the P_r curve.

Before the nail penetration beginning at t_6, the model predictions are in good agreement with the experimental P_r measurements. Compared to the experimental evaluation, the model predicts the t_6 position with a precision of 99.9%.

Between the nail penetration beginning at t_6 and the piston return at t_{14} the measured and model-predicted P_1 show a visible difference. This difference results from the F_r calculation model, which was developed for a speed range lower than the nail penetration speed, and consequently affects the nailing device model precision. Nevertheless, the predicted and measured t_7 positions are in perfect agreement, while the predicted P_1 pressure at this position shows a correspondence of 94.8% with the experimental measurement. The difference between the model predicted measurements show a maximum around t_9, where, while the position t_9 is around 0.91 time t_{9s}, the model predicted P_1 value is 1.25 time the measured pressure. In fact, the pressure difference between t_9 and t_{9s} affects the predicted nail penetration duration. The simulated duration is slightly greater than the real time required for a complete nail penetration. In other words, the predicted average penetration velocity is under evaluated. The model precision increases around t_{13s}. After the nail penetration end or after the influence of F_r, the model precision appears to be better. For example, the ratio t_{14}/t_{14s} is 0.96, while the predicted pressure is 0.93 time the measured P_1 value. Finally, at t_{15}, the time ratio t_{15}/t_{15s} is 1.02, while the simulated P_1 is 1.1 time the measurement.

Despite the penetration force approximation, the model-predicted P_r is in excellent agreement with the experimental measurements P_r. For instance, at t_9, the measured-predicted P_r ratio is 1.00. The lowest simulation precision occurs between t_{8s} and t_{9s}. Nevertheless, over this time range, the model precision remains excellent. Close to t_{16s}, the pressure inside the return air chamber reaches a practically static condition. Therefore, since the pressure transducers added to the nailer are piezoelectric devices and only detect pressure variations, after t_{16} the pressure measurements are not accurate.

The global model precision may be established by the pressure ratio $P_{measured}/P_{simulated}$: averaging these ratios at t_9, t_{14} and t_{15} reveals a correspondence of 0.93 and 0.96 for P_l and P_r, respectively.

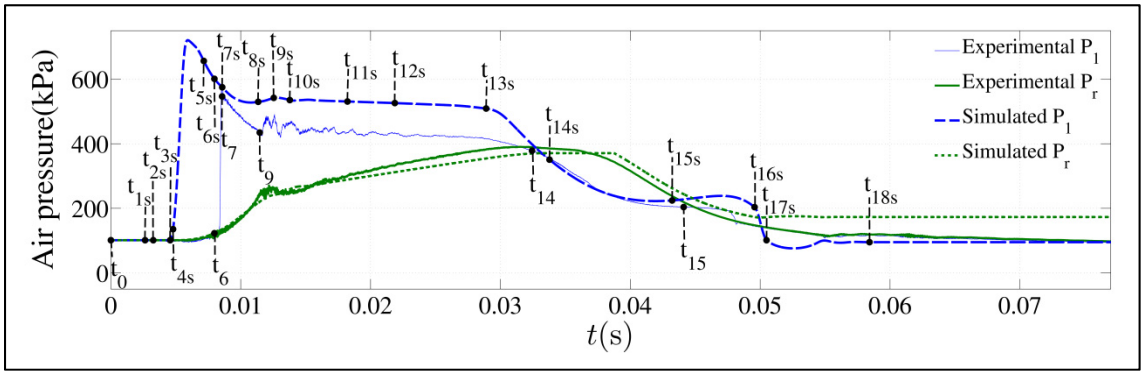

Figure 4.12 Air pressure in chamber no.1 and return air chamber

Figure 4.13 presents the model predictions for the piston displacement (y_{pr}), velocity ($\dot{y}_{pr}$), and acceleration ($\ddot{y}_{pr}$). The end of the nail penetration at t_{9s} is associated with piston-rod assembly oscillations triggered by a significant upward force increase imposed on the nailing device by the nail head contacting the wood piece. These oscillations result in impact between the piston and the bumper visible in the $\dot{y}_{pr}$ response. These oscillations last until t_{11s}. Ahmadabadi et al. (2016) indicated that the piston oscillations intensify the nailing device body vibrations and generated noise. Between t_{14s} and t_{16s}, the piston upward displacement remains smooth, whereas due to the impact between the piston and the piston stopper at t_{16s}, the piston-rod assembly starts oscillating again.

Figure 4.14 presents the head valve displacement (y_{hr}) and velocity ($\dot{y}_{hr}$). The graph shows that the head valve response includes two impact regions: during its opening phase between t_{1s} and t_{7s}, and during its closing phase between t_{12s} and t_{14s}. While these oscillations demonstrate no noticeable influence on the piston-rod assembly movement, they certainly engender vibrations having the potential of generating noises.

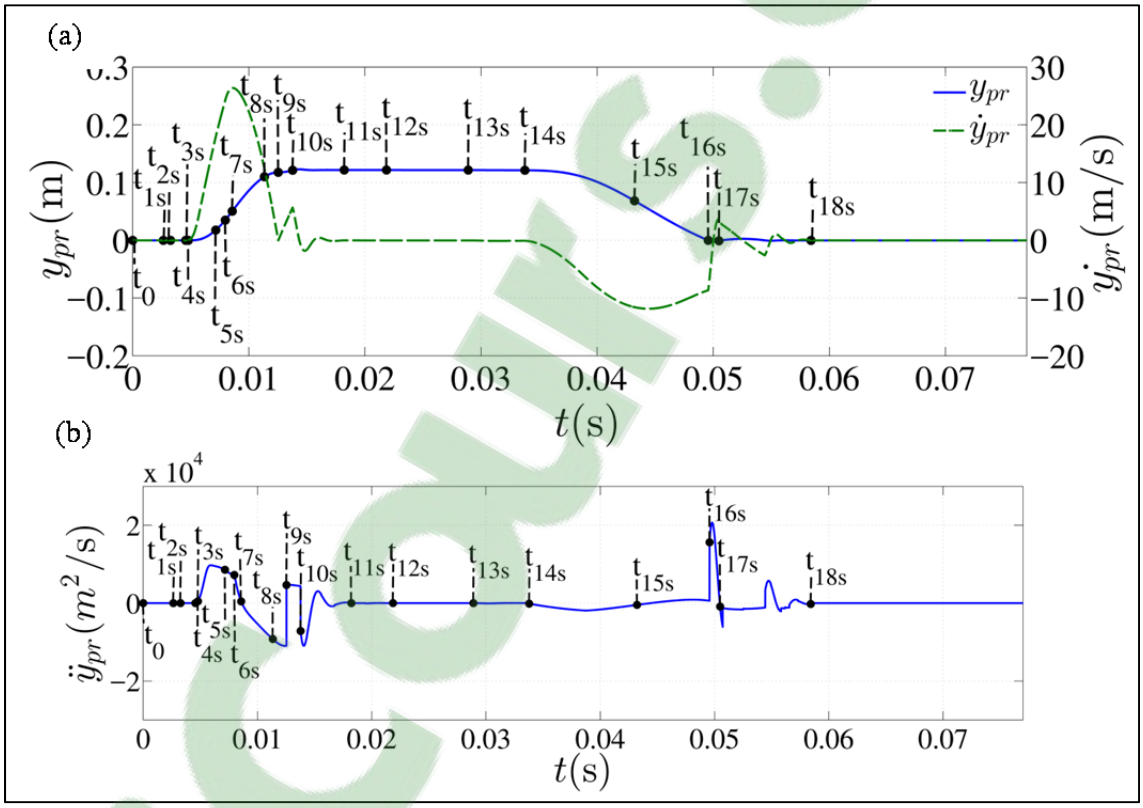

Figure 4.13 Model-predicted piston: (a) velocity and displacement, (b) acceleration.

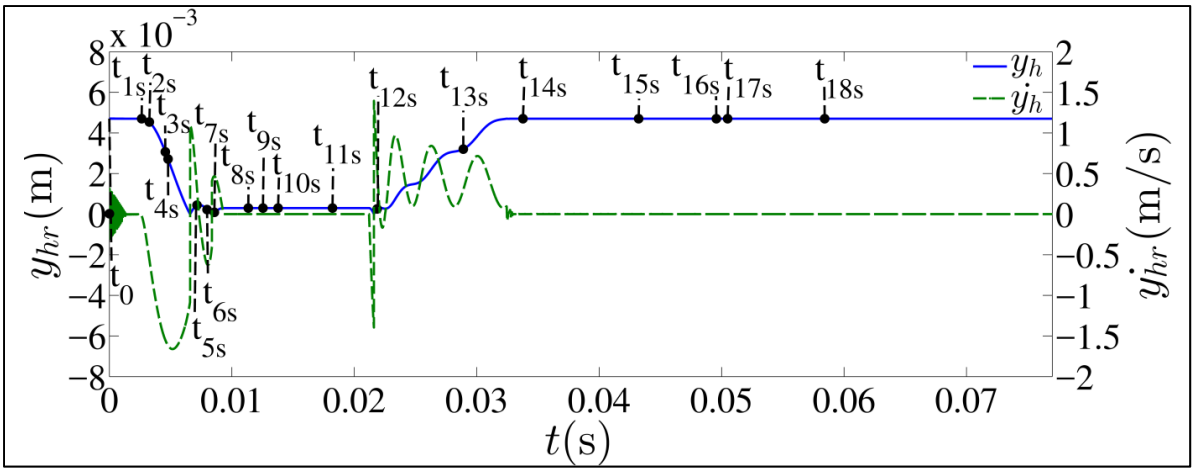

Figure 4.14 Model-predicted head valve velocity and displacement

As described before, the outflows from the fixed and variable restrictions may represent strong noise sources, particularly when the flow is in the sonic or supersonic condition. Figure 4.15(a) shows the ratio of the ambient pressure to chamber no.1 pressure for the duration of the air exhaust process between t_{13s} and t_{17s}. Since $P_a/P_1 < P_{cr}$ (P_{cr}=0.528 for air) for most of the exhaust process duration, this figure shows that the flow is mostly supersonic. This observation agrees with the finding of Ahmadabadi et al. (2016), which identified the air exhaust as the dominant noise source.

Figure 4.15(b) presents the ratio of chamber no.1 pressure to external chamber pressure during the head valve opening period and the open position duration. The graph shows that during the first part of the head valve opening phase around t_{3s} and t_{4s}, the flow is supersonic ($P_1/P_{ext} < P_{cr}$), while after this period it remains subsonic. This description also agrees with the observations published in Ahmadabadi et al. (2016), where the first part of the valve opening phase was associated with a significant contribution of the air exhaust to the generated noise, while the head valve opened position was shown to correspond to low noise levels.

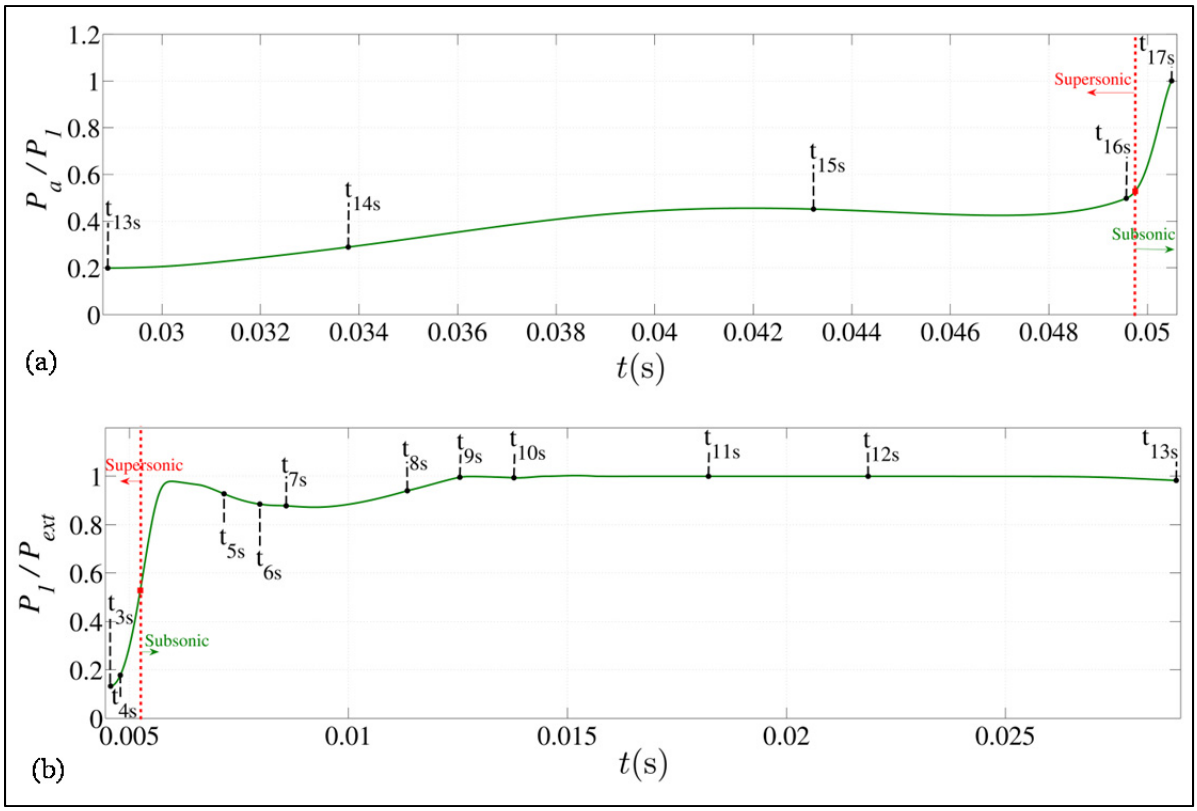

Figure 4.15 Downstream-to-upstream pressure ratio: (a) P_a/P_1 , (b) P_1/P_{ext}

4.9 Conclusion

This study developed a mathematical modeling procedure for pneumatic nailing devices. The representation integrates all the device operation phases and physical processes involved during the nailing operation. The model accounts for the dynamics of the chamber pressures, the moving parts, the nonlinear interactions and impacts between various fixed and moving components, the nailing device body, and the workpiece. The following system parameters were established from experimental measurements and integrated into the proposed representation: the friction between moving surfaces; the materials stiffness and damping properties; and the spring stiffness. The model also integrates a nonlinear empirical formulation to predict the nail penetration resistance force.

The investigation included a comprehensive experimental validation approach based on chamber no.1 pressure and return chamber pressure measurements made on a selected nailer.

Compared to the experimental evaluations, the modeling procedure was shown to be accurate; averaging the measured to simulated air pressure ratios established at important time positions ($P_{measured}/P_{simulated}$) revealed agreement levels of 0.93 and 0.96 for chamber no.1 and return chamber predictions, respectively.

The final model represents a powerful simulation tool for prediction of pneumatic nailing devices dynamic response, and would be helpful to evaluate any design modifications.

4.10 Acknowledgments

The support of NSERC (Natural Sciences and Engineering Research Council of Canada) is gratefully acknowledged.

CONCLUSION AND RECOMMENDATIONS

High levels of noise emitted by pneumatic nailing devices put construction workers at the risk of hearing loss. This health problem comes from the lack of appropriate technology such as low noise devices which in turn results from the lack of scientific knowledge about designing the reduced noise devices. The present study belongs to a broader investigation aiming to reduce noise emissions in pneumatic nailing devices. As the first step toward this goal, this study developed the essential tools and knowledge needed to redesign the pneumatic nailing device while making the following four contributions:

(1) Identifying and ranking the noise sources in a pneumatic nailing process;
(2) Developing an empirical prediction law for nail-wood penetration resistance force at quasi-static penetration velocities;
(3) Designing and fabricating a test machine for conducting nail driving experiments at high penetration velocities.
(4) Developing a dynamic model of the pneumatic nailing process.

As the first contribution, Chapter 1(article 1) presented a comprehensive study of the noise sources in a pneumatic nailing device process. The analysis identified the physical processes involved in the machine operation and provided a detailed separation of the noise generation mechanisms in 13 successive time sequences. Ranking of the noise sources showed that the workpiece vibrations is the predominant noise source in either case of having a realistic test arrangement (worktable setup) or using a sand-filled enclosure around the workpiece (sandbox setup). With the worktable setup, the workpiece was the main contributor to the total noise, while the air exhaust and machine body were ranked as the second and third noise sources, respectively. With the sandbox setup, the workpiece noise was reduced, but remained the dominant source with the air exhaust, in equal measure.

Regardless of the setup, the air exhaust noise remained visible during the whole nailing process. The air exhaust dominated the measure before the nail penetration beginning, while workpiece vibrations represented the main source during the nail penetration and remained dominant until the start of the air exhaust process. Between the end of nail penetration and

start of the air exhaust process, the machine body contribution goes over the air exhaust. This period of time corresponds to important internal air flows, strong body vibrations, and piston oscillations. These vibrations are resulted from the reaction force imposed on the nailing device during the nail penetration. By the start of the air exhaust process, the air exhaust source preponderates over the two other sources. The analysis in frequency domain showed that the air exhaust has a more significant influence below 0.1 kHz. For both workpiece and air exhaust sources, the maximum power level appeared at 0.5 kHz. Above 0.1 kHz, the machine body contribution only surpassed the air exhaust power level over the $2.0kHz \leq f \leq 5.0kHz$ range. Also, the workpiece contribution surpasses the air exhaust at frequencies above 1.0 kHz.

The limitations of article 1 and future recommendations include:

- The findings of this article were obtained under the laboratory conditions. To represent more realistic conditions, a future study should measure the nailing device noise emissions in a construction field as different workers are using the device.
- Though the worktable setup used for the experiments in this study is a more realistic test arrangement compared to the sandbox setup, it does not fully represent the field conditions where for instance two pieces of wood are fastened together. In the future, this effect should be considered in designing the test setup.
- This article studied the noise sources in one type and commercial brand of the pneumatic nailing device while the contribution of the sources might depend on the type and brand of nailing device. As a next step, the contribution of the sources should be compared between different commercial types and brands.

In terms of the second contribution, chapter 2 (article 2) studied the tribo-dynamic interactions appearing at the wood-nail interface during fastening, and developed a prediction law for the nail penetration resistance force when driven into plywood panels at quasi-static velocities.

The analysis of the tribo-dynamic interactions at the wood-nail interface showed that the nails with annularly threaded shank type generate a penetration resistance largely dictated

by the deformation-fracture component, while the smooth shank type, and by extension, the helically threaded geometry, lead to penetration resistance controlled by the friction. The parametric analysis demonstrated that for a quasi- static speed range, penetration velocity variations result in inconsequential effects, and could be neglected. Moreover, for softwoods, the PRF could be considered as largely determined by the wood hardness.

The final PRF prediction law was derived from analysis of extensive experiments conducted over the parameter space. Model validations demonstrated reliability of formulation in predicting the PRF with an overall precision above 89%.

In developing this law, the penetration velocity factor was considered over a limited range (quasi-static). To extend the prediction model, a future study should examine the high velocity range.

Moreover, in future redesign of the nailing device, changing the piston-rod assembly mass (or impactor mass) might be one solution to the nailing device noise problem. Though varying this mass might affect the PRF profile, the PRF prediction law developed in chapter 2 does not include the influence of the impactor (or projectile) mass parameter. Therefore, a future extension of the PRF model should take into account a wide range of velocities and impactor masses.

Chapter 3 contributed to the above-mentioned extension of the PRF law through design and fabrication of an advanced test machine. This machine can be later used to conduct the nail penetration tests over a wide range of penetration velocities and impactor masses including the nailing device average penetration velocity and piston-rod assembly mass, respectively.

A future study should follow the detailed experimental procedure provided in chapter 3 and develop the extended PRF law by performing a statistical analysis on the measured data.

In terms of the fourth contribution, chapter 4 (article 3) developed a detailed model of the pneumatic nailing process integrating all the device operation phases composing the nailing process. The model accounts for the dynamics of the chamber pressures, the moving

parts, the interactions and impacts between the fixed and moving components, and includes the nailing device body and workpiece. All the system parameters integrated into the proposed model were established from experimental measurements. The model integrated an empirical prediction law for nail-solid wood PRF developed following the approach introduced in chapter 2. According to the model predictions, the air exhaust flow is in the supersonic condition for most of the exhaust process. This agrees with the findings of article 1 which identified the air exhaust process as one of the major noise generation mechanisms. The final representation is validated through a comparison of the predicted piston motion and air pressures to experimental measurements. Averaging the measured to simulated air pressure ratios established at important time positions shows an agreement level higher than 93%.

Arbitrary variation of the PRF profile in the dynamic model indicated a strong influence of the PRF on the dynamic model predictions. Thus the above-mentioned future extension of the PRF law will improve the dynamic model accuracy.

Moreover, the simulation model can be further extended to include the acoustic radiation from the pneumatic nailing device and the workpiece.

Overall, this research presented a novel and powerful tool which relates design parameters of the nailing device to the sound generation mechanisms. Using this tool, the effective design modifications can be first identified through simulation and then implemented to develop new types of nailing devices with reduced noise level. This technology advancement would improve working conditions in the construction fields.

APPENDIX I

AN EMPIRICAL PREDICTION LAW FOR QUASI-STATIC NAIL-SOLID WOOD PENETRATION RESISTANCE

This appendix gives the unpublished results of the empirical prediction model for nail penetration resistance force at quasi-static velocity ranges in the case of solid wood based on the same procedure presented in article 2 (chapter 2, section 2.3) in the case of plywood. These results were not included in article 2 since the article concentration was on studying the influence of complexities involved in plywood (composite wood products) on the PRF. Besides article 2 was the first study of its kind to investigate tribo-dynamics of nail-wood penetration and the effect of many important parameters (such as nail geometry, size, and etc.) on the PRF. Therefore solid wood PRF results were beyond the purpose of article 2 but will be presented in future publications.

This appendix results are used in article 3 (chapter 4) for the development of the nonlinear dynamic modeling of pneumatic nailing devices. The study includes three solid wood types: (1) Douglas-Fir, (2) Pine, (3) Poplar. Table A I-1 shows the hardness modulus, density, and moisture content of the solid woods. The proposed investigation examines three shank types: (1) smooth, (2) annularly threaded, and (3) helically threaded. Table A I-2 presents the evaluated diameters for each shank type. As demonstrated in Chapter 2, the penetration velocity has an insignificant influence on the PRF at quasi-static ranges. Therefore here all the tests were conducted at 500 mm/min penetration velocity.

Table A I-1 Hardness modulus, density values, and moisture content

	Douglas-Fir	***Pine***	***Poplar***
$\boldsymbol{H_M(\mathrm{N/mm})}$	567.47	383.64	375.35
$\boldsymbol{\rho(kg/m^3)}$	450	429.46	413.04
Moisture content (%)	5.6	5.7	5.6

Table A I-2 Nail shank types

Nail penny size	Smooth nails	Annularly threaded nails	Helically threaded nails
3d	✓		
4d	✓		
6d			
8d	✓	✓	✓
10d	✓	✓	✓
12d	✓		

The nail penetration resistance formula (Eq. (4.59)) results from nonlinear regressions fitted to the data sets. Table A I-3 presents the statistical measures of the model average performances.

Table A I-3 Statistical measures of model average performances

Descriptors	Solid woods model
R^2	91.84%
SEE	0.01408
MAE	0.01075

LIST OF REFERENCES

Adelberg, J, R Anderson, B Kuykendall, T Schwartz, K Vu and M Rao. 2002. *Study of Noise Transmission from a Pneumatic Nail Gun*. Coll. « ME4704 Project Report, National Institute for Occupational Safety and Health (NIOSH) ». Michigan: Michigan Tech, 27 p.

Ahmadabadi, Z Nili , F Laville and R Guilbault. 2015a. « Study of parameters influencing pneumatic nail-gun noise ». In *INTER-NOISE and NOISE-CON Congress and Conference Proceedings*. Vol. 250, p. 17-28. Institute of Noise Control Engineering.

Ahmadabadi, Z Nili , F Laville and R Guilbault. 2016. « Time domain identification and ranking of noise sources of a pneumatic nail gun, submitted to Journal of Applied Acoustics ».

Ahmadabadi, Z Nili, F Laville and R Guilbault. 2015b. « An empirical prediction law for quasi-static nail–plywood penetration resistance ». *Construction and Building Materials,* vol. 88, p. 126-133.

Ahmadabadi, ZN, F Laville and R Guilbault. 2015c. « Studying of the noise sources in a pneumatic nail-gun process ». *The Journal of the Acoustical Society of America,* vol. 138, n^{o} 3, p. 1937-1937.

AITC. 1986. *Timber construction manual*, 3rd. New York: J. Wiley and Sons, 836 p.

Akay, A. 1978. « A review of impact noise ». *The Journal of the Acoustical Society of America,* vol. 64, n^{o} 4, p. 977-987.

Al-Ibrahim, MA, and DR Otis. 1992. « Transient air temperature and pressure measurements during the charging and discharging processes of an actuating pneumatic cylinder ». In *Proceedings of the 45th National Conference on Fluid Power*.

Alonso, J., J. M. López, I. Pavón, M. Recuero, C. Asensio, G. Arcas and A. Bravo. 2014. « On-board wet road surface identification using tyre/road noise and Support Vector Machines ». *Applied Acoustics,* vol. 76, p. 407-415.

Andersen, BW. 2001. *The analysis and design of pneumatic systems*. Krieger Publishing Company.

ASTM. 2007. *Standard test methods for direct moisture content measurement of wood and wood-base materials*. International standards D4442-07. United States: ASTM International, 6 p.

ASTM. 2012. *Standard test methods for evaluating properties of wood-base fiber and particle panel materials*. International standards D1037-12. United States: ASTM International, 32 p.

Aytekin, A. 2008. « Determination of screw and nail withdrawal resistance of some important wood species ». *International Journal of Molecular Sciences,* vol. 9, n° 4, p. 626-637.

Badino, A, D Borelli, T Gaggero, E Rizzuto and C Schenone. 2016. « Airborne noise emissions from ships: Experimental characterization of the source and propagation over land ». *Applied Acoustics,* vol. 104, p. 158-171.

Bartelt, PA, W Ammann and E Anderheggen. 1994. « The numerical simulation of the impact phenomena in nail penetration ». *Nuclear Engineering and Design,* vol. 150, n° 2, p. 431-440.

Beiers, JL. 1966. « A study of noise sources in pneumatic rock drills ». *Journal of Sound and Vibration,* vol. 3, n° 2, p. 166-194.

Berger, E.H., L.H. Royster and DP Driscoll. 2003. *The noise manual*, Revised Fifth edition. Fairfax, VA: : AIHA Press.

Bharath, S., B. C. Nakra and K. N. Gupta. 1990. « Mathematical Model of a Railway Pneumatic Brake System With Varying Cylinder Capacity Effects ». *Journal of Dynamic Systems, Measurement, and Control,* vol. 112, n° 3, p. 456-462.

Bi, F, L Li, J Zhang and T Ma. 2015. « Source identification of gasoline engine noise based on continuous wavelet transform and EEMD–RobustICA ». *Applied Acoustics,* vol. 100, p. 34-42.

Boll, SF. 1979. « Suppression of acoustic noise in speech using spectral subtraction ». *Acoustics, Speech and Signal Processing, IEEE Transactions on,* vol. 27, n° 2, p. 113-120.

Branco, JM, PJS Cruz and M Piazza. 2009. « Experimental analysis of laterally loaded nailed timber-to-concrete connections ». *Construction and Building Materials,* vol. 23, n° 1, p. 400-410.

BSI. 1999. *Acoustics: Noise test code for fastener driving tools-Engineering method*. UK: BSI 20 p.

Campillo-Davo, N, R Peral-Orts, E Velasco-Sanchez and H Campello-Vicente. 2013. « An experimental procedure to obtain sound power level of tyre/road noise under Coast-By conditions ». *Applied Acoustics,* vol. 74, n° 5, p. 718-727.

Carvalho, EP, and EVM Carrasco. 2010. « Influence of test specimen on experimental characterization of timber–concrete composite joints ». *Construction and Building Materials,* vol. 24, n° 8, p. 1313-1322.

Celebi, G, and M Kilic. 2007. « Nail and screw withdrawal strength of laminated veneer lumber made up hardwood and softwood layers ». *Construction and Building Materials,* vol. 21, n° 4, p. 894-900.

Chester, CR. 1970. *Techniques in partial differential equations*. McGraw-Hill Companies.

Chow, GC, and G Reethof. 1980. « A study of valve noise generation processes for compressible fluids ». In *American Society of Mechanical Engineers, Winter Annual Meeting*. (Chicago,). Vol. 1, p. 11.

Chung, JY, MJ Crocker and JF Hamilton. 1975. « Measurement of frequency responses and the multiple coherence function of the noise-generation system of a diesel engine ». *The Journal of the Acoustical Society of America,* vol. 58, n° 3, p. 635-642.

Crocker, MJ. 2007. *Handbook of noise and vibration control*. John Wiley & Sons.

CSST. 2015. *Statistiques annuelles 2014*. Quebec, Canada, 160 p.

Dias, A, JW Van de Kuilen, S Lopes and H Cruz. 2007. « A non-linear 3D FEM model to simulate timber–concrete joints ». *Advances in Engineering Software,* vol. 38, n° 8, p. 522-530.

Elmadbouly, EE, and MA Nour. 1994. « Modelling, simulation and sensitivity analysis of a straight pneumatic pipeline ». *Energy Conversion and Management,* vol. 35, n° 1, p. 61-77.

Goldsmith, W. 1960. *Impact: The theory and physical behavior of colliding solids*. London: Edward Arnold Publishers.

Gong, M, S Delahunty and YH Chui. 2014. « Influence of number of finger joints per stud on mechanical performance of wood shearwalls ». *Construction and Building Materials,* vol. 50, p. 335-339.

Green, DW, JE Winandy and DE Kretschmann. 1999. « Mechanical properties of wood ». In *Wood handbook : wood as an engineering material*. p. 45. Madison, WI: USDA Forest Service, Forest Products Laboratory.

Hodgson, D. C. 1976. « Platen deceleration as a mechanism of noise production in impact forming machines ». *Journal of Mechanical Engineering Science,* vol. 18, n° 3, p. 126-130

Hodgson, M, and I Li. 2006. « Experimental study of the noise emission of personal computer cooling fans ». *Applied Acoustics,* vol. 67, n° 9, p. 849-863.

Holmes, DG. 1973. « Aerodynamic impact sounds ». Ph.D. thesis. Massachusetts Institute of Technology.

Hougen, J.O., O. R. Martin and R. A. Walsh. 1963. « Dynamics of Pneumatic Transmission Lines ». *Energy Conservation and Management,* vol. 35, p. 61-77.

Hu, Fu-Chieh. 2009. « Investigation on the Effects of Gas dynamics on the Performance of Pneumatic and Combustion Nailers ». Taiwan, National Cheng Kung University, 145 p.

INSPQ. 2015. *Nombre de nouveaux cas de surdités professionnelles acceptés par la CSST*. 1 p.

ISO. 2010. *Acoustics: Determination of sound power levels and sound energy levels of noise sources using sound pressure. Survey method using an enveloping measurement surface over a reflecting plane*. Switzerland: ISO, 48 p.

ISO. 2011. *Mechanical vibration and shock-Characterization of the dynamic mechanical properties of visco-elastic materials -Part 5: Poisson ratio based on comparison between measurements and finite element analysis*. Switzerland: ISO, 13 p.

Jayakumar, V, J Kim and E Zechmann. 2015. « Identification of noise sources and design of noise reduction measures for a pneumatic nail gun ». *Noise Control Engineering Journal,* vol. 63, p. 159-168.

Kim, BS, GJ Kim and TK Lee. 2007. « The identification of tyre induced vehicle interior noise ». *Applied Acoustics,* vol. 68, n° 1, p. 134-156.

Koruk, H, and A Arisoy. 2015. « Identification of crack noises in household refrigerators ». *Applied Acoustics,* vol. 89, p. 234-243.

Kumar, S, and NS Srivastava. 1975. « Investigation of noise due to structural vibrations using a cross-correlation technique ». *The Journal of the Acoustical Society of America,* vol. 57, n° 4, p. 769-772.

Leclère, Q., C. Pézerat, B. Laulagnet and L. Polac. 2005. « Application of multi-channel spectral analysis to identify the source of a noise amplitude modulation in a diesel engine operating at idle ». *Applied Acoustics,* vol. 66, n° 7, p. 779-798.

Lee, GS, C Cheong, SH Shin and SS Jung. 2012. « A case study of localization and identification of noise sources from a pitch and a stall regulated wind turbine ». *Applied Acoustics,* vol. 73, n° 8, p. 817-827.

Lefebvre, L, and F Laville. 2008. « Noise source identification for mechanical systems generating periodic impacts ». *Applied Acoustics,* vol. 69, n° 9, p. 812-823.

Lighthill, MJ. 1962. « The Bakerian lecture, 1961. Sound generated aerodynamically ». In *Proceedings of the Royal Society of London A: Mathematical, Physical and Engineering Sciences*. Vol. 267, p. 147-182. The Royal Society.

Lighthill, MJ. 1963. « Jet noise ». *AIAA Journal,* vol. 1, n° 7, p. 1507-1517.

Lin, TJ, and JM LaFave. 2012. « Experimental structural behavior of wall-diaphragm connections for older masonry buildings ». *Construction and Building Materials,* vol. 26, n° 1, p. 180-189.

Lu, Chia-Hua, Yean-Ren Hwang, Yu-Ta Shen and Tzu-Yu Wang. 2011. « Analysis and Modeling of a Pneumatic Servo System Based on Backstepping Design ». *Journal of Dynamic Systems, Measurement, and Control,* vol. 133, n° 6, p. 061013-061013.

Lukaszewska, E, H Johnsson and M Fragiacomo. 2008. « Performance of connections for prefabricated timber–concrete composite floors ». *Materials and Structures,* vol. 41, n° 9, p. 1533-1550.

Ma, Jia, Guoming G. Zhu and Harold Schock. 2010. « A Dynamic Model of an Electropneumatic Valve Actuator for Internal Combustion Engines ». *Journal of Dynamic Systems, Measurement, and Control,* vol. 132, n° 2, p. 021007-021007.

Mascia, Nilson Tadeu, and Claudia Lucia de Oliveira Santana. 2009. « Remarks on the slip modulus of nailed connections for linear analysis of plywood timber beams ». *Construction and Building Materials,* vol. 23, n° 8, p. 2731-2737.

Miller, Jonathan I., Tim J. Flack and David Cebon. 2014. « Modeling the Magnetic Performance of a Fast Pneumatic Brake Actuator ». *Journal of Dynamic Systems, Measurement, and Control,* vol. 136, n° 2, p. 021022-021022.

Nieto, AJ, AL Morales, A Gonzalez, JM Chicharro and P Pintado. 2008. « An analytical model of pneumatic suspensions based on an experimental characterization ». *Journal of Sound and Vibration,* vol. 313, n° 1, p. 290-307.

NIOSH. 2014. « NOISE AND HEARING LOSS PREVENTION: Facts and Statistics ». In *Centers for Disease Control and Prevention:Saving lives, Protecting People*. < http://www.cdc.gov/niosh/topics/noise/stats.html >. Accessed April 15, 2013.

Pallas, M. A., R. Chatagnon and J. Lelong. 2014. « Noise emission assessment of a hybrid electric mid-size truck ». *Applied Acoustics,* vol. 76, p. 280-290.

Pallas, M. A., J. Lelong and R. Chatagnon. 2011. « Characterisation of tram noise emission and contribution of the noise sources ». *Applied Acoustics,* vol. 72, n° 7, p. 437-450.

Porumamilla, H., A. G. Kelkar and J. M. Vogel. 2008. « Modeling and Verification of an Innovative Active Pneumatic Vibration Isolation System ». *Journal of Dynamic Systems, Measurement, and Control,* vol. 130, n° 3, p. 031001-031001.

Pu, H, X Luo and X Chen. 2011. « Modeling and analysis of dual-chamber pneumatic spring with adjustable damping for precision vibration isolation ». *Journal of Sound and Vibration,* vol. 330, n° 15, p. 3578-3590.

Rammer, DR, SG Winistorfer and DA Bender. 2001. « Withdrawal strength of threaded nails ». *Journal of Structural Engineering,* vol. 127, n° 4, p. 442-449.

Riachy, S, and M Ghanes. 2014. « A nonlinear controller for pneumatic servo systems: Design and experimental tests ». *Mechatronics, IEEE/ASME Transactions on,* vol. 19, n° 4, p. 1363-1373.

Ribner, HS. 1964. « The generation of sound by turbulent jets ». *Advances in Applied Mechanics,* vol. 8, p. 103-182.

Richards, EJ, and I Carr. 1986. « On the prediction of impact noise, X: The design and testing of a quietened drop hammer ». *Journal of sound and vibration,* vol. 104, p. 137-164.

Richards, EJ, I Carr and M Westcott. 1983. « On the prediction of impact noise, V: The noise from drop hammers ». *Journal of Sound and Vibration,* vol. 88, n° 3, p. 333-367.

Richards, EJ, ME Westcott and RK Jeyapalan. 1979. « On the prediction of impact noise, II: Ringing noise ». *Journal of Sound and Vibration,* vol. 65, n° 3, p. 419-451.

Richer, E, and Y Hurmuzlu. 2000a. « A high performance pneumatic force actuator system: Part I—nonlinear mathematical model ». *Journal of Dynamic Systems, Measurement, and Control,* vol. 122, n° 3, p. 416-425.

Richer, E, and Y Hurmuzlu. 2000b. « A high performance pneumatic force actuator system: part II—nonlinear controller design ». *Journal of Dynamic Systems, Measurement, and Control,* vol. 122, n° 3, p. 426-434.

Schuder, CB, and RC Binder. 1959. « The response of pneumatic transmission lines to step inputs ». *Journal of Basic Engineering,* vol. 81, n° 12, p. 578-584.

Shanks, E. 2008. *Noise emission from fastener driving tools*. United Kingdom: HSE, 51 p.

Sorli, M, G Figliolini and S Pastorelli. 2004. « Dynamic model and experimental investigation of a pneumatic proportional pressure valve ». *Mechatronics, IEEE/ASME Transactions on,* vol. 9, n° 1, p. 78-86.

Stern, EG. 1950a. « Improved nails for building construction ». *Bull. Va polytech. Inst.,* vol. 43, n° 6, p. 1-23.

Stern, EG. 1950b. « Improved nails. Their driving resistance, withdrawal resistance, and lateral load-carrying capacity ». *Transactions Amer. Soc. Mech. Engnrs,* vol. 72, n° 8, p. 987-98.

Stern, EG, and V Blacksburg. 1956a. « Better construction with threaded nails ». *Bulletin*, n° 25.

Stern, EG, and V Blacksburg. 1956b. *Plain-shank vs. fluted vs. threaded nails*. Virginia Polytechnic Institute, Wood Research Laboratory.

Stewart, ND, JR Bailey and JA Daggerhart. 1975. « Study of parameters influencing punch press noise ». *Noise Control Engineering,* vol. 5, n° 2, p. 80-86.

Subramanian, SC, S Darbha and KR Rajagopal. 2004. « Modeling the Pneumatic Subsystem of an S-cam Air Brake System ». *Journal of Dynamic Systems, Measurement, and Control,* vol. 126, n° 1, p. 36-46.

Szirtes, T. 2007. *Applied dimensional analysis and modeling*. Butterworth-Heinemann.

Tam, CKW. 1995. « Supersonic jet noise ». *Annual Review of Fluid Mechanics,* vol. 27, n° 1, p. 17-43.

Timmins, P, and O Granger. 2010. *Occupational noise-induced hearing loss in Australia: Overcoming barriers to effective noise control and hearing loss prevention*. Australia: Safe Work Australia, 207 p.

Tisserand, JX, and S Triomphe. 2011. « Fabrication de palettes : Réduction du bruit de l ' échappement de cloueurs pneumatiques ». In *Bruit et vibrations au travail*. (France), p. 7. France.

Tomasi, R, and T Sartori. 2013. « Mechanical behaviour of connections between wood framed shear walls and foundations under monotonic and cyclic load ». *Construction and Building Materials,* vol. 44, p. 682-690.

Troccaz, P, R Woodcock and F Laville. 2000. « Acoustic radiation due to the inelastic impact of a sphere on a rectangular plate ». *The Journal of the Acoustical Society of America,* vol. 108, n° 5, p. 2197-2202.

Tsai, DH, and EC Cassidy. 1961. « Dynamic behavior of a simple pneumatic pressure reducer ». *Journal of Basic Engineering,* vol. 83, n° 2, p. 253-264.

Villaggio, P. 2005. « Hammering of nails and pitons ». *Mathematics and mechanics of solids,* vol. 10, n° 4, p. 461-468.

Wang, Y, WC Su, P Kasemsiri and S Hiziroglu. 2011. « A comparison of the withdrawal resistance load of nails using experimental and interference approaches ». *Wood Material Science & Engineering,* vol. 6, n° 4, p. 213-218.

Whitmore, SA, WT Lindsey, RE Curry and GB Gilyard. 1990. *Experimental characterization of the effects of pneumatic tubing on unsteady pressure measurements*. Coll. « NASA Technical Memorandum 4171 », NASA TM-4171. California, USA: NASA, 30 p.

Wilcox, WW, EE Botsai and H Kubler. 1991. *Wood as a building material: a guide for designers and builders*. Wiley.

Wills, BL, SG Winistorfer, DA Bender and DG Pollock. 1996. « Threaded-nail fasteners—Research and standardization needs ». *Transactions of the ASAE,* vol. 39, n° 2, p. 661-668.

Witczak, KJ. 1976. « Flow patterns and noise of a choked gas jet expanding into a duct ». *Archives Acoustics,* vol. 1, p. 181-200.

Zarnani, P, and P Quenneville. 2014. « Strength of timber connections under potential failure modes: An improved design procedure ». *Construction and Building Materials,* vol. 60, p. 81-90.

Zhong, W, GL Tao, H Liu and Z Xiang. 2008. « Mathematical modeling and simulation of pneumatic nail gun ». *Journal-Zhejiang university engineering science,* vol. 42, n° 2, p. 239.

Zhou, T, and ZW Guan. 2011. « A new approach to obtain flat nail embedding strength of double-sided nail plate joints ». *Construction and Building Materials,* vol. 25, n° 2, p. 598-607.